Geometrical characteristics of random fields : on the perimeter of a binary image : estimation procedures, testing, and numerical implementations

Mariem Abaach

To cite this version:

Mariem Abaach. Geometrical characteristics of random fields : on the perimeter of a binary image : estimation procedures, testing, and numerical implementations. Mathematics [math]. Université Paris Cité, 2023. English. NNT : 2023UNIP7150 . tel-04601975

HAL Id: tel-04601975
https://theses.hal.science/tel-04601975

Submitted on 5 Jun 2024

Université Paris Cité
École doctorale de Science Mathématiques de Paris Centre (ED 386)

Établissement d'inscription : Université Paris Cité

Laboratoire d'accueil : Laboratoire MAP5, UMR 8145

Geometrical characteristics of random fields

On the perimeter of a binary image : estimation procedures, testing, and numerical implementations.

Mariem ABAACH

Thèse de doctorat de Mathématiques appliquées

Dirigée par :
Anne ESTRADE, Elena Di BERNARDINO
et Hermine BIERMÉ

Date de soutenance : 24 novembre 2023

Jury de soutenance :

Jean Marc AZAÏS	(Professeur émérite, Université de Toulouse) Examinateur
Hermine BIERMÉ	(Professeure des universités, Université de Tours) Co-encadrante et invitée
Elena DI BERNARDINO	(Professeure des universités, Université Côte d'Azur) Codirectrice de thèse
Anne ESTRADE	(Professeure des universités, Université Paris Cité) Directrice de thèse
Bruno GALERNE	(Professeur des universités, Université d'Orléans) Examinateur
Marie KRATZ	(Full Professor, ESSEC Business School) Rapporteuse
Dominico MARINUCCI	(Full Professor, University of Rome Tor Vergata) Rapporteur
Frédéric RICHARD	(Professeur des universités, Aix-Marseille Université) Président du jury

Université Paris Cité
Campus Saint-Germain
45, rue des Saints-Pères
75006 Paris FRANCE

Je dédie cette thèse à mon Jeddi Kebour (mon
grand père paternel), qui a cru en l'école même si
lui-même n'y a jamais mis les pieds.

Mon père raconte que mon grand-père lui répétait souvent

"سف ربي اكمل"

Face au danger le chat se répète :
"Gonfle toi et Dieu fera le reste"

Remerciements

La partie des remerciements est la part la plus personnelle du manuscrit, ou finalement on dévoile bien plus sur soit que dans le reste de la thèse. La tâche est rude car de simple mots ne peuvent exprimer l'ampleur de ma reconnaissance envers toutes les personnes qui m'ont soutenue durant cette aventure, ce qui suit n'est donc qu'un humble essai pour exprimer toute ma gratitude envers eux.

Je tiens tout d'abord à adresser mes remerciements les plus sincères à Hermine Biérmé, Elena Di Bernardino et Anne Estrade. Sans votre soutien, je ne serai jamais arrivée au bout de cette aventure. Merci pour votre écoute, votre présence, votre confiance et votre aide, je n'aurais sincèrement pas pu rêver meilleure équipe.

Je tiens également à remercier les membres du jury pour leur travail de relecture, et pour leurs questions qui ont donné naissance à un agréable échange le jour de la soutenance.

Je remercie l'équipe des permanents, Julie, Céline, Jonathan, Raphaël, Fabienne, Marc, Rémy, Marie, Joan, Éric, et bien évidemment Marie-Hélène, ton écoute et ton accompagnement ont été très précieux, merci à vous tous pour votre dévouement, votre passion contagieuse et votre lutte pour un monde meilleur !

Aux doctorants de Paris 5 (oui oui P5 !) à commencer par mes co-bureaux, Ariane mon meilleur coach personnel, Rémy L. et Rémy B. dont les blagues ont apporté de la légéreté à mon quotidien, je cite aussi Lucia, Angie, Keanu, Béatriz, Bianca, Yassine et nos longues discussions philosophiques sur la thèse, le monde et l'esprit humain, my dear Sergio, I will never forget the hug you gave me after I accidentally deleted my draft, it gave me the power to pull myself up and got look for the stored version, thank you for that. Sonia et Ivan, à jamais mes co-organisteurs de conf préférés ! Diala, ton travail, ton acharnement et ton sérieux ont toujours été une source d'inspiration, Zoé, merci pour ton sourire et ta bonne humeur. Merci également à Cécile, Safa, Mehdi, Herb, Loïc, Ousmane, Anton, Laurent, Arthur, Marie, Juliana et Pierre-Louis.

Sans oublier le labo de Nice où j'ai été acceuillie trois mois par ans pendant mes années de thèse, merci Alexis et nos théories sur le lien entre la volatilité de la qualité des repas du Crous et l'impression de goût et d'excellence. Sara et Ryan, I will never forget the late nights we spent chilling at the beach at the Porquerolles conference, it is one of the best memories I have of the PhD ! Paul, Yash et Dimitri, ce fut un plaisir !

Aux doctorants et maîtres de conférence d'autres horizons, Cérine, nothing more than thank you for existing and for being the amazing human you are. Taher, mon pianiste préféré ! Antoine, le grand frère de thèse le plus cool qui existe. Michel et Jonathan, grâce à vous, les conf de géo sto furent bien plus agréable à vivre. Eddie, pour tes encouragements et ta bienveillance, Claire, merci pour ton sourire et ton soutien. Et enfin, François Liret, mon prof d'algèbre et de nav. préféré.

À mes amis, Ilias, my favorite Bikhu, I stopped counting the number of times I randomly showed up saying that this time was it, that my cup was full and that I was going to give up, and you, just patiently saying : nope, and for the bazillionth time, helped me pick myself up and try again, thank you for your patience, my friend. Rahma, merci pour ton soutien inébranlable, sur lequel j'ai toujours pu compter. Jassou mon pilier constant, Kenza, Reda, Ghita, Elena et Said, merci à vous. Et enfin, pendant toute cette aventure tu m'as soutenue et a cru en moi, merci d'être la personne que tu es, merci Mikael d'avoir été là.

Et enfin, à ma famille, en commençant par mes cousins Asmaa, qui est une source d'inspiration au quotidien. Redouane et nos discussions philo. Mes frères Youssef et Yahia, my favorite pair of guys in the whole world. Et mes parents, mon papa, qui m'a fait découvrir la beauté des maths et m'a toujours encouragé à poursuivre mes rêves, et enfin ma maman, merci pour ton amour inconditionnel !

J'ai eu la chance pendant cette thèse de rencontrer des gens extraordinaires, passionnés, passionnants, exemples d'acharnement, mais aussi de vivre des expériences incroyables (petit clin d'œil à Oberwolfach), et pour cela, je serai à jamais reconnaissante !

Contents

1 INTRODUCTION (VERSION FRANÇAISE)

En traitement d'image, nous pouvons considérer une image comme la réalisation d'un champ aléatoire 2d discrétisé ce qui permet de définir un cadre statistique pour analyser les propriétés et les caractéristiques des images. Les défis à relever dans le cadre du traitement d'image incluent le débruitage d'image, la détection de motifs, la segmentation et la classification des images (voir, par exemple, Blake et al. (2011); Jähne (2005)). Plus précisément, en utilisant des outils issus du cadre rigoureux de la géométrie stochastique, nous pouvons comprendre et analyser les propriétés géométriques du champ aléatoire sous-jacent et obtenir des informations précieuses sur les éléments structurels de l'image, ce qui permet de réaliser différentes tâches d'apprentissage automatique (N.M. van Lieshout (2009)).

L'étude directe de la géométrie de l'image peut s'avérer délicate, nous choisissons plutôt de considérer l'ensemble des images seuillées associées à une même image, communément appelées ensembles d'excursion. Ainsi, nous obtenons des informations de natures 'sparses' qui capturent les informations géométriques de l'image. Pour examiner les caractéristiques de ces images en noir et blanc, nous faisons appel à trois caractéristiques géométriques : l'aire (nombre de pixels blancs dans l'image en noir et blanc), le périmètre (la longueur du contour de la partie blanche) et la caractéristique d'Euler qui est définie dans notre contexte 2d comme la différence entre le nombre de composantes connexes et le nombre de trous dans l'image en noir et blanc. Chacune de ces trois fonctionnelles encapsule des informations essentielles sur les caractéristiques géométriques et topologiques de l'ensemble d'excursion. Elles sont étroitement associées aux fonctionnelles de Minkowski et font l'objet d'études approfondies en géométrie intégrale et stochastique (Chiu et al. (2013)). Elles sont également connues sous le nom de courbures Lipschitz-Killing (LKC) des ensembles d'excursion, et nous renvoyons le lecteur à Adler (1981) ou Thäle (2008) pour une introduction formelle au sujet. Ces fonctionnelles servent de descripteurs de forme efficaces et trouvent des applications dans divers domaines, pour n'en citer que quelques-uns : la cosmologie (Schmalzing and Górski (1998)), la médecine (imagerie cérébrale, Flandin and Friston (2015), mammographies numériques, Biermé et al. (2019)).

De nombreux résultats théoriques ont été établis dans le cadre des champs aléatoires continus. Les propriétés statistiques des LKC ont été étudiées dans divers cadres, et d'importants résultats ont été obtenus, notamment pour les champs aléatoires gaussiens, et les shots noises. Nous renvoyons le lecteur à Biermé and Lerbet (2022); Lachièze-Rey (2019a); Biermé and Desolneux (2016); Bulinski et al. (2012b) pour plus de détails.

Dans cette thèse, nous nous concentrons sur le périmètre des ensembles d'excursion d'une image en explorant ses propriétés statistiques et en révélant les structures qu'il hérite du champ aléatoire sous-jacent.

Nous commençons par introduire le cadre théorique pour modéliser les images à l'aide de champs aléatoires.

1.1 D'un champ aléatoire aux images binaires

1.1.1 Construction (rigoureuse) de l'image binaire

Soit m un entier avec $m \geq 2$. Sans perte de généralité, nous considérons notre fenêtre d'observation comme étant le carré $S = [0, m]^2$ et nous le divisons en m^2 carrés disjoints. Nous notons e_1, e_2 les éléments de la base canonique de $\mathbb{R}^2$ et nous introduisons les notations suivantes.

- $\mathbb{G}_m$ est l'ensemble des points dans S ayant des coordonnées entières dans $[0, m)$, nous écrivons $x = (x_1, x_2)$ avec $x_1, x_2 \in \{0, \dots, m-1\}$ pour tout $x \in \mathbb{G}_m$.
- Pour $x \in \mathbb{G}_m$, $C_m(x) := x + \left[0, 1\right]^2$ sera appelé une *cellule* (c'est-à-dire un pixel). Remarquons que $S = \cup_{x \in \mathbb{G}_m} C_m(x)$.
- Nous désignons par $\mathcal{E}_m^{(1)}$, $\mathcal{E}_m^{(2)}$ l'ensemble des arêtes verticales et horizontales dans $\mathring{S}$ comme présenté dans la Figure 1.1, respectivement les segments rouges et bleus.

La Figure 1.1 montre un exemple de pavage carré avec $m = 4$.

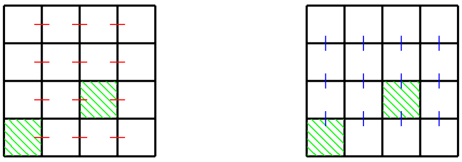

Figure 1.1 – Pavage carré pour $m = 4$ et les cellules associées $C_4((0,0))$ et $C_4((2,1))$ (rayures vertes). Nous représentons les arêtes verticales en rouge et les arêtes horizontales en bleu.

En utilisant les notations introduites ci-dessus, nous observons une image $I : x \in \mathbb{G}m \to \mathbb{R}$. En considérant un paramètre de seuillage $t \in \mathbb{R}$, nous introduisons l'image binaire associée, comme indiqué dans la Figure 1.2, où chaque cellule (pixel) $C_m(x)$ dans l'image I se voit attribuer soit une couleur noire, soit une couleur blanche, en fonction de si $I_x \geq t$ ou $I_x < t$. L'ensemble des cellules $C_m(x)$ pour lesquelles $I_x \geq t$ est connu dans la littérature sous le nom d'ensemble d'excursion et est souvent noté $E_I(t)$. Dans la Figure 1.2, nous représentons une image en niveaux de gris, sa représentation en 3d et son image seuillée associée pour $t = 87$.

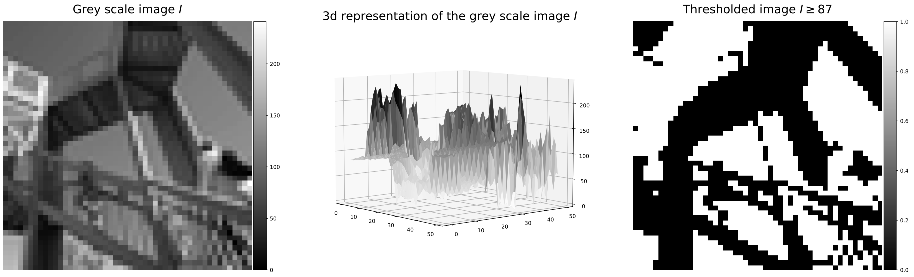

Figure 1.2 – Une image I, sa représentation 3d, et l'image seuillé pour $t = 87$.

Les champs aléatoires sont couramment utilisés pour modéliser les images car ils offrent un cadre théorique permettant de capturer les dépendances entre les pixels ou les régions voisines dans l'image.

1.1.2 Champs Aléatoires

Un champ aléatoire peut être vu comme un processus stochastique prenant généralement des valeurs réelles et défini sur un espace de paramètres de dimension au moins égale à 1 (nous renvoyons le lecteur à Adler and Taylor (2007); Biermé (2017) pour une introduction détaillée). Dans le cadre de notre étude, l'espace de paramètres est $\mathbb{Z}^2$.

En général, les champs aléatoires sont des fonctions mathématiques qui attribuent des valeurs aléatoires à des points dans un espace de paramètres. Dans notre cas, nous considérons le champ aléatoire X sur une grille discrète qui ne peut être observé que dans le cadre d'une fenêtre bornée S et qui prend des valeurs dans $\mathbb{R}$. Ainsi, nous considérons le champ X comme une image pixelisée aléatoire, où à chaque pixel est attribuée à une valeur réelle aléatoire.

Une classe importante de champs aléatoires est la classe des champs aléatoires stationnaires, il s'agit de champs qui sont invariants par translation ; cette propriété les rend largement utilisés pour modéliser des régions homogènes et des textures. Plus précisément, l'hypothèse de stationnarité stipule que pour tout $h \in \mathbb{Z}^2$,

$$\left(X_{x+h}; x \in \mathbb{Z}^2\right) \overset{fdd}{=} \left(X_x; x \in \mathbb{Z}^2\right),$$

où fdd désigne les distributions finies dimensionnelles.

Ainsi, en utilisant le cadre précédemment introduit, nous observons l'image I, que nous supposons correspondre aux valeurs d'une réalisation d'un champ aléatoire stationnaire $(X_x)\, x \in \mathbb{Z}^2$ défini sur un espace de probabilité, de telle sorte que $I_x = X_x(w)$. Étant donné un paramètre de seuillage $t \in \mathbb{R}$, nous considérons l'image en noir et blanc associée en appliquant la procédure que nous avons décrite ci-dessus.

La Figure 1.3 présente plusieurs générations de champs aléatoires et les images seuillées qui leur sont associées.

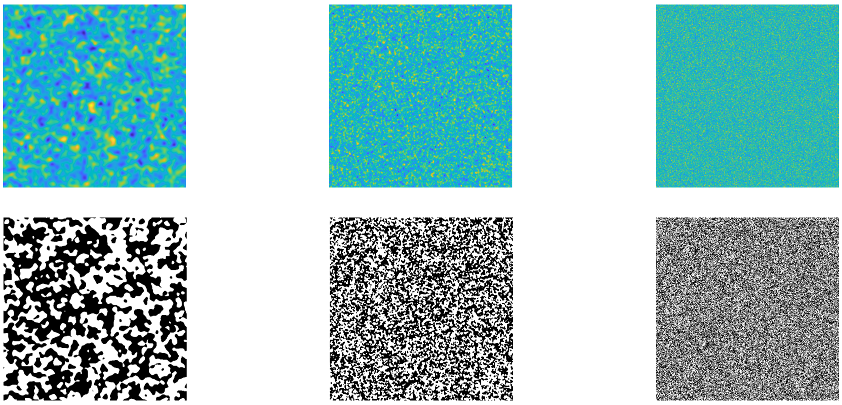

Figure 1.3 – Génération de trois champs aléatoires (première ligne) et leurs images seuillées respectives pour $t = 0$ et $m = 512$ (deuxième ligné).

Comme indiqué précédemment, une façon d'accéder à la géométrie d'un ensemble est d'explorer le comportement des courbures de Lipschitz-Killing qui lui sont associées : l'aire, le périmètre et la caractéristique d'Euler. Plus précisément, l'aire fournit des informations sur la densité d'occupation dans l'ensemble, le périmètre offre des indications sur sa régularité, et la caractéristique d'Euler, qui est également un invariant topologique, quantifie sa connectivité ou la présence de trous.

Pour chaque valeur de seuil t, nous pouvons calculer le périmètre de l'image binaire associée à t, définissant ainsi la fonction aléatoire $\mathcal{P}_m : t \mapsto \mathcal{P}_m(t)$ qui est le périmètre des ensembles d'excursion du champ aléatoire $(X_x)_{x \in \mathbb{G}_m}$. Dans cette thèse, nous nous concentrons sur l'étude du comportement statistique du périmètre et sur la mise en évidence des structures qu'il hérite du champ aléatoire sous-jacent.

1.2 Périmètre orienté d'une image binaire

1.2.1 Définition formelle

Suivant l'approche présentée dans Biermé and Desolneux (2021), pour chaque arête $w \in \mathcal{E}_m = \mathcal{E}_m^{(1)} \cup \mathcal{E}_m^{(2)}$, nous cherchons à savoir si w contribue au périmètre de l'ensemble en noir (voir Figure 1.4). En utilisant la nature additive du périmètre, on peut commencer par calculer le périmètre orienté dans chaque direction, horizontale et verticale.

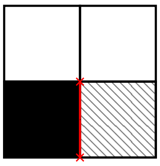

Figure 1.4 – L'arête w en rouge appartient à $C_2((0,0)) \cap C_2((1,0))$, avec la cellule $C_2((0,0))$ colorée en noir et $C_2((1,0))$ en rayures grises pointillées.

À la suite de cette remarque, pour une valeur de seuil fixée t, on peut considérer l'image binaire

$$Z_t^m = \left(\mathbb{1}_{\{X_x \geq t\}}\right)_{x \in \mathbb{G}_m}, \tag{1.1}$$

et définir la quantité aléatoire,

$$f_t^{(i)}(x) := \mathbb{1}_{\{\min(X_x, X_{x+e_i}) < t \leq \max(X_x, X_{x+e_i})\}}, \qquad x \in \mathbb{G}_m^{(i)}, \quad \text{for } i \in \{1,2\} \tag{1.2}$$

afin de prendre en compte la contribution éventuelle au périmètre de la partie noir de $Z_t^{(m)}$ de l'arête w qui correspond à l'intersection des deux cellules, $C(x)$ et $C(x+e_j)$. Introduisons maintenant l'outil principal de cette étude.

Definition 1.2.1 (Périmètre orienté)**.** *Pour $t \in \mathbb{R}$, nous notons $\mathcal{P}_m^{(i)}(t)$ la somme de toutes les contributions dans la i-ème direction (verticale pour $i = 1$ et horizontale pour $i = 2$) et nous l'appelons le périmètre orienté de l'image binaire $Z_t^{(m)}$,*

$$\mathcal{P}_m^{(i)}(t) = \sum_{x \in \mathbb{G}_m^{(i)}} f_t^{(i)}(x). \tag{1.3}$$

Le périmètre de $Z^{(m)}t$ est donné par $\mathcal{P}_m(t) := \mathcal{P}_m^{(1)}(t) + \mathcal{P}_m^{(2)}(t)$.

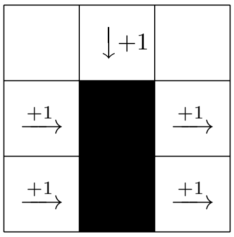

Figure 1.5 – Calcul du périmètre d'une image binaire avec $m = 3$. Ici, $\mathcal{P}_3^{(1)} = 4$ et $\mathcal{P}_3^{(2)} = 1$.

Ci-dessous, nous présentons un algorithme pour calculer le périmètre d'une image binaire, qui implémente la Définition 1.2.1, avec M et N correspondant à la largeur et la longueur de l'image I. Dans le contexte de notre travail, nous supposons que $M = N = m$.

Algorithm 1 Calcul du périmètre d'une image binaire en utilisant l'Équation (1.3)

```
**Initialization** Image binaire $Z$ de taille $(M, N)$,
**Do** $L_1 = \text{somme}((Z[0:M-1, 0:N] == 1) \times (Z[1:M, 0:N] == 0))$
    $L_2 = \text{somme}((Z[0:M, 0:N-1] == 1) \times (Z[0:M, 1:N] == 0))$
    $L_3 = \text{somme}((Z[0:M-1, 0:N] == 0) \times (Z[1:M, 0:N] == 1))$
    $L_4 = \text{somme}((Z[0:M, 0:N-1] == 0) \times (Z[0:M, 1:N] == 1))$
    $P_1 = L_1 + L_3$
    $P_2 = L_2 + L_4$
**Return** $P_1 + P_2$
```

1.2.2 Biais

Avant d'aller plus loin, il est essentiel de noter que considérer le champ aléatoire comme une image pixelisée bornée et non comme l'entité continue et infinie qu'il est, entraîne quelques biais. Le premier biais est lié au problème de discrétisation, et le second est dû à la fenêtre bornée S dans laquelle nous observons le champ.

LE PROBLÈME DE DISCRÉTISATION Le terme *biais* fait référence à l'erreur de pixelisation qui se produit numériquement en raison de la représentation discrétisée des images. L'hypothèse initiale que nous avons faite est que l'image étudiée I est considérée comme correspondant aux valeurs observables de la réalisation d'un champ aléatoire continu X sur la fenêtre discrète S. Comme nous supposons que l'image $I_x = X_x$ avec x pris sur une grille discrète, cela introduit un biais (exemple Figure 1.2 représente une image discrétisée d'un phénomène du monde réel qui est intrinsèquement continu). La plupart des travaux qui étudient ces caractéristiques géométriques (Azaïs and Wschebor (2009); Kratz and Vadlamani (2017)) repose sur des hypothèses fortes concernant la régularité du champ aléatoire sous-jacent. On suppose souvent que le champ a des trajectoires régulières (C^k, $k \geq 1$).

En pratique, nous n'avons pas accès à l'objet sous-jacent continu, car il n'est pas accessible empiriquement. Nous pouvons seulement accéder à la fonction prise en certains points de la grille discrète $\mathbb{G}_m$. Par conséquent, les ensembles d'excursions obtenus sont discrétisés, et les bords verticaux et horizontaux forment leur frontière. Cependant, ces bords ne représentent pas exactement la véritable frontière de l'objet. Cela introduit un biais discuté dans Biermé and Desolneux (2021) ; où les autrices étudient comment le périmètre moyen des ensembles d'excursion change lorsque l'on considère des versions discrétisées (grille carrée ou hexagonale) des champs aléatoires stationnaires et isotropes sous-jacents. elles montrent en particulier qu'en moyenne, sous certaines conditions de stationnarité et d'isotropie sur le champ aléatoire, le périmètre est toujours biaisé (avec un facteur de $4/\pi$) dans un contexte de grille dense lorsqu'on essaie de se rapprocher de l'objet sous-jacent continu. Cotsakis et al. (2022a) dérivent une formule explicite pour le biais, montrant qu'il dépend uniquement de la dimension spatiale d, ce qui leur permet d'établir un estimateur non biaisé pour le périmètre des ensembles d'excursion qui sont approximés par des tétrahèdres dans $\mathbb{R}^d$. Cotsakis et al. (2022b) proposent une méthode pour calculer un estimateur non biaisé du périmètre des ensembles d'excursion de champs aléatoires sur $\mathbb{R}^2$ observés sur une grille carrée régulière, en introduisant des diagonales. La construction de l'estimateur nécessite un réglage préalable et perd la propriété additive du périmètre, ce qui rend ces statistiques plus difficiles d'accès.

Biais de bord Lors de l'étude du périmètre des ensembles d'excursion dans les images, un biais naturel apparaît en raison de la nature bornée du domaine S, ce qui a pour concéquence d'introduire une frontière artificielle. Cependant, ce biais diminue lorsque la taille du domaine m tend vers l'infini. Afin de corriger ce biais, Biermé et al. (2019) proposent une méthode qui utilise d'autres caractéristiques géométriques disponibles dans les environnements 2d, à savoir la surface et la caractéristique d'Euler. elles construisent un estimateur non biaisé du périmètre en incorporant les autres caractéristiques géométriques en utilisant la 'Gaussian kinematic formula' (voir par exemple le Théorème 15.9.5 dans Adler and Taylor (2007); Schneider and Weil (2008)). Une autre approche pour corriger le biais consiste à traiter les bords d'un côté comme s'ils se prolongeaient jusqu'à l'extrémité opposée, ce qu'on appelle la correction toroïdale. Alternativement, lorsqu'il s'agit de grands ensembles de données, une méthode de correction efficace consiste à exclure les points proches de la frontière.

L'utilisation de champs aléatoires pour modéliser des images permet de décrire les relations spatiales entre les pixels et la régularité ou la texture de l'image. En revenant à l'image seuillée $Z_t^{(m)}$, voir Équation (1.1), pour chaque $x \in \mathbb{G}_m$, $Z_t^{(m)}(x)$ suit une distribution de Bernoulli de paramètre $\mathbb{P}(X_x \geq t)$. Dans la section suivante, nous étudierons comment la relation entre les pixels, dictée par la structure de dépendance du champ X, influence la géométrie de l'image en noir et blanc $Z_t^{(m)}$ et donc la structure de son périmètre également !

1.3 Structure de dépendance et géométrie

Ce qui régit la notion de dépendance du champ est la structure de covariance $K(s,t) = \mathrm{Cov}(X_t, X_s)$ qui encapsule le type de relation que les pixels auront entre eux. Il existe de nombreuses façons de définir la structure de covariance K, mais il y a deux conditions générales qu'elle doit vérifier.
Elle doit être symétrique, ce qui signifie que $\forall s,t \in \mathbb{Z}^2, K(s,t) = K(t,s)$, et définie positive: $\forall k \geq 1, t_1, \ldots, t_k \in \mathbb{Z}^2, \lambda_1, \ldots, \lambda_k \in \mathbb{R},\ \sum_{i,j=1}^{k} \lambda_i \lambda_j K(t_i, t_j) \geq 0$.

Dans le cadre de ce travail, nous ne considérons que des champs aléatoires stationnaires. Ainsi, il existe une fonction $\rho : \mathbb{Z}^2 \to \mathbb{R}$ telle que pour tout $s,t \in \mathbb{Z}^2$, $\rho(t-s) = \mathrm{Cov}(X_t, X_s)$. Nous nous concentrons sur le cas de la variance unitaire, c'est-à-dire $\rho(0) = 1$.

Lorsque le champ est également isotrope (invariant par rotation), ρ est souvent considérée par abus de language, comme une fonction de la distance entre les points, allant de $\mathbb{R}^+$ vers $\mathbb{R}$.

1.3.1 Portée de la dépendance

La fonction de covariance ρ capture l'information spatiale du champ et décrit le type de relation et d'influence qu'un pixel entretient avec ses voisins. Lors de l'assignation de valeurs aux pixels, une approche intuitive consisterait à attribuer à chaque pixel une valeur sans tenir compte des valeurs des pixels voisins. Dans ce cas, les pixels sont indépendants les uns des autres, et la valeur de leur covariance est nulle. Un tel champ aléatoire est appelé bruit blanc, comme illustré dans la Figure 1.6. Nous utilisons un modèle Gaussien pour les illustrations.

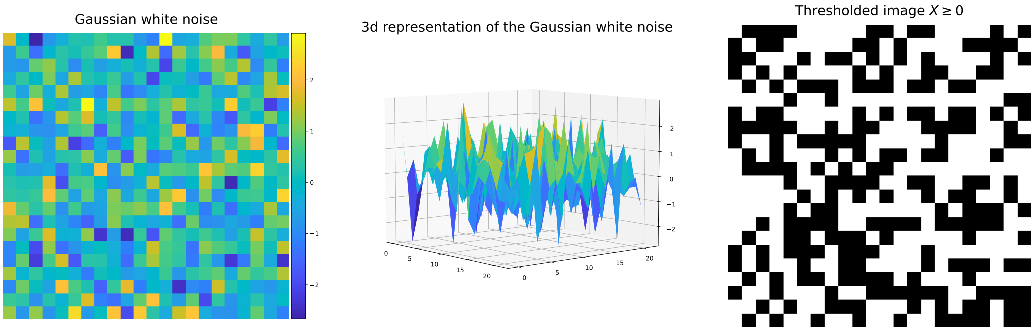

Figure 1.6 – Réalisation d'un bruit blanc Gaussien, $m = 22$.

Une autre façon possible d'attribuer des valeurs aux pixels est de les rendre totalement dépendants, ce qui signifie que la valeur de ses voisins détermine entièrement la valeur du pixel. En conséquence, connaître la valeur d'un pixel détermine les valeurs de tous les autres. Ce cas particulier correspond à une valeur de covariance égale à 1 en raison de la normalisation. Dans ce cas, le champ se comporte comme une seule variable aléatoire.

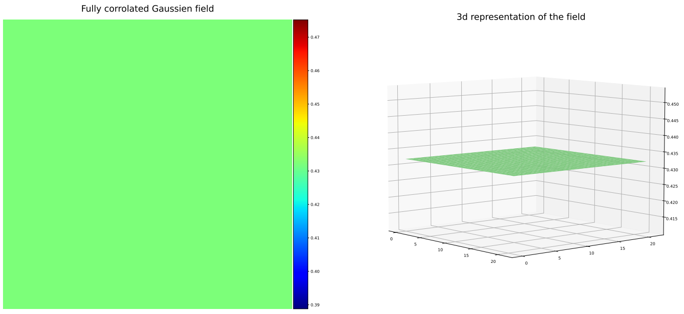

Figure 1.7 – Réalisation d'un champ Gaussien entièrement corrélé, $m = 22$.

Nous pouvons voir que la Figure 1.6 et la Figure 1.7 représentent deux extrêmes ; dans le premier cas ($\forall x \in \mathbb{Z}^2 \setminus \{(0,0)\}, \rho(x) = 0$), chaque pixel se comporte de manière indépendante, ne laissant aucune place à toute ressemblance d'ordre ou de motif discernable, juste du bruit. Dans le second cas ($\rho \equiv 1$), un degré excessif d'ordre domine le champ, ne laissant aucune place à la spontanéité ou à la variation, conduisant à des images parfaitement plates et uniformes. Un juste milieu existe, et entre ces deux extrêmes se trouve tout un monde de possibilités de formes et de motifs, et la fonction de covariance du champ régit tout cela. En un sens, la covariance mesure la déviation par rapport à l'aléatoire spatial, et décider du type de fonction de covariance que nous utilisons change complètement la nature des structures que nous obtenons. Une classe très importante de champs aléatoires est celle des champs aléatoires gaussiens qui permet de décrire d'un point de vue statistique un large éventail de structures naturelles, couvrant des domaines d'application divers tels que l'électronique, la géographie, l'apprentissage automatique et les phénomènes cosmiques. L'intérêt des champs aléatoires gaussiens réside dans leur capacité à capturer des propriétés essentielles de diverses structures naturelles tout en étant très faciles à manipuler car ils sont entièrement caractérisés par leur premier et second moment, ce qui les rend favorables pour les analyses théoriques. Utiliser un champ aléatoire gaussien pour modéliser une image signifie que tous ses pixels suivent une distribution gaussienne et que toute combinaison linéaire finie de pixels est gaussienne. Les champs aléatoires gaussiens centrés sont complètement caractérisés par leur fonction de covariance ρ.

Nous nous intéressons principalement au comportement local de la covariance, c'est-à-dire à la relation de dépendance entre un pixel et ses 4 voisins les plus proches. En général, nous nous situons entre les deux extrêmes ci-dessus.

Dans la Figure 1.8, nous considérons un modèle isotrope, et nous nous intéressons à mettre en évidence l'influence locale de la valeur de la covariance $\rho(e_i)$, la valeur de la covariance entre un pixel et son voisin, sur la nature des structures que nous observons sur l'image. Plus $\rho(e_i)$ est proche de 1, plus nous observons l'apparition de motifs réguliers et continus dans l'image et des valeurs bien groupées, indiquant un voisinage de pixels qui ont approximativement la même valeur. Inversement, plus $\rho(e_i)$ est proche de 0, moins l'image a de structure.

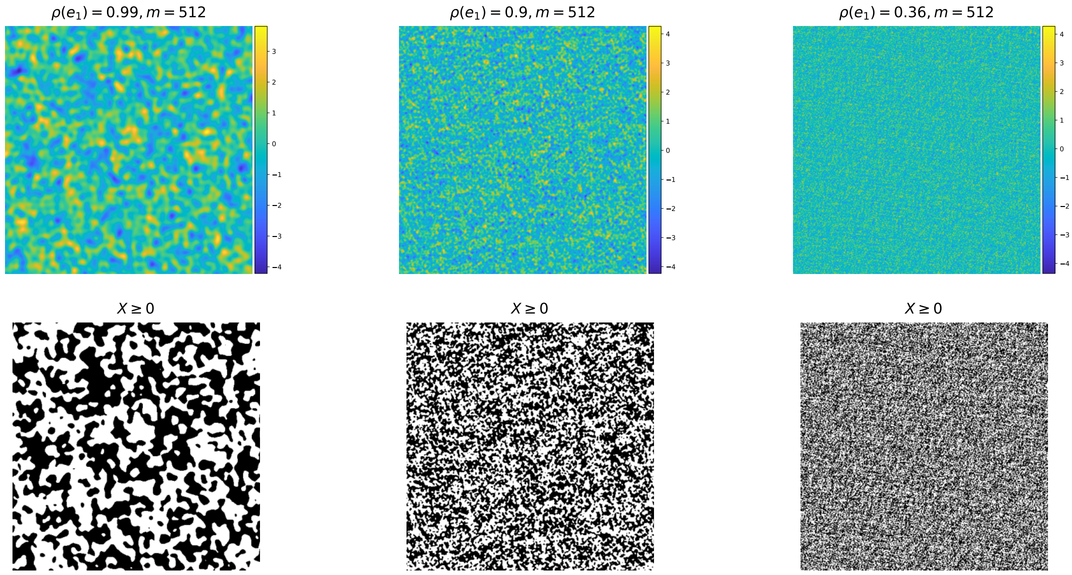

Figure 1.8 – Générations de champs aléatoires gaussiens ayant le même type de fonction de covariance mais avec différentes valeurs de $\rho(e_i)$.

1.3.2 Modèles gaussiens paramétriques

La simulation de champs aléatoires est un sujet largement exploré dans la recherche, avec de nombreux outils numériques disponibles dans la littérature. Dans cette thèse, nous utilisons deux outils spécifiques pour générer les images. Tout d'abord, nous avons utilisé le package Python **GeoStatTools** Müller et al. (2022), qui propose une gamme d'outils géostatistiques, y compris la génération de champs aléatoires. Ce package facilite le processus de génération en fournissant de nombreux modèles de covariance et en permettant aux utilisateurs d'intégrer les fonctions de covariance de leur choix. Nous renvoyons le lecteur intéressé à Müller et al. (2022) pour plus d'informations sur la méthode de génération.

Dans le deuxième chapitre de cette thèse, nous utilisons la fonction Matlab **stationary_Gaussian_process** pour générer un champ aléatoire gaussien. Cette fonction utilise la méthode des matrices circulantes pour générer le champ aléatoire, l'utilisateur doit fournir la fonction de covariance.

Dans les figures ci-dessous, nous présentons des exemples de réalisations de champs aléatoires gaussiens, avec deux modèles de covariance et différents degrés de dépendance.

CHAMP GAUSSIEN DE BERGMANN-FOCK. Le modèle de covariance le plus couramment utilisé est $\rho(x) = \exp(-\kappa ||x||_2^2)$, pour $x \in \mathbb{R}^2$ et $\kappa \in \mathbb{R}^+$, avec $||.||_2$ désignant la norme euclidienne de $\mathbb{R}^2$.

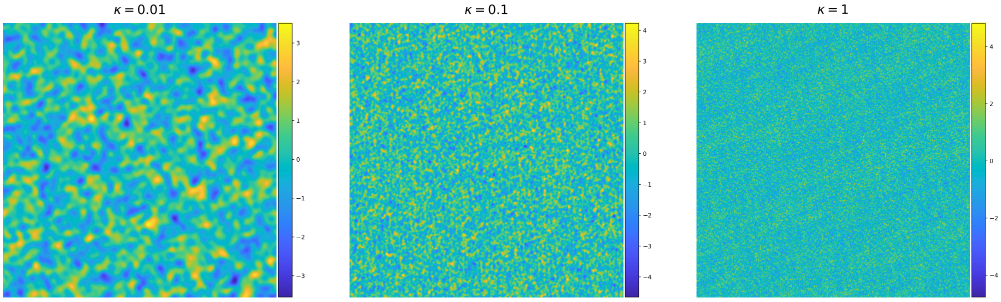

Figure 1.9 – Générations de champs aléatoires gaussiens avec $m = 512$, de gauche à droite $\kappa = 0.01, 0.1, 1$.

Comme on peut le voir dans la figure 1.9, à mesure que la valeur du paramètre κ diminue (exemple, image de gauche), la structure de dépendance dans le champ devient plus prononcée, révélant des motifs plus grands et plus discernables dans l'image. Le paramètre κ a un effet d'échelle et est étroitement lié à la résolution de l'image. Nous illustrons l'impact du choix de κ et de m dans la figure 1.10. Sur la première ligne, nous fixons la valeur de κ et changeons la valeur de m pour démontrer l'effet de zoom. Sur la deuxième ligne, nous fixons la graine de l'algorithme (la randomisation) pour montrer l'effet, en modifiant la valeur de m tout en ajustant κ pour obtenir la même texture.

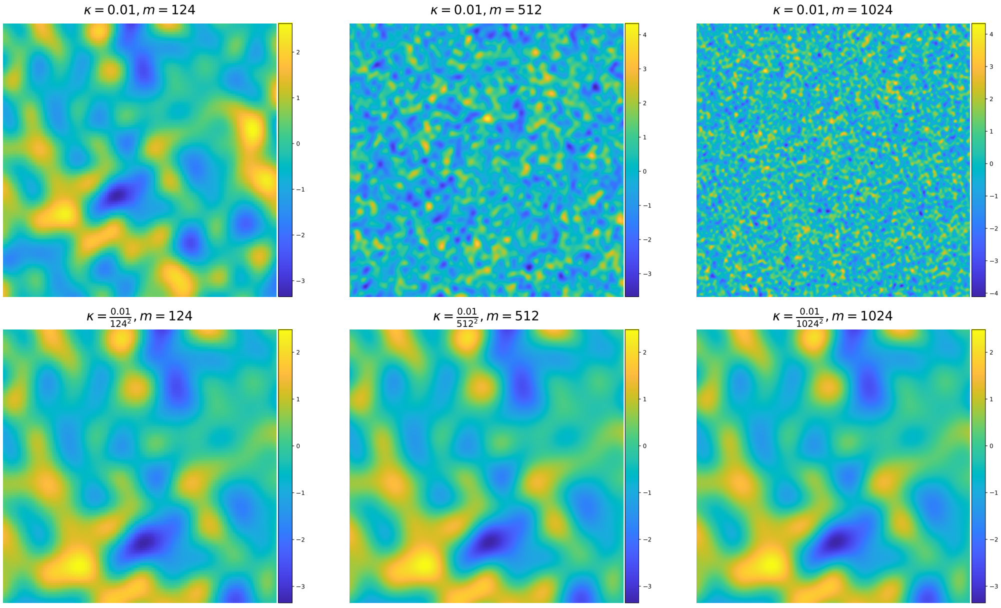

Figure 1.10 – Générations de champs aléatoires gaussiens avec différentes valeurs pour κ et m.

Modèle sphérique. Soit X un champ gaussien centré et isotrope avec une fonction de covariance sphérique donnée par $\rho(x) = (1 - 3||x||_2/2C + (||x||_2^3/2C^3)\mathbb{1}_{||x||_2 \leq C}$, pour $x \in \mathbb{R}^2$ et $C \in \mathbb{R}^+$ (voir Bulinski et al. (2012a)). La structure de dépendance est liée au paramètre C et est appelée C-dépendance, ce qui signifie que si $||x - y||_2 > C$, alors X_x et X_y sont des variables indépendantes.

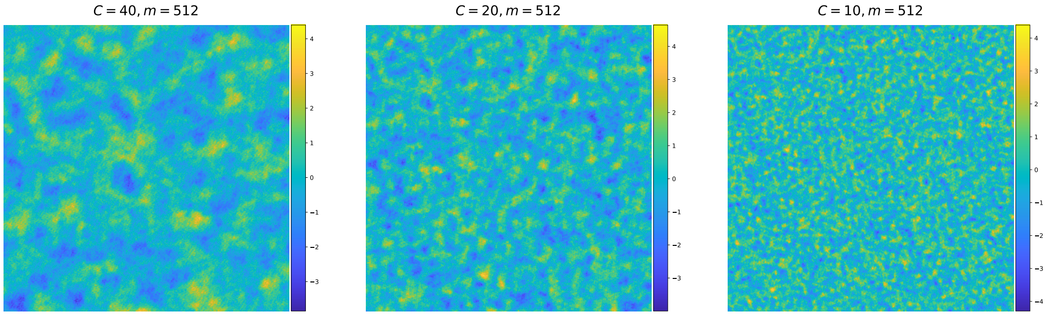

Figure 1.11 – Générations de champs aléatoires gaussiens avec $m = 512$ et une fonction de covariance sphérique pour différentes valeurs de C, de gauche à droite $C = 40, 20, 10$.

Modèle anisotrope. Tous les exemples présentés ci-dessus sont isotropes, ce qui signifie qu'ils sont invariants par rotations. En conséquence, leur fonction de covariance dépend uniquement de la distance entre les points du champ. La classe de champs aléatoires pour lesquels ce type d'invariance n'est pas vérifié est connue sous le nom de classe de champs aléatoires anisotropes. Une approche simple pour construire un champ aléatoire gaussien anisotrope consiste à considérer la classe des processus affines. Cette méthode consiste à appliquer une transformation affine à un champ aléatoire isotrope X pour briser la structure isotrope et imposer l'anisotropie. Soit $\{Y(x; a, b, \theta); x \in \mathbb{R}^2\}$ un champ aléatoire ayant la même distribution que $\{X(Ax); x \in \mathbb{R}^2\}$ (voir Cabaña (1987); Berzin (2021)), où

$$A := \begin{pmatrix} a & 0 \\ 0 & b \end{pmatrix} \begin{pmatrix} \cos(\theta) & \sin(\theta) \\ -\sin(\theta) & \cos(\theta) \end{pmatrix}, \tag{1.4}$$

avec $a, b \in \mathbb{R}^2, a, b \geq 0$ et $\theta \in [0, \pi)$. Le champ Y est également gaussien avec une fonction de covariance donnée par $\rho_Y(x) = \rho_X(Ax)$. Remarquons que $a \neq b$ si et seulement si Y est anisotrope.

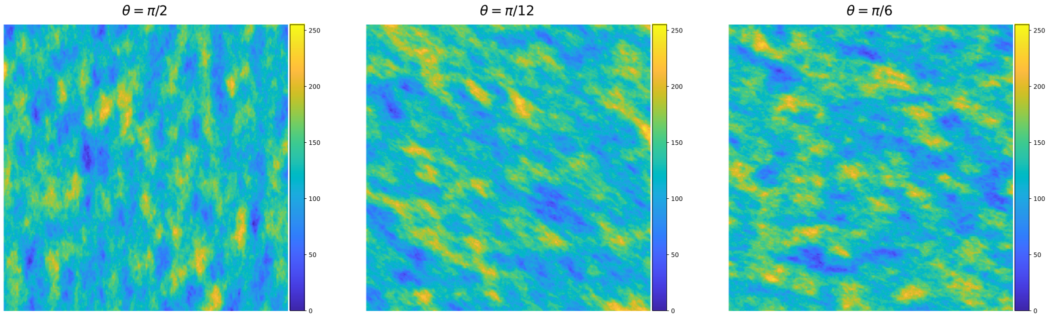

Figure 1.12 – Générations de champs aléatoires gaussiens avec $m = 512$ avec une fonction de covariance sphérique $\rho_Y = (1 - 3||Ax||_2/2C + ||Ax||_2)^3/2C^3)\mathbb{1}_{||Ax||_2 \leq C}$ avec $a = 1, b = 2$ et $C = 40$, pour différentes valeurs de θ de gauche à droite $\theta = \pi/2, \pi/12, \pi/6$.

Géométrie des champs aléatoires Dans le contexte des champs aléatoires stationnaires continus, des résultats très importants ont été obtenus, en particulier pour les champs Gaussiens (voir Adler and Taylor (2007)). Dans ce cadre, le calcul théorique des moyennes des courbures de Lipschitz-Killing des ensembles d'excursions a été explicitement réalisé par Wschebor (2006). Ces LKC moyennes peuvent être efficacement estimées à partir d'images, voir Biermé et al. (2019). L'estimation cohérente des variances associées a été étudiée récemment dans Di Bernardino and Duval (2020). De plus, des résultats du type Théorème Central Limite (TCL) Kratz and Vadlamani (2017); Bulinski et al. (2012b) ont ouvert la voie à des tests d'hypothèses statistiques.

En générale, les procédures de test nécessitent généralement l'observation du champ entier et/ou de copies indépendantes du champ ; l'étude de la géométrie du champ aléatoire nous permet d'adopter une approche parcimonieuse, car elle ne nécessite que l'observation d'un ou deux ensembles d'excursion au lieu du champ entier.

De nombreux résultats théoriques ont été établis dans le cadre des champs aléatoires continus. Les propriétés statistiques des LKC ont été étudiées dans divers cadre, et des résultats importants ont été obtenus, en particulier pour les champs aléatoires gaussiens. Nous renvoyons le lecteur à Bulinski et al. (2012b); Biermé and Desolneux (2016); Lachièze-Rey (2019a); Biermé and Lerbet (2022) pour davantage de références.

1.4 Nos contributions

1.4.1 Approche théorique

Suivant les travaux de Biermé and Desolneux (2021), notre objectif principal est d'explorer les propriétés statistiques du périmètre des ensembles d'excursion du champ aléatoire discrétisé $(X_x)_{x\in\mathbb{Z}^2}$.

Comme mentionné précédemment, le périmètre est une somme de fonctions dépendant des valeurs du champ X (plus précisément, des fonctions indicatrices qui interrogent la valeur de X en un point et la valeur de ses voisins directs). Du fait de sa nature en tant que somme de fonctions aléatoires, il devient possible de calculer ses moments et d'établir des théorèmes de type TCL pour tester et révéler certaines propriétés structurelles du champ X. Ces calculs deviennent souvent fastidieux, leur complexité et leur faisabilité étant influencées par les caractéristiques du champ X, en particulier sa structure de covariance. Par conséquent, au sein de cette étude, nous nous concentrons sur deux cadres particuliers. Le premier est un contexte de bruit blanc. Ce cadre nous permet d'éviter d'imposer des hypothèses spécifiques concernant la nature du champ (Gaussien, Uniforme...). Il est important de noter que même dans ce contexte, la structure du périmètre présente une faible dépendance (somme de variables 1-dépendantes), malgré l'absence de dépendance entre les pixels individuels. Le deuxième cadre est celui d'un champ aléatoire gaussien stationnaire, dans lequel nous pouvons imposer une condition faible sur la structure de covariance (conditions d'intégrabilité classiques).

Lors de l'étude des propriétés statistiques du périmètre, nous constatons qu'il renferme des caractéristiques pouvant être utilisées pour décrire la nature de la distribution du champ aléatoire qui l'a produit. Il imite la propriété de symétrie de la marginale dans le cadre du bruit blanc. De plus, dans le contexte des champs aléatoires gaussiens stationnaires, il est étroitement lié à la covariance dans les directions canoniques. Il est intéressant de noter qu'en réduisant le niveau de dépendance dans le champ, nous observons l'émergence de résultats qui se rapprochent du cas indépendant. Ces observations nous ont permis d'utiliser le périmètre comme une mesure pour tester ces deux propriétés dans leurs contextes respectifs.

Pour établir ces tests, il était crucial de calculer et de comprendre le comportement des premier et deuxième moments du périmètre. Cette compréhension nous a permis d'établir un Théorème Central Limite (multivarié) spécifiquement adapté à notre contexte.

Pour établir le premier théorème central limite multivarié pour le vecteur des périmètres pris à différents seuils, nous avons utilisé un résultat de Heinrich (1986), consacré aux sommes de variables m-dépendantes, où m désigne la portée de dépendance entre les variables, aucune hypothèse sur la distribution n'est requise. Le deuxième théorème central limite multivarié utilise un résultat de Arcones (1994) et n'est applicable que dans le cas de vecteurs gaussiens stationnaires avec une condition faible sur la fonction de covariance.

Voici un résumé concis des divers résultats présentés dans cette thèse, à la fois dans le cadre du bruit blanc et dans le cadre du champ gaussien stationnaire.

- Calcul du premier et du second moment du périmètre $\mathcal{P}_m^{(i)}(t)$ donné par l'équation (1.3) (voir Proposition 2.3.1 et Proposition 2.3.2 dans le chapitre 2 pour le modèle de bruit blanc et Proposition 3.3.1 et Proposition 3.3.2 dans le chapitre 3 pour le modèle gaussien stationnaire), et leurs expressions asymptotiques lorsque m tend vers l'infini.
- Établissement du théorème central limite multivarié adapté au vecteur $\left(\mathcal{P}_m^{(1)}(t_1), \ldots, \mathcal{P}_m^{(1)}(t_k), \mathcal{P}_m^{(2)}(t_1), \ldots, \mathcal{P}_m^{(2)}(t_k)\right)$, pour $t_1, \ldots, t_k \in \mathbb{R}$ pour différentes conditions sur la structure de covariance (voir Théorème 2.3.3 dans le chapitre 2 pour le modèle de bruit blanc et Théorème 3.3.8 dans le chapitre 3 pour le modèle gaussien stationnaire).
- Construction des tests statistiques, test de symétrie dans le cas du modèle de bruit blanc (voir Section 2.4.1 dans le chapitre 2) et test d'isotropie locale dans le contexte du modèle gaussien stationnaire (voir Section 3.3 dans le chapitre 3).

1.4.2 Approche numérique

En complément des résultats théoriques, nous avons mis en place plusieurs méthodes de calcul utilisant à la fois **Python** et **MATLAB** pour valider et illustrer les résultats à l'aide de données synthétiques. Ces implémentations ont permis de vérifier l'exactitude des résultats théoriques et leur conformité avec les données simulées. Plus précisément, nous avons développé un code pour calculer les premier et deuxième moments du périmètre $\mathcal{P}_m^{(i)}(t)$ ainsi que pour effectuer les simulations des tests statistiques proposés (voir Section 2.5 dans le chapitre 2 et Section 3.4 dans le chapitre 3).

1.4.3 Application aux données réelles

Après avoir mené des investigations théoriques et numériques, nous nous tournons vers l'utilisation du périmètre provenant d'images issues de données réelles (Section 3.6 dans le chapitre 3). Nous commençons par étudier l'anisotropie de la texture des images de radiographies osseuses, comme dans Biermé et al. (2009). Nous arrivons à la même conclusion : les images de radiographies du calcanéum présentent une nature anisotrope. Enfin, dans le dernier chapitre (chapitre 4) de cette thèse, nous explorons les potentialités des trois caractéristiques géométriques (aire, périmètre et caractéristique d'Euler) dans un contexte d'apprentissage automatique. L'objectif est d'évaluer leur efficacité pour résumer les caractéristiques géométriques complexes des données réelles dans le cadre d'une tâche de classification. À cet effet, nous considérons un ensemble de données d'images de cancer de la peau. Les résultats de classification obtenus à partir des caractéristiques LKC sont ensuite comparés à ceux obtenus à partir de techniques relevant du domaine de l'analyse de données topologiques (TDA). Il s'agit d'un domaine en plein essor qui vise à capturer des informations topologiques et géométriques pertinentes à partir de jeux de données, voir par exemple Chazal and Michel (2021); Garin and Tauzin (2019); Singh et al. (2023); Vandaele et al. (2022). En utilisant une méthode de forêt aléatoire pour la classification, nous réalisons une analyse comparative qui met en lumière les capacités respectives de ces approches pour capturer et représenter les aspects géométriques essentiels des images, ainsi que le potentiel de combiner les deux techniques pour améliorer les résultats de classification.

1.5 Travaux de la thèse

1. Le chapitre 2 reprend le travail présenté dans l'article (Abaach et al. (2021)), M. Abaach, H. Biermé, and E. Di Bernardino. Testing marginal symmetry of digital noise images through the perimeter of excursion sets. *Electronic Journal of Statistics*, 15(2): 6429 – 6460, 2021.

2. Le chapitre 3 reprend le travail présenté dans le préprint (Abaach et al. (2023)), M. Abaach, H. Biermé, E. Di Bernardino, and A. Estrade. Local isotropy test based on the oriented perimeter of digitalized images. Working paper, Mar. 2023. hal-04037394. URL https://hal.science/hal-04037394/.

3. Le chapitre 4 est un travail en collaboration avec Ian Morrilla, chercheur à l'Institut d'Horticulture Subtropicale et Méditerranéenne (IHSM), université de Málaga.

1 Introduction (english version)

In image processing, we can view an image as the realization of a 2d discretized random field which permits the setting of a convenient statistical framework allowing the analyzis of the images properties and characteristics and addressing multiple image processing challenges. These challenges include image denoising, pattern detection, segmentation, and classification (see, *e.g.* Blake et al. (2011); Jähne (2005)). More precisely, by using tools from the rigorous framework of stochastic geometry, we can understand and analyze the geometric properties of the underlying random field, and gain valuable insights into the image's structural elements thus enabling various machine learning tasks (N.M. van Lieshout (2009)).

However, directly studying the image's geometry poses challenges. Therefore, our approach is not a frontal one, instead, we opt to consider the set of thresholded images associated with an image, commonly called excursion sets. Hence, we obtain sparse information that captures the geometrical information of the image. To examine the characteristics to these black-and-white images, we can define three geometrical characteristics which are the surface area (number of white pixels in the black-and-white image), the perimeter (the length of the contour of the white part), and the Euler characteristic which is defined in our 2d context as the difference between the number of connected components and the number of holes in the black-and-white image. Each of the three functionals encapsulates essential information about the excursion set's geometric and topological characteristics, they are closely associated with the Minkowski functionals and are extensively studied in integral and stochastic geometry (Chiu et al. (2013)), they are also known as the Lipschitz-Killing curvatures (LKC) of excursion sets, we refer the reader to Adler (1981) or Thäle (2008) for a formal introduction to the subject. These functionals serve as an effective shape descriptors and find applications in various domains, to name a few: cosmology (Schmalzing and Górski (1998)), medicine (brain imaging, Flandin and Friston (2015), and the study of synthesized 2d digital mammograms, Biermé et al. (2019)).

We first start by introducing the theoretical framework to model images using random fields.

1.1 From a random field to binary images

1.1.1 Rigorous construction of the binary image

Let m be an integer with $m \geq 2$. Without loss of generality, we consider our observation window as the square $S = [0, m]^2$ and we divide it into m^2 pairwise disjoint squares. We denote by e_1, e_2 the elements of the canonical basis of $\mathbb{R}^2$ and we introduce the following notations.

- $\mathbb{G}_m$ is the set of points in S with integer coordinates in $[0, m)$, we write $x = (x_1, x_2)$ with $x_1, x_2 \in \{0, \ldots, m-1\}$ for any $x \in \mathbb{G}_m$.
- For $x \in \mathbb{G}_m$, $C_m(x) := x + \left[0, 1\right]^2$ will be referred to as a *cell*, (*i.e*, pixel). Note that $S \ = \cup_{x \in \mathbb{G}_m} C_m(x)$.
- We denote by $\mathcal{E}_m^{(1)}$, $\mathcal{E}_m^{(2)}$ the set of vertical and horizontal edges in $\mathring{S}$ as presented in Figure 1.1, respectively red and blue segments.

Figure 1.1 shows an example of a square tiling with $m = 4$.

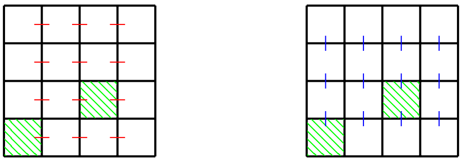

Figure 1.1 – Square tiling for $m = 4$ and associated cells $C_4((0, 0))$ and $C_4((2, 1))$ (green stripes). We represent the vertical edges in red and the horizontal ones in blue.

Using the previous square tiling, we observe an image $I : x \in \mathbb{G}_m \to \mathbb{R}$ and considering a threshold parameter $t \in \mathbb{R}$, we introduce the associated binary image, see Figure 1.2, where each cell (pixel) $C_m(x)$ within the image I is assigned either a black or white color, depending on whether $I_x \geq t$ or $I_x < t$. The set of cells $C_m(x)$ for which $I_x \geq t$ is known in the literature as the excursion set or upper-level set of I at threshold level t and is often denoted by $E_I(t)$. In Figure 1.2, we represent a grayscale image, its 3d representation and its associated thresholded image for $t = 87$.

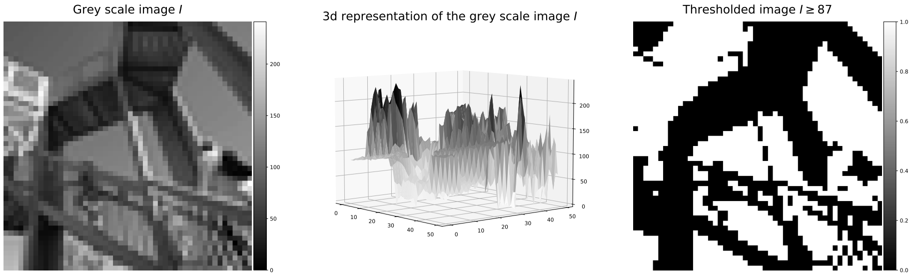

Figure 1.2 – An image I, its 3d representation of the image, and the corresponding thresholded image for $t = 87$.

Random fields are commonly used to model images as it gives a nice theoretical framework that succeeds to capture the dependencies between neighboring pixels or regions in the image.

1.1.2 Random Fields

A random field can be viewed as a stochastic process, usually taking real values and defined over a parameter space of dimension at least 1 (we refer the reader to Adler and Taylor (2007); Biermé (2017) for a thorough introduction). In the course of our study, the parameter space is $\mathbb{Z}^2$. In general, random fields are mathematical functions that assign random values to points within a parameter space. In our case, we consider the random field X on a discrete grid that can only be observed within the scope of a bounded window S and that takes values in $\mathbb{R}$. Thus, we look at the field X as a random pixelated image, where each pixel is assigned a random real value.

An important class of random fields is the class of stationary random fields which means that they are invariant in regard to translation; this property makes them widely used for modeling homogeneous regions and textures. More precisely, the stationarity hypothesis states that for all $h \in \mathbb{Z}^2$,

$$\left(X_{x+h}; x \in \mathbb{Z}^2\right) \overset{fdd}{=} \left(X_x; x \in \mathbb{Z}^2\right),$$

where fdd denotes finite-dimensional distributions.

Hence, using the previously introduced framework, we observe the image I, which we assume coincides with the values of a realization of a stationary random field $(X_x)_{x \in \mathbb{Z}^2}$ defined on a probability space, such that $I_x = X_x(w)$. Given a threshold parameter $t \in \mathbb{R}$, we consider the associated black-and-white image, by applying the procedure we described above.

Figure 1.3 displays several generations of random fields and their associated thresholded images.

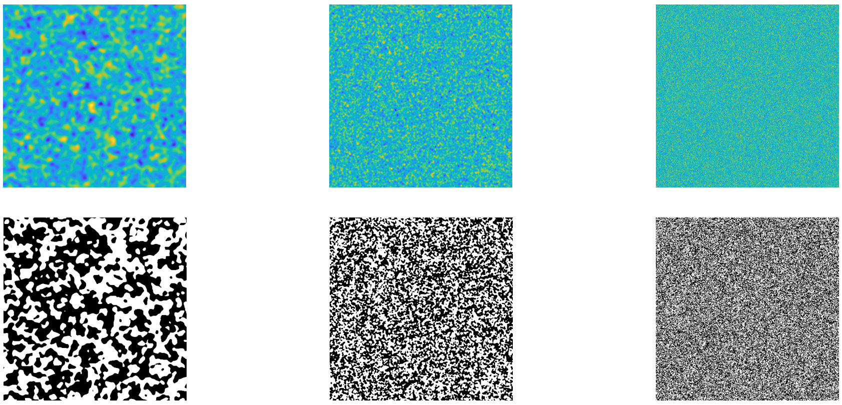

Figure 1.3 – Generation of three random fields (first row) and their respective thresholded image for $t = 0$ and $m = 512$ (second row).

As stated before, one way to access the geometry of a set is by exploring the behavior of its associated Lipschitz-Killing curvatures: area, perimeter, and the Euler characteristic. Specifically, the area provides insights into the density of occupation within the set, the perimeter offers indications of its regularity or smoothness, and the Euler characteristic, which is also a topological invariant, quantifies its connectivity or the presence of holes.

For each threshold value t, we can compute the perimeter of the associated binary image, thus defining the random function, $\mathcal{P}_m : t \mapsto \mathcal{P}_m(t)$ that is the perimeter of the excursion sets of the random field $(X_x)_{x \in \mathbb{G}_m}$. In this thesis, we focus on studying the statistical behavior of the perimeter and uncovering the structures it inherits from the underlying random field.

1.2 Oriented perimeter of a binary image

1.2.1 Formal definition

Following the approach presented in Biermé and Desolneux (2021), for each edge $w \in \mathcal{E}_m = \mathcal{E}_m^{(1)} \cup \mathcal{E}_m^{(2)}$, we aim to know whether w contributes to the perimeter of the black component set (see Figure 1.4). Making use of the additive nature of the perimeter, one can start by computing the oriented perimeter given each direction, horizontal and vertical.

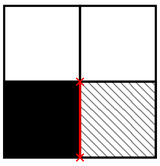

Figure 1.4 – The edge w in red belongs to $C_2((0,0)) \cap C_2((1,0))$, with the cell $C_2((0,0))$ colored in black and $C_2((1,0))$ in gray dashed stripes.

Following this remark, for a fixed threshold t, considering the binary image

$$Z_t^m = \left(\mathbb{1}_{\{X_x \geq t\}}\right)_{x \in \mathbb{G}_m}, \tag{1.1}$$

one can define the random quantity,

$$f_t^{(i)}(x) := \mathbb{1}_{\{\min(X_x, X_{x+e_i}) < t \leq \max(X_x, X_{x+e_i})\}}, \qquad x \in \mathbb{G}_m^{(i)}, \quad \text{for } i \in \{1,2\} \tag{1.2}$$

in order to take into account the eventual contribution of the edge w in the intersection of the two cells, $C(x)$ and $C(x+e_j)$, to the perimeter of the black component of $Z_t^{(m)}$. Let us now introduce the main tool of the present work.

Definition 1.2.1 (Oriented perimeter)**.**
For $t \in \mathbb{R}$, we denote by $\mathcal{P}_m^{(i)}(t)$ the sum of all contributions over the ith direction (vertical for $i = 1$ and horizontal for $i = 2$) and we call it the oriented perimeter of the binary image $Z_t^{(m)}$,

$$\mathcal{P}_m^{(i)}(t) = \sum_{x \in \mathbb{G}_m^{(i)}} f_t^{(i)}(x). \tag{1.3}$$

The perimeter of $Z_t^{(m)}$ is given by $\mathcal{P}_m(t) := \mathcal{P}_m^{(1)}(t) + \mathcal{P}_m^{(2)}(t)$.

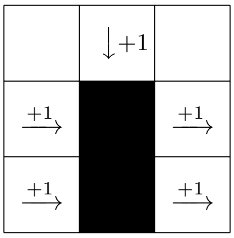

Figure 1.5 – Computation of the perimeter of a binary image with $m = 3$. Here $\mathcal{P}_3^{(1)} = 4$ and $\mathcal{P}_3^{(2)} = 1$.

Below, we present an algorithm to compute the perimeter of a binary image *e.g* Figure 1.2 that implements Definition 1.2.1, for M, N being the width and length of the image, in the context of our work we assume that $M = N = m$.

Algorithm 2 Perimeter of a binary image computation using Equation (1.3)

```
Initialization Binary image $Z$ of shape $(M, N)$,
Do $L_1 = \mathrm{sum}((Z[0:M-1, 0:N] == 1) \times (Z[1:M, 0:N] == 0))$
    $L_2 = \mathrm{sum}((Z[0:M, 0:N-1] == 1) \times (Z[0:M, 1:N] == 0))$
    $L_3 = \mathrm{sum}((Z[0:M-1, 0:N] == 0) \times (Z[1:M, 0:N] == 1))$
    $L_4 = \mathrm{sum}((Z[0:M, 0:N-1] == 0) \times (Z[0:M, 1:N] == 1))$
    $P_1 = L_1 + L_3$
    $P_2 = L_2 + L_4$
Return $P_1 + P_2$
```

1.2.2 Biases

Before going further, it is essential to note that viewing the random field as a bounded pixelated image and not as the continuous infinite entity that it is, entails a couple of biases.

The first bias is linked to the discretization problem, and the second one due to is the bounded window S in which we observe the field.

THE DISCRETIZATION PROBLEM The term *bias* refers to the pixelization error that arises numerically due to the discretized representation of images. The initial hypothesis we made is that the studied image I is considered to correspond to the observable values of the realization of a continuous random field X on the discrete window S. As we assume that the image $I_x = X_x$ with x taken on a discrete grid, we introduce biais *e.g.* Figure 1.2 depicts a discretized snapshot of a real-world phenomenon that is inherently continuous). Most of the literature that studies these geometrical feature (Azaïs and Wschebor (2009); Kratz and Vadlamani (2017)) relies on strong assumptions on the smoothness of the underlying random fields. The field is often assumed to have smooth trajectories (C^k, $k \geq 1$). In practice, we do not have access to the continuous underlying object, as it is not empirically accessible. We can only access the function taken at points on the discrete grid $\mathbb{G}_m$. Consequently, the obtained excursion sets are discretized, and vertical and horizontal edges form their boundary. However, these edges do not accurately represent the true boundary of the object. This introduces a bias discussed in Biermé and Desolneux (2021); they study how the mean perimeter of excursion sets over a set of thresholds changes when considering discretized versions (square and hexagonal tiling) of the underlying stationary, isotropic random fields. They show in particular that, in expectation, under some stationarity and isotropy conditions on the random field, the perimeter is always biased (with a $4/\pi$ factor) in a dense tiling context when converging towards the continuous underlying object. Cotsakis et al. (2022a) derive an explicit formula for the bias, showing that it solely depends on the spatial dimension d, which allows them to establish an unbiased estimator for the perimeter of excursion sets that are approximated by general tessellations of polytopes in $\mathbb{R}^d$. Cotsakis et al. (2022b) proposes a method to compute an unbiased estimator for the perimeter of excursion sets of random fields on $\mathbb{R}^2$ observed over regular square tilings, by introducing diagonals. The construction of the estimator does require prior tuning and loses the additive property of the perimeter which makes its statistics harder to access.

BOUNDARY BIAS When studying the perimeter of excursion sets in images, a natural bias arises due to the finite nature of the domain S, thus introducing an artificial border. However, this bias decreases as the size of the domain m goes to infinity. In order to address this bias, Biermé et al. (2019) proposed a correction method that utilizes additional geometric features available in 2d settings, namely the area and the Euler characteristic. They construct an unbiased estimator of the perimeter by incorporating the other geometrical characteristics using the kinematic formula (see *e.g.* Theorem 15.9.5 in Adler and Taylor (2007); Schneider and Weil (2008)). Another approach to correcting the bias involves treating one side's edge as if it wraps around to the opposite edge, known as toroidal correction. Alternatively, when dealing with large datasets, an effective correction method excludes points near the boundary while estimating the features.

Using random fields to model images gives a way to describe the spatial relationships between pixels and the image's smoothness or texture. Getting back to thresholded image $Z_t^{(m)}$, see Equation (1.1), for each $x \in \mathbb{G}_m$, $Z_t^{(m)}(x)$ follows a Bernoulli distribution of parameter $\mathbb{P}(X_x \geq t)$. In the next section, we will study how the relationship between the pixels, which is dictated by the dependence structure of the field X, impacts the geometry of the black and white image $Z_t^{(m)}$ and the structure of its perimeter as well!

1.3 Dependence structure and geometry

What governs the notion of field dependence is the covariance structure $K(s,t) = \text{Cov}\,(X_t, X_s)$, which encapsulates the kind of relationship that the pixels will have. There are many ways to define the covariance structure K, but there are two general conditions that it must verify. It has to be symmetrical, meaning that $\forall s,t \in \mathbb{Z}^2, K(s,t) = K(t,s)$ and non-negative definite: $\forall k \geq 1, t_1, \ldots, t_k \in \mathbb{Z}^2, \lambda_1, \ldots, \lambda_k \in \mathbb{R}$, $\sum_{i,j=1}^{k} \lambda_i \lambda_j K(t_i, t_j) \geq 0$.
In the scope of this work, we only consider stationary random fields. Thus, there exists a function $\rho : \mathbb{Z}^2 \to \mathbb{R}$ such that for all $s, t \in \mathbb{Z}^2$, $\rho(t-s) = \text{Cov}\,(X_t, X_s)$. We focus on unit variance, $i.e$ $\rho(0) = 1$.
By abuse of notation, when the field is also isotropic (invariant in regard to rotation), ρ is often regarded as a function of the distance between the point, mapping $\mathbb{R}^+$ to $\mathbb{R}$.

1.3.1 Dependence range

The covariance function ρ captures the spatial information of the field and describes the kind of relationship a pixel has with its neighbors. When assigning values to pixels, an intuitive approach would be to assign to each pixel a value without considering the values of neighboring pixels. Each pixel follows a marginal distribution. Thus its value is determined by the realization of a 1D variable. In that case, the pixels are independent of one another, and the covariance value between them equals 0. Such a random field is known as white noise, as depicted in Figure 1.6. We use a Gaussian model for the illustrations.

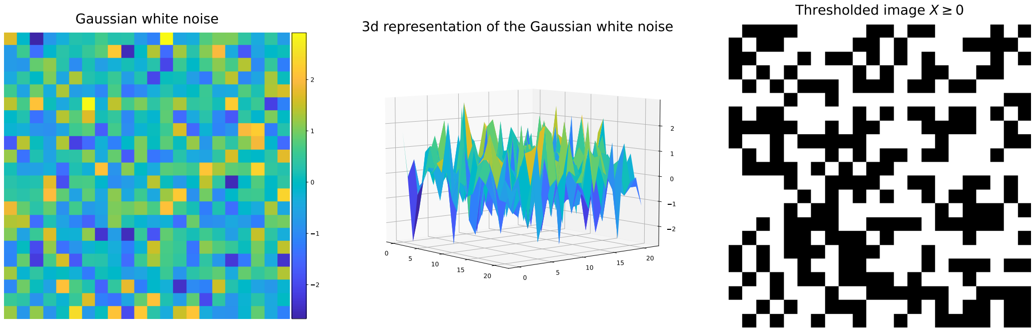

Figure 1.6 – Realization of Gaussian white noise, $m = 22$.

The other possible way to assign pixel values is to make them fully dependent, which means that the value of its neighbors entirely determines the pixel's value. Consequently, knowing the value of one pixel determines the values of all the others. That particular case corresponds to a covariance value equal to 1 due to normalization. In that case, the field behaves as a single random variable.

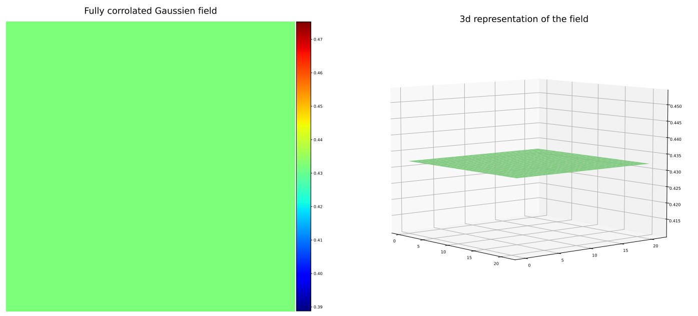

Figure 1.7 – Realization of a fully correlated Gaussian random field, $m = 22$.

We can see that Figure 1.6 and Figure 1.7 represent two extremes; in the first case ($\forall x \in \mathbb{Z}^2 \setminus \{(0,0)\}, \rho(x) = 0$), with each pixel behaving independently, it leaves no space for any semblance of order or discernible pattern, just plain noise. In the second case ($\rho \equiv 1$), an excessive degree of order dominates the field, leaving no room for spontaneity or variation, leading to perfectly structured plain images. A middle ground exists, and between these two extremes lies a whole world of possibilities of shapes and forms, and the covariance function of the field governs all of it. In a sense, covariance measures the deviation from spatial randomness, and deciding on the kind of covariance function we use entirely changes the nature of the structures we obtain. A very important class of random fields is the Gaussian random fields which is a statistical tool to describe a wide range of natural structures, encompassing diverse applications such as electronics, geography, machine learning, and cosmic phenomena. The unique aspect of Gaussian random fields lies in their ability to capture essential properties of various natural structures while being very easy to manipulate since they are fully characterized by their first and second moment, making them favorable for theoretical analyses. Using a Gaussian random field to model an image means that all its pixels follow a Gaussian distribution and that all finite linear combination of pixels are also Gaussian. Centered Gaussian random fields are completely characterized by their covariance function ρ. We are mainly interested in the local behavior of the covariance, meaning the relationship of the dependence between a pixel and its 4 closest neighbors. In general, we range between the two extremes above.

In Figure 1.8, we consider an isotropic model, and we are interested in exhibiting the local influence of the value of the covariance $\rho(e_i)$, the value of the covariance between a pixel and its neighbor, on the nature of the structures that we observe on the image. The closer $\rho(e_i)$ is to 1, the more we observe the apparition of regular "continuous" patterns in the image and well of values meaning a neighborhood of pixels that approximately have the same value. Conversely, the closer $\rho(e_i)$ is to 0, the lesser structure the image has.

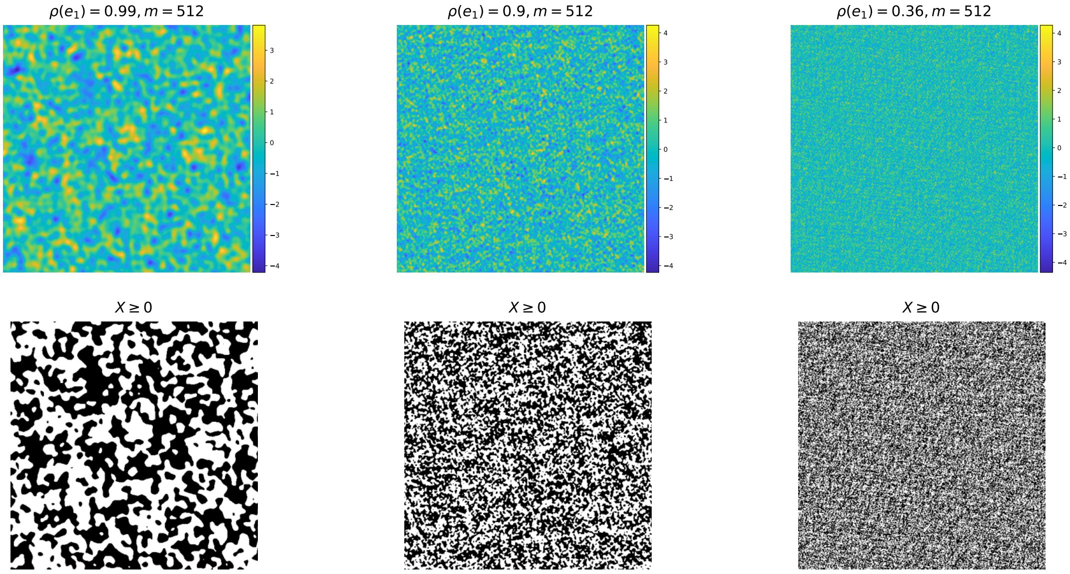

Figure 1.8 – Generations of Gaussian random fields that have the same kind of covariance function but with different value of $\rho(e_i)$.

1.3.2 Gaussian parametric models

Simulation of random fields is a widely explored subject in research, with numerous numerical tools available in the literature. In this thesis, we utilize two specific tools for generating the images. Firstly, we used the Python package **GeoStatTools** Müller et al. (2022), which offers a range of geostatistical tools, including generating random fields. This package facilitates the generation process by providing many covariance models and allowing users to plug in the covariance functions of their choice. We refer the interested reader to Müller et al. (2022) for more information on the generation method. Additionally, we use the Matlab function **stationary_Gaussian_process** in the second chapter of this thesis to generate a Gaussian random field. This function employs the circulant matrix method to generate the random field, the user is required to provide the covariance function.

In the figures below, we present examples of the realization of Gaussian random fields, with two covariance models and different degrees of dependence.

BERGMANN-FOCK GAUSSIAN FIELD. The most commonly used covariance model is $\rho(x) = \exp(-\kappa ||x||_2^2)$, for $x \in \mathbb{R}^2$ and $\kappa \in \mathbb{R}^+$ and $||.||_2$ designating the Euclidean norm of $\mathbb{R}^2$.

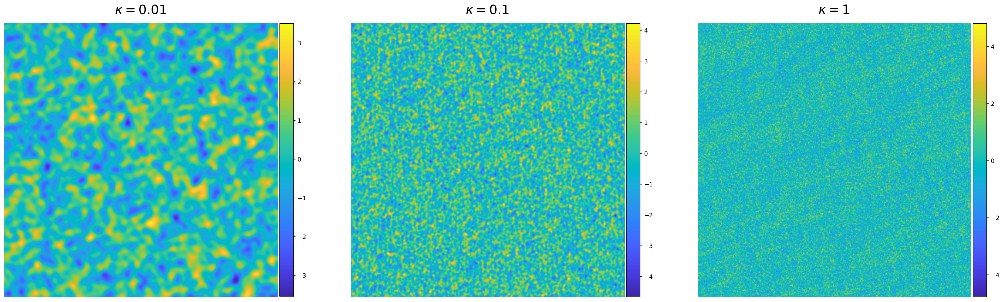

Figure 1.9 – Generations of Gaussian random fields with $m = 512$ and from left to right $\kappa = 0.01, 0.1, 1$.

As we can observe in Figure 1.9, as the value of the parameter κ decreases (*e.g.*, left image), the dependence structure in the field becomes more prominent, revealing larger and more discernible patterns in the image. The parameter κ has a scaling effect and is closely associated with the image's resolution. We illustrate the impact of the choice of κ and m in Figure 1.10. In the first row, we fix the value of κ and change the value of m to demonstrate the zooming effect. In the second row, we set the seed of the algorithm (the randomness) to showcase the effect, altering the value of m while adjusting κ to achieve a consistent texture.

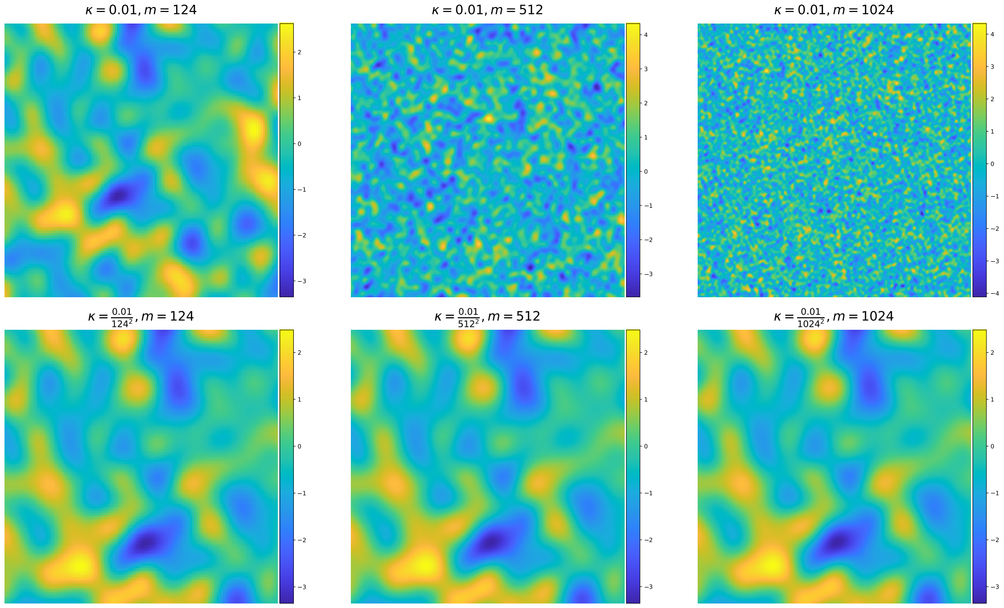

Figure 1.10 – Generations of Gaussian random fields with different values for κ and m.

SPHERICAL MODEL. Let X be a stationary, isotropic centered Gaussian field with a spherical covariance function given by $\rho(x) = (1 - 3||x||_2/2C + (||x||_2^3/2C^3)\mathbb{1}_{||x||_2 \leq C}, x \in \mathbb{R}^2$ and $C \in \mathbb{R}^+$ (see Bulinski et al. (2012a)). The dependence structure is linked to the parameter C and is called C-dependence, meaning that if $||x - y||_2 > C$, then X_x and X_y are independent variables.

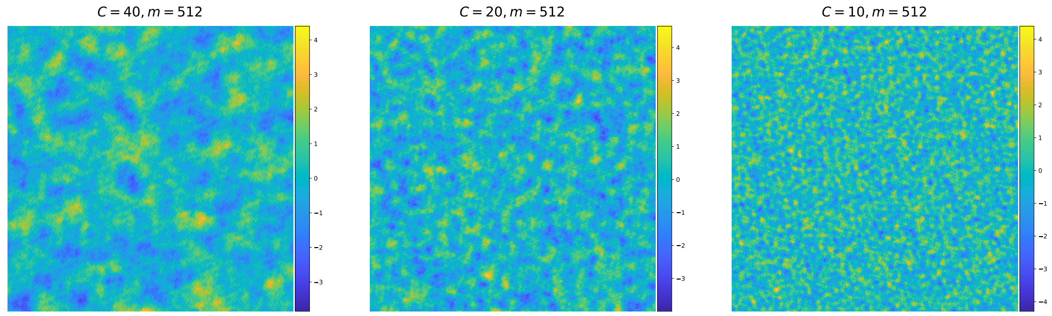

Figure 1.11 – Generations of Gaussian random fields with $m = 512$ with a spherical covariance function for different values of C, from left to right $C = 40, 20, 10$.

ANISOTROPIC MODEL. All the examples presented above exhibit the isotropic property, meaning they are invariant under rotations. Consequently, their covariance function solely depends on the distance between the points of the field. The class of random fields for which that kind of invariance does not hold is known as the anisotropic random fields class. One straightforward approach to constructing an anisotropic Gaussian random field involves considering the class of affine processes. This approach entails applying an affine transformation to an isotropic random field X to break the isotropy structure and enforce anisotropy. Let $\{Y(x; a, b, \theta); x \in \mathbb{R}^2\}$, be a random field equal in distribution to $\{X(Ax); x \in \mathbb{R}^2\}$ (see Cabaña (1987); Berzin (2021)), where

$$A := \begin{pmatrix} a & 0 \\ 0 & b \end{pmatrix} \begin{pmatrix} \cos(\theta) & \sin(\theta) \\ -\sin(\theta) & \cos(\theta) \end{pmatrix}, \tag{1.4}$$

with $a, b \in \mathbb{R}^2, a, b \geq 0$ and $\theta \in [0, \pi)$. The field Y is also Gaussian with covariance function given by $\rho_Y(x) = \rho_X(Ax)$. Note that $a \neq b$ if and only if Y is anisotropic.

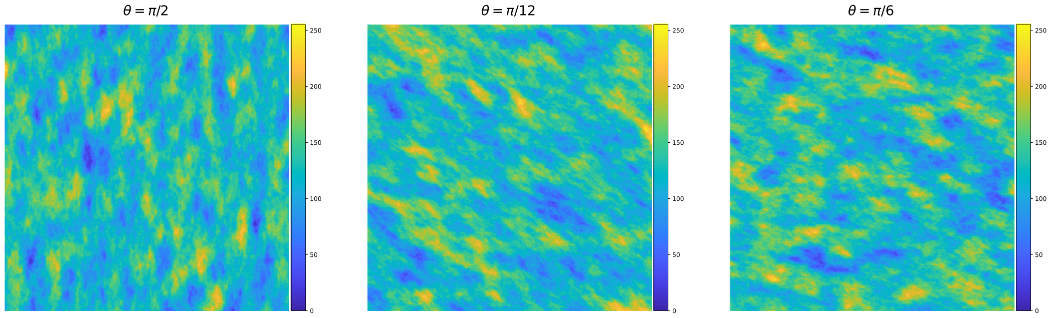

Figure 1.12 – Generations of Gaussian random fields with $m = 512$ with a spherical covariance function $\rho_Y(x) = (1 - 3||Ax||_2/2C + ||Ax||_2)^3/2C^3)\mathbb{1}_{||Ax||_2 \leq C}$ with $a = 1, b = 2$ and $C = 40$ and for different values of θ, from left to right $\theta = \pi/2, \pi/12, \pi/6$.

GEOMETRY OF RANDOM FIELDS In the context of smooth stationary random fields, very important results have been obtained, especially for Gaussian related fields (see Adler and Taylor (2007)). Within this framework, the theoretical computation of the expected Lipschitz-Killing curvatures with respect to the field parameters has been explicitly conducted Wschebor (2006) and can be efficiently estimated from images Biermé et al. (2019). The consistent estimation of related variances has been recently studied in Di Bernardino and Duval (2020). Moreover, Central Limit Theorems (CLT) Kratz and Vadlamani (2017); Bulinski et al. (2012b) that paved the road for statistical hypothesis tests. Besides, testing procedures usually require the observation of the entire field and/or independent copies of the field; studying the geometry of the random field allow us to adopt a sparse approach since it only requires one or two excursion sets instead of the whole field. Many theoretical results have been established in the framework of smooth random fields. The LKC's statistical properties have been studied in various frameworks, and important results have been obtained, especially for Gaussian random fields, shot noise, among many we refer the reader to Bulinski et al. (2012b); Biermé and Desolneux (2016); Lachièze-Rey (2019a); Biermé and Lerbet (2022).

1.4 Our contributions

1.4.1 Theoretical approach

Following the work of Biermé and Desolneux (2021), our primary focus lies in exploring the statistical properties exhibited by the perimeter of the excursion sets of the discretized random field $(X_x)_{x\in\mathbb{Z}^2}$. As stated above, the perimeter equals a sum of functions taking values over the field X (more precisely, indicator functions that interrogate the value of X on a position and the value of its direct neighbor). Given its nature as a sum of random functions, it becomes possible to compute its moments and establish Central Limit Theorems to test and uncover some structural properties of the field X. However, these computations can often become tedious, with their complexity and feasibility being influenced by the characteristics of the field X, particularly its covariance structure. Consequently, within this study we position ourselves within two distinct frameworks. The first is a context of white noise. This covariance-free framework allows us to avoid imposing any specific assumptions regarding the nature of the field (Gaussian, uniform...). It is important to note that even within this context, the structure of the perimeter still exhibits weak dependence (sum of 1-dependent variables), despite the absence of dependence between individual pixels. In the second framework is a stationary Gaussian random field framework under which we could impose a weak condition on the covariance structure (classical integrability conditions).

When studying the statistical properties of the perimeter, we exhibit that it encloses features that can be used to describe the nature of the distribution of the random field that produced it. It mimics the symmetrical property of the marginal in the case of white noise. Besides, in the context of stationary Gaussian random fields, it becomes closely linked to the covariance of the canonical directions. It is interesting to note that as we reduce the level of dependence in the field, we observe the emergence of results that align with the independent case. These observations allowed us to use the perimeter as a measure to test for these two properties within their respective contexts.

To establish these tests, it was crucial to compute and understand the behavior of the first and second moments of the perimeter. This understanding paved the way for establishing a multivariate Central Limit Theorem specifically tailored to the perimeter.

To establish the first multivariate Central Limit Theorem for the vector of perimeters taken at different thresholds, we used a result from Heinrich (1986), established for sums of m-dependent variables, m denotes the range of dependence among the variables, no assumption on the distribution is required. The second multivariate Central Limit Theorem uses a result from Arcones (1994) and is applicable only in the case of stationary Gaussian sequences of vectors with a weak condition on the covariance function of the field.

Below is a concise summary of the diverse results presented in this dissertation in both the white noise and stationary Gaussian frameworks.

- Computation of the first and second moment of the perimeter $\mathcal{P}_m^{(i)}(t)$, Equation (1.3) (see Proposition 2.3.1 and Proposition 2.3.2 in Chapter 2 for the white noise model and Proposition 3.3.1 and Proposition 3.3.2 in Chapter 3 for the Gaussian one), and their asymptotic expressions as m goes to ∞.
- Establishing the adapted multivariate Central Limit Theorem for the vector $\left(\mathcal{P}_m^{(1)}(t_1), \ldots, \mathcal{P}_m^{(1)}(t_k), \mathcal{P}_m^{(2)}(t_1), \ldots, \mathcal{P}_m^{(2)}(t_k)\right)$, for $t_1, \ldots, t_k \in \mathbb{R}$ for different conditions on the covariance structure (see Theorem 2.3.3 in Chapter 2 for the white noise model and Theorem 3.3.8 in Chapter 3 for the Gaussian one).
- Constructing the statistical tests, symmetry test in the case of a white noise model (see Section 2.4.1 in Chapter 2) and the local isotropy test in the context of the stationary Gaussian framework model (see Section 3.3 in Chapter 3).

1.4.2 Numerical approach

Following the theoretical findings, we implement several computational methods using both **Python** and **MATLAB** to validate the results using synthetic data. These implementations assessed the accuracy of the theoretical results and verified their conformity with the simulated data. Specifically, we develop a code to compute the first and second moments of the perimeter $\mathcal{P}_m^{(i)}(t)$ alongside the execution of simulations of the proposed statistical tests (see Section 2.5 in Chapter 2 and Section 3.4 in Chapter 3).

1.4.3 Application to real-world data

After completing the theoretical and numerical investigations, we shift focus towards using the perimeter of images from real-world data (Section 3.6 in Chapter 3). We start by investigating the anisotropy of the texture of bone X-ray images as in the work of Biermé et al. (2009). We arrive at the same conclusion: the calcaneus X-ray images exhibit an anisotropic nature. Finally, in the last chapter (Chapter 4) of this dissertation, we explore the potential of using all three geometrical features (area, perimeter, and Euler characteristic) in a machine-learning context. The objective is to evaluate their effectiveness in summarizing the intricate geometric characteristics of real-world data through a classification task. For that effect, we consider a dataset of skin cancer images. The classification results obtained from the LKC features are then compared to those obtained from techniques within the realm of Topological Data Analysis. It is a fast growing field that aims at capturing relevant topological and geometric information from datasets Chazal and Michel (2021); Garin and Tauzin (2019); Singh et al. (2023); Vandaele et al. (2022). Using a Random Forest method for classification, we perform a comparative analysis that sheds new light on the respective capabilities of these approaches in capturing and representing the essential geometric aspects of the images and the potential of combining both techniques to improve the classification results.

1.5 Thesis work

1. Chapter 2 resumes the work presented in the published article (Abaach et al. (2021)), M. Abaach, H. Biermé, and E. Di Bernardino. Testing marginal symmetry of digital noise images through the perimeter of excursion sets. *Electronic Journal of Statistics*, 15(2): 6429 – 6460, 2021.
2. Chapter 3 resumes the work presented in the preprint (Abaach et al. (2023)), M. Abaach, H. Biermé, E. Di Bernardino, and A. Estrade. Local isotropy test based on the oriented perimeter of digitalized images. working paper, Mar. 2023. hal-04037394. URL https://hal.science/hal-04037394/.
3. Chapter 4 is an ongoing work in collaboration with Ian Morrilla, researcher at the Institute of Subtropical and Mediterranean Horticulture (IHSM), university of Málaga.

2 WHITE NOISE FRAMEWORK

This chapter resumes the work presented in the published article (Abaach et al. (2021)), M. Abaach, H. Biermé, and E. Di Bernardino. Testing marginal symmetry of digital noise images through the perimeter of excursion sets. *Electronic Journal of Statistics*, 15(2): 6429 – 6460, 2021.

2.1 Introduction

The stochastic modeling of images by spatial random fields allows to set up a convenient statistical framework for different issues in image processing for image denoising, pattern detection, segmentation or classification Pratt (1978); Jähne (2005); Desolneux (2019).

A particular interest directed towards the study of geometric attributes and features of objects has grown these last years. Roughly speaking the considered quantities are the surface area, perimeter and Euler characteristic, which is a topological invariant that is equal to the number of connected components minus the number of holes, in a black and white binary image obtained by thresholding a gray image at some fixed level. These quantities are related to intrinsic volumes and Minkowski functionals particularly studied in the integral and stochastic geometry Chiu et al. (2013); Schneider and Weil (2008) or Lipschitz-Killing (LK) curvatures of excursion sets (see Thäle (2008) for a formal introduction to the subject). Those functionals are robust and efficient shape descriptors that have been largely applied to a variety of domains: cosmology (*e.g.* the morphological analysis of cosmic microwave background Schmalzing and Górski (1998); Marinucci (2004); Casaponsa et al. (2016)), astrophysics (*e.g.* modeling galaxy formation Gott et al. (2008)), military (*e.g.* mine field detection, Lake and Keenan (1995)) medicine (*e.g.* brain imaging, Flandin and Friston (2015), study of synthesized 2D digital mammograms, Biermé et al. (2019); Di Bernardino and Duval (2020)).

Very important results have been obtained in the framework of smooth stationary random fields, especially for Gaussian related fields (see Adler (1981)). In this framework, the theoretical means of LK curvatures are explicitly computed with respect to the parameters of the fields Wschebor (2006); Worsley (1994); Azaïs and Wschebor (2009) and can be efficiently estimated from images Biermé et al. (2019). The consistent estimation of related variances had been recently studied in Di Bernardino and Duval (2020). Moreover, Central Limit Theorems (CLT) have been proven for Gaussian fields Estrade and León (2016); Kratz and Vadlamani (2017) that paved the road for statistical hypothesis tests. Several extensions for non-Gaussian fields, namely shot noise random fields are also available for means of LK curvatures Lachièze-Rey (2019a) and associated CLT's Lachièze-Rey (2019b). However the framework of smooth fields, indexed by continuous space variables, is not appropriate with the discrete framework induced by digital images. Let us remark that links with discrete setting have been recently explored in Biermé and Desolneux (2021).

In this paper we consider this discrete framework for digital images for which white noise is well defined. More precisely, we assume that pixels values are given by $(X_{i,j})_{i,j\geq 1}$ a sequence of independent and identically distributed (*i.i.d.*) variables within an observation window S. We have in mind the residuals of a denoising procedure or a linear regression, or the difference between two images as for brain activities study. Therefore, we are interested to test the natural symmetry hypothesis, that is to know whether $X_{i,j}$ is drawn from a symmetrical distribution. This assumption of marginal distribution symmetry is called here the *null hypothesis* H_0 and includes Gaussian or Student distributions. Being able to formally test for symmetry hypotheses is an important topic in many fields since this basic assumption contains important information regarding the underlying model, that would allow to validate it before further investigation.

This problem has been largely considered in the literature for *i.i.d.* sample, especially due to its importance for time series analysis. Different approaches to construct a symmetry test include the use of empirical distribution for known center of symmetry Butler (1969), the characteristic symmetry function and study of its behavior to know if the distribution is symmetric or not Csörgő and Heathcote (1987) with unknown center. Other tests rely on the study of the skewness of the distribution function as initiated by Gupta (1967); see Mira (1997) for a free-distribution test based on Bonferroni's measure. For an overview and comparison of the existing methods we refer to Quessy (2016) and Ivanovic et al. (2020).

In our original approach we attempt to use our digital image setting and the geometrical features of its excursion sets. More precisely, for a given threshold $t \in \mathbf{R}$ we consider the binary image given by the *i.i.d.* Bernoulli variables $(\mathbb{1}_{\{X_{i,j}\geq t\}})_{i,j\geq 1}$, coloring black pixels for values equal to one and considering the area of black components as well as its perimeter inside a given domain. This allows us to build an *unbiased* estimator of the perimeter, without border effects. This framework is close from the one used by Ebner et al. (2018) to set up a goodness of fit test for complete spatial randomness. In the aforementioned paper the authors consider the counting process obtained from a homogeneous Poisson point process such that the observed values $(X_{i,j})$ are *i.i.d.* Poisson random variables. They obtain explicit expectation and covariance matrix for the three Lipschitz-Killing curvatures at a fixed level as well as CLT to build their test. In the present paper, we focus on the perimeter and obtain a multivariate CLT with respect to several threshold levels with an explicit covariance matrix, under a general *i.i.d.* assumption, in a dense tiling framework. The choice of our unbiased perimeter estimator permits us to preserve the symmetry of the distribution, in contrast with perimeter with border. This lead us to construct the statistical test of symmetry, by considering the behavior of the ratio between two specific thresholds. We also explore the asymptotic in large threshold limit regime and obtain the equivalence between the asymptotic behavior of the expectation value and the variance establishing a joint auto-normalized Central Limit Theorem for dense tiling and large threshold limit regime in a white noise framework, similarly to Dalmao et al. (2017) for crossings in dimension 1.

The paper is organized as follows. In Section 2.2 we introduce our mathematical framework for binary images and we proceed to the construction of an unbiased estimator for the associated perimeter. Then, in Section 2.3 we study the first and second moments of the perimeter, which allows us to prove asymptotic normality results with an explicit covariance matrix, for which we consider several consistent estimators. The construction of our consistent symmetry test via empirical accessible test statistics is proposed in Section 2.4. Numerical evaluations are presented in Section 2.5. The case of large threshold values is investigated in Section 2.6, that yields to a new a central limit theorem and test statistics illustrated with numerical comparisons. Finally, we postpone the technical proofs to Section 2.7, and additional numerical evaluations to the Appendix.

2.2 Mathematical framework

2.2.1 Construction of the binary image

SQUARE TILING Let m be an integer with $m \geq 2$, without loss of generality, we consider our observation window as the unit square $S = [0,1]^2$ and we divide our window into m^2 pairwise disjoint squares. This provides a regular tiling of S with squares of "size" (side length) $1/m$, *i.e.*,

$$C_{i,j}^{(m)} := \left[\frac{i-1}{m}, \frac{i}{m}\right] \times \left[\frac{j-1}{m}, \frac{j}{m}\right], \quad \text{for } i,j \in \{1,\dots,m\}.$$

The $C_{i,j}^{(m)}$ will be referred to as *cells*. We denote by $\mathcal{E}_m$ the set of edges in $\mathring{S} = (0,1)^2$, each $w \in \mathcal{E}_m$ is a segment of length $1/m$.

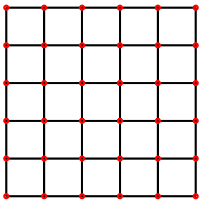

Figure 2.1 – Tilling with squares for $m = 5$ and associated vertices (red circles).

Discrete setting Using the previous square tiling, we write $S = \underset{1 \le i,j \le m}{\cup} C^m_{i,j}$. Let $(X_{i,j})_{1 \le i,j \le m}$ be a sequence of random variables defined over the same probability space $(\Omega, \mathcal{A}, \mathbb{P})$, that are independent and identically distributed. Each pixel value $X_{i,j}$ is associated to the cell $C^{(m)}_{i,j}$. In Figure 2.2, $X_{i,j} \sim \mathcal{U}(0,1)$ and $m = 20$.

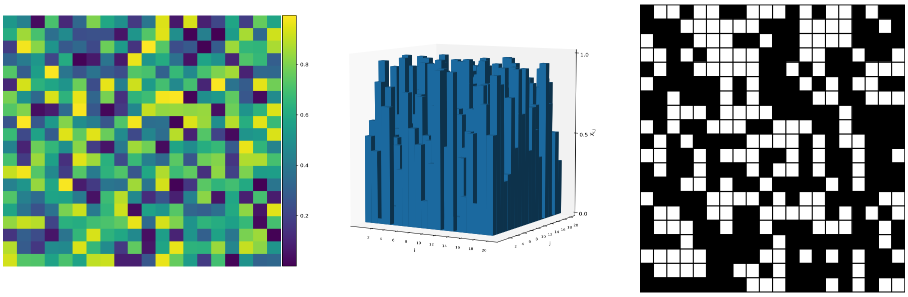

Figure 2.2 – Left and center panels: Image of size (20×20) realization of a Uniform white noise model. Right panel: Obtained binary image for $t = 0.5$.

Let us consider a threshold parameter $t \in \mathbb{R}$. In order to create the associated binary image, we introduce a random $m \times m$-matrix $Z(t) = (Z_{i,j}(t))_{1 \le i,j \le m}$, where

$$Z^{(m)}_{i,j}(t) := \mathbb{1}_{\{X_{i,j} \ge t\}}, \quad \text{for} \quad i, j \in \{1, \dots, m\}.$$

Each cell $C^{(m)}_{i,j}$ is associated to black or white according to whether $Z_{i,j}(t) = 0$ or $Z_{i,j}(t) = 1$. Then, $Z_{i,j}(t)$ follows a binomial distribution of parameter $(1, p_t)$, where

$$p_t := \mathbb{P}(Z_{i,j}(t) = 1) = \mathbb{P}(X_{i,j} \ge t) = 1 - F(t^-),$$

with F the cumulative distribution function associated to $X_{i,j}$.

2.2.2 Perimeter of a binary image

Let $Z = Z(t)$ be the binary image Z at that given threshold $t \in \mathbb{R}$. Following the approach presented in Biermé and Desolneux (2021), for each edge $w \in \mathcal{E}_m$, we aim to know if w contributes to the perimeter of the black component of Z. Let w be a horizontal edge of the form $w = \left(\frac{l-1}{m}, \frac{l}{m}\right) \times \{\frac{k-1}{m}\}$, w belongs to both cells $C_{l,k-1}$ and $C_{l,k}$, which means that w is a contribution to the perimeter if $Z_{l-1,k} \neq Z_{l,k}$. Following this consideration, one can consider

$$f_1^{(t)}(l,k) = \mathbb{1}_{\{(Z_{l,k-1}(t)=0 \,\cap\, Z_{l,k}(t)=1) \,\cup\, (Z_{l,k-1}(t)=1 \,\cap\, Z_{l,k}(t)=0)\}}$$

to count the horizontal contributions and

$$f_2^{(t)}(k,l) = \mathbb{1}_{\{(Z_{k-1,l}(t)=0 \,\cap\, Z_{k,l}(t)=1) \,\cup\, (Z_{k-1,l}(t)=1 \,\cap\, Z_{k,l}(t)=0)\}}$$

to count the vertical ones.

Definition 2.2.1 (Perimeter and scaled perimeter of a binary image)**.** *We denote by* $\mathcal{P}^{(1)}_m(t) = \sum_{l=1}^m \sum_{k=2}^m f_1^{(t)}(l,k)$ *the sum of all horizontal contributions and* $\mathcal{P}^{(2)}_m(t) =$

$\sum_{l=1}^{m}\sum_{k=2}^{m} f_2^{(t)}(k,l)$ *the sum of the vertical ones, then, the perimeter and scaled perimeter are given by*

$$\mathcal{P}_m(t) := \mathcal{P}_m^{(1)}(t) + \mathcal{P}_m^{(2)}(t), \qquad \check{\mathcal{P}}_m(t) := \frac{1}{m^2}\left(\mathcal{P}_m^{(1)}(t) + \mathcal{P}_m^{(2)}(t)\right). \tag{2.1}$$

An equivalent way to compute the perimeter is by considering, for each edge w, the maximal and minimal values on the two sides of w. Then, the perimeter is equivalently given by

$$\mathcal{P}_m(t) := \sum_{w \in \mathcal{E}_m} \left(f_+^{(t)}(w) - f_-^{(t)}(w)\right), \tag{2.2}$$

where $f_+^{(t)}(w) = \max(Z_{l,k-1}(t), Z_{l,k}(t))$ and $f_-^{(t)}(w) = \min(Z_{l,k-1}(t), Z_{l,k}(t))$ for w the common edge between $C_{l,k-1}$ and $C_{l,k}$. The interested reader is referred to Biermé and Desolneux (2021). The only edges $w \in \mathcal{E}_m$ that contribute to the computation are those for which $f_+^{(t)}(w) = 1$ and $f_-^{(t)}(w) = 0$ which are exactly the edges belonging to the perimeter intersected with the interior of our observation window.

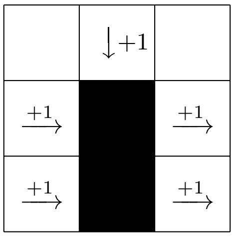

Figure 2.3 – Computation of the perimeter of a binary image with $m = 3$. Here $\mathcal{P}_3 = 5$.

Algorithm 3 Perimeter of a binary image computation using Equation (2.2)

```
Initialization Binary image $Z$ of shape $(M, N)$,
Do $L_1 = \mathrm{sum}((Z[0:M-1, 0:N] == 1) \times (Z[1:M, 0:N] == 0))$
   $L_2 = \mathrm{sum}((Z[0:M, 0:N-1] == 1) \times (Z[0:M, 1:N] == 0))$
   $L_3 = \mathrm{sum}((Z[0:M-1, 0:N] == 0) \times (Z[1:M, 0:N] == 1))$
   $L_4 = \mathrm{sum}((Z[0:M, 0:N-1] == 0) \times (Z[0:M, 1:N] == 1))$
   $P_1 = L_1 + L_3$
   $P_2 = L_2 + L_4$
Return $P_1 + P_2$
```

Remark 1. Notice that the proposed method in Definition 2.2.1(see Equation (2.2)) does not take into account the contribution of the edges that belongs to the frontier of the observation window S. Indeed, in Algorithm 3, the border cells can only contribute to the perimeter with one or two edges contrary to the other cells that can have up to four edges contributing to the perimeter. In this sense this method is *unbiased* in comparison with Ebner et al. (2018)'s technique. In the aforementioned paper, the authors introduce a white artificial frontier around the image and then, compute the perimeter of the extended new image (white frontier included), making all cells contributing to the perimeter have a four edge contribution.

2.3 Statistics of the perimeter of a binary image

2.3.1 Moments and asymptotic normality

In this section we investigate the first and second moments of the perimeter. This preliminary study will be useful to state our multivariate Central Limit Theorem (see Theorem 2.3.3 below).

Proposition 2.3.1 (First moment of the perimeter)**.** *The expected value of the scaled perimeter in* (2.1) *is given by*

$$\mathbb{E}(\check{\mathcal{P}}_m(t)) = 4p_t(1-p_t)\left(1-\frac{1}{m}\right) := \mu_{\check{\mathcal{P}}}(p_t, m). \tag{2.3}$$

The proof of Proposition 2.3.1 is postponed to Section 2.7.

Remark 2. Assume that $X_{i,j}$ is drawn from a symmetrical continuous distribution of axis $\theta \in \mathbb{R}$, *i.e* $p_{\theta-t} = 1 - p_{\theta+t}$, $\forall t \in \mathbb{R}$. Then, $\mu_{\check{\mathcal{P}}}(p_{\theta-t}, m) = \mu_{\check{\mathcal{P}}}(p_{\theta+t}, m)$ and therefore, $t \mapsto \mu_{\check{\mathcal{P}}}(p_t, m)$ has an axis of symmetry on θ. This implies that the ratio $(\check{\mathcal{P}}_m(\theta-t))/(\check{\mathcal{P}}_m(\theta+t))$ would be distributed around 1 in the case of symmetry. This consideration will be crucial for the proposed symmetry testing procedure in Section 2.4.

We now study the second moment of the perimeter of the considered binary image.

Proposition 2.3.2 (Covariance between perimeters at two thresholds)**.** *Let $t, s \in \mathbb{R}$ be two given thresholds. The covariance between the scaled perimeter taken at levels t and s is given by*

$$\begin{aligned} Cov\left(\check{\mathcal{P}}_m(t), \check{\mathcal{P}}_m(s)\right) = \frac{4}{m^4} & p_{\max(t,s)}(1-p_{\min(t,s)})\Big((4m^2-7m+2) \\ & - 2p_{\min(t,s)}(1-p_{\max(t,s)})(7m^2-13m+4) \\ & + 2(p_{\min(t,s)} - p_{\max(t,s)})(3m^2-6m+2)\Big). \end{aligned}$$

Taking $t = s$, we obtain the following variance formula

$$\begin{aligned} Var(\check{\mathcal{P}}_m(t)) &= \frac{4}{m^4} p_t(1-p_t)\left((4m^2-7m+2) - 2p_t(1-p_t)(7m^2-13m+4)\right) \\ &:= \sigma^2_{\check{\mathcal{P}}}(t,m). \end{aligned} \tag{2.4}$$

The proof of Proposition 2.3.2 is postponed to Section 2.7. If we add in Proposition 2.3.2 the bias induced by the boundary of the window S to the variance computation, we obtain the same results as those provided in Ebner et al. (2018) (see Theorem 4.1).

Beyond Propositions 2.3.1 and 2.3.2, we can prove the multivariate asymptotic normality as $m \to \infty$ of our geometrical feature for a given vector of thresholds.

Theorem 2.3.3 (Multivariate CLT for r-thresholds)**.** *Let r be a positive integer, $m \geq 2$ and $t_1, \ldots, t_r \in \mathbb{R}$, then,*

$$m\left(\begin{pmatrix} \check{\mathcal{P}}_m(t_1) \\ \check{\mathcal{P}}_m(t_2) \\ \vdots \\ \check{\mathcal{P}}_m(t_r) \end{pmatrix} - \begin{pmatrix} \mathbb{E}(\check{\mathcal{P}}_m(t_1)) \\ \mathbb{E}(\check{\mathcal{P}}_m(t_2)) \\ \vdots \\ \mathbb{E}(\check{\mathcal{P}}_m(t_r)) \end{pmatrix}\right) \xrightarrow[m\to\infty]{d} \mathcal{N}\left(0, \Sigma_r^{\star}\right),$$

where $\xrightarrow{d}$ *holds for the convergence in distribution and* $\mathcal{N}(0, \Sigma_r^\star)$ *for the* r*-dimensional centered Gaussian distribution with covariance matrix* $\Sigma_r^\star$ *given by*

$$\Sigma_r^\star(i,j) := 4p_{\max(t_i,t_j)}(1-p_{\min(t_i,t_j)})\Big(4 - 14p_{\min(t_i,t_j)}(1-p_{\max(t_i,t_j)}) \\ + 6(p_{\min(t_i,t_j)} - p_{\max(t_i,t_j)})\Big). \tag{2.5}$$

The proof of Theorem 2.3.3 is postponed to Section 2.7. Furthermore, some numerical illustrations of Theorem 2.3.3 in the case $r = 2$ can be found in Appendix 2.A1. Finally, as can be seen in (2.5), the last theoretical result that will be needed for the construction of an empirical accessible test statistic is an estimation of p_t. This will be discussed in the next section.

2.3.2 Two consistent estimators for p_t.

In the following, we will present two estimators and study their consistency properties. In this section, for the sake of clarity, we denote $p(t) := p_t$, $\forall\, t \in \mathbb{R}$.

One way to estimate $p(t)$ is by considering the area of the excursion set. Another idea for the estimation of $p(t)$ is built on the relationship that exists between the expectation value of the perimeter at a level t and $p(t)$ (see Equation (2.3)):

$$\mathbb{E}\left(\frac{\check{\mathcal{P}}_m(t)}{(1-\frac{1}{m})}\right) = 4p(t)(1-p(t)). \tag{2.6}$$

Definition 2.3.4 (Area and perimeter based estimator for $p(t)$)**.** *Given a threshold* $t \in \mathbb{R}$*, we define*

$$\hat{p}_m^{\mathcal{A}}(t) = \frac{1}{m^2}\sum_{i,j=1}^{m} Z_{i,j}(t).$$

Besides, we partition the image S *in* $m^2/4$ *sub-images* S_2^i *of size* (2×2)*. We denote by* $\check{\mathcal{P}}_2^i(t)$ *the value of the scaled perimeter for each sub-image. Let* $\overline{S}_m(t) := \frac{4}{m^2}\sum_i \check{\mathcal{P}}_2^i(t)$ *and the continuous mapping* $g : [0,1] \to \mathbb{R}$ *defined by*

$$x \mapsto g(x) = \begin{cases} \dfrac{1}{2}\big(1 - \sqrt{1-2x}\big) & \text{if } x < \frac{1}{2}, \\ \dfrac{1}{2} & \text{else.} \end{cases}$$

Then, for $t > \theta$ *with* θ *the median value of the distribution, we define the perimeter based estimator of* $p(t)$ *as*

$$\hat{p}_m^{\mathcal{P}}(t) := g(\overline{S}_m(t)).$$

Proposition 2.3.5 (Asymptotic normality for the proposed estimators for $p(t)$)**.** *Let* $\hat{p}_m^{\mathcal{A}}(t)$ *and* $\hat{p}_m^{\mathcal{P}}(t)$ *as in Definition 2.3.4. Then, it holds that*

$$\hat{p}_m^{\mathcal{A}}(t) \xrightarrow[m\to\infty]{a.s} p(t) \quad \text{and} \quad m\left(\hat{p}_m^{\mathcal{A}}(t) - p(t)\right) \xrightarrow[m\to\infty]{d} \mathcal{N}(0, p(t)(1-p(t))).$$

Similarly, it holds

$$\hat{p}_m^{\mathcal{P}}(t) \xrightarrow[m\to\infty]{a.s} p(t)$$

and

$$m\left(\hat{p}_m^{\mathcal{P}}(t)-p(t)\right)\xrightarrow[m\to\infty]{d}\mathcal{N}\left(0,\frac{p(t)(1-p(t))\Big(1-3p(t)(1-p(t))\Big)}{4(1-2p(t))^2}\right).$$

The proof of Proposition 2.3.5 is postponed to Section 2.7.

Remark 3. It is also possible to estimate $p(t)$ for $t<\theta$ by considering the continuous mapping $h:[0,1]\to\mathbb{R}$, $x\mapsto h(x)=\begin{cases}\frac{1}{2}\big(1+\sqrt{1-2x}\big) & \text{if } x<\frac{1}{2},\\ \frac{1}{2} & \text{else,}\end{cases}$ and applying the same procedure.

2.4 Perimeter based symmetry test

As previously discussed in Remark 2, we now aim to build a test using the specific structure of the mean perimeter in the case of symmetry. Let $I=\left\{x\in\mathbb{R},0<p(x)<\frac{1}{2}\right\}$ and $I_\theta=I-\theta$, it follows that

$$\forall\, t\in I_\theta,\ 0<p(\theta+t)<\frac{1}{2}.$$

A TEST STATISTIC Following the idea in Biermé et al. (2019) we propose a method to test the symmetry of the marginal distribution marginal of the field at equidistant levels from the median.

Let us consider the null hypothesis for $t\in I_\theta$

$$H_0(t)\quad:\quad p_{\theta-t}=1-p_{\theta+t},$$

where θ is the median value of the distribution. Let us first present a normality asymptotic result in the general case and a second result under the null hypothesis.

Proposition 2.4.1 (Ratio between perimeters at two thresholds)**.** *Let $t_1\in\mathbb{R}$ and $t_2\in I$ with $t_1<t_2$, and $\check{\mathcal{P}}_m(\cdot)$ be the scaled perimeter in Definition 2.2.1 computed for each threshold. Then, it holds that,*

$$m\left(\frac{\check{\mathcal{P}}_m(t_1)}{\check{\mathcal{P}}_m(t_2)}-\frac{\mu_{\check{\mathcal{P}}_m}(t_1)}{\mu_{\check{\mathcal{P}}_m}(t_2)}\right)\xrightarrow[m\to\infty]{d}\mathcal{N}\left(0,\tilde{\sigma}^2(t_1,t_2)\right),$$

with $\tilde{\sigma}^2(t_1,t_2)=\dfrac{p_{t_1}(1-p_{t_1})}{(p_{t_2}(1-p_{t_2}))^3}\Big(p_{t_2}(1-p_{t_2})-2p_{t_2}(1-p_{t_1})-3p_{t_2}(p_{t_1}-p_{t_2})(1-p_{t_1})+p_{t_1}(1-p_{t_1})\Big)$.

Let $t\in\mathcal{I}_\theta$ and $R_{m,\theta}(t):=\dfrac{\check{\mathcal{P}}_m(\theta-t)}{\check{\mathcal{P}}_m(\theta+t)}$. Then, under $H_0(t)$, it holds that

$$m\left(R_{m,\theta}(t)-1\right)\xrightarrow[m\to\infty]{d,H_0}\mathcal{N}\left(0,\sigma^2(\theta+t)\right),\tag{2.7}$$

with $\sigma^2(\theta+t)=\dfrac{(2p_{\theta+t}-1)(3p_{\theta+t}-2)}{p_{\theta+t}(1-p_{\theta+t})^2}$.

We postpone the proof of Proposition 2.4.1 in Section 2.7.

2.4.1 Proposed test with asymptotic level α

Let $\alpha \in (0,1)$ and $q_{1-\alpha/2}$ such that $\mathbb{P}(\mathcal{N}(0,1) \leq q_{1-\alpha/2}) = 1 - \alpha/2$. Then, using Proposition 2.4.1, we define the statistic of the test with asymptotic level α,

$$\phi^{\mathcal{P}}_m(\sigma) = \mathbb{1}_{\left\{|\frac{m}{\sigma(\theta+t)}(R_{m,\theta}(t)-1)| \geq q_{1-\alpha/2}\right\}}. \tag{2.8}$$

Firstly, we study the consistency of the proposed test statistic (see Proposition 2.4.2 below). Secondly, we focus on some estimation procedures for $\sigma(\theta+t)$ (see Section 2.4.2).

Let $t \in \mathcal{I}_\theta$ and $H_1(t)$ be the alternative hypothesis

$$H_1(t) \quad : \; p_{\theta-t} \neq 1 - p_{\theta+t}.$$

Proposition 2.4.2 (Consistency of the proposed symmetry test)**.** *For* $t \in \mathcal{I}_\theta$*, it holds that* $\mathbb{P}_{H_1(t)}(\phi^{\mathcal{P}}_m(\sigma) = 1) \to 1$ *for* $m \to \infty$*, with* $\phi^{\mathcal{P}}_m(\sigma)$ *as in Equation* (2.8)*.*

We postpone the proof of Proposition 2.4.2 in Section 2.7.

2.4.2 Empirical accessible test statistic

Notice that, if we take a consistent empirical estimator $\hat{\sigma}_m(\theta+t)$ of the variance of the considered ratio at level $\theta+t$, then, we can consider the empirical accessible test statistic

$$\phi^{\mathcal{P}}_m(\hat{\sigma}) = \mathbb{1}_{\left\{|\frac{m}{\hat{\sigma}_m(\theta+t)}(R_{m,\theta}(t)-1)| \geq q_{1-\alpha/2}\right\}}. \tag{2.9}$$

Using the estimators of $p(t)$ presented in Proposition 2.3.5, we can now construct estimators of the variance of the ratio to built $\phi^{\mathcal{P}}_m(\hat{\sigma})$ in (2.9).

Proposition 2.4.3 (Plug-in variance estimators)**.** *Let* $\hat{p}_m(\theta+t)$ *be a consistent estimator of* $p(\theta+t)$ *(i.e* $\hat{p}_m(\theta+t) \to p(\theta+t)$*, a.s.) and* $\sigma(\theta+t)$ *as in Proposition 2.4.1. We define*

$$\hat{\sigma}_m(\theta+t) := \sqrt{\frac{(2\hat{p}_m(\theta+t)-1)(3\hat{p}_m(\theta+t)-2)}{\hat{p}_m(\theta+t)(1-\hat{p}_m(\theta+t))^2}}. \tag{2.10}$$

Then, $\hat{\sigma}_m(\theta+t) \xrightarrow[m\to\infty]{a.s.} \sigma(\theta+t)$ *and*

$$\frac{m}{\hat{\sigma}_m(\theta+t)}(R_{m,\theta}(t)-1) \xrightarrow[m\to\infty]{d,H_0} \mathcal{N}(0,1). \tag{2.11}$$

The proof of Proposition 2.4.3 is postponed to Section 2.7.

Corollary 2.4.4. *Using the same framework as in Proposition 2.4.3, we denote by* $\hat{\sigma}^{\mathcal{P}}_m(\theta+t)$ *and* $\hat{\sigma}^{\mathcal{A}}_m(\theta+t)$ *the plug-in estimators based on Equation* (2.10) *using respectively* $\hat{p}^{\mathcal{P}}_m(\theta+t)$ *and* $\hat{p}^{\mathcal{A}}_m(\theta+t)$ *as in Proposition 2.3.5. Then,* $\hat{\sigma}^{\mathcal{P}}_m(\theta+t)$ *and* $\hat{\sigma}^{\mathcal{A}}_m(\theta+t)$ *are two consistent estimators of* $\sigma(\theta+t)$ *and asymptotic normality in* (2.11) *holds for these two estimators.*

Thus, from Corollary 2.4.4 and using Equation (2.9), we get two empirical accessible test statistics

$$\phi_m^{\mathcal{P}}(\hat{\sigma}^{\mathcal{P}}) = \mathbb{1}_{\left\{|\frac{m}{\hat{\sigma}_m^{\mathcal{P}}(\theta+t)}(R_{m,\theta}(t)-1)| \geq q_{1-\alpha/2}\right\}} \tag{2.12}$$

and

$$\phi_m^{\mathcal{P}}(\hat{\sigma}^{\mathcal{A}}) = \mathbb{1}_{\left\{|\frac{m}{\hat{\sigma}_m^{\mathcal{A}}(\theta+t)}(R_{m,\theta}(t)-1)| \geq q_{1-\alpha/2}\right\}}. \tag{2.13}$$

2.4.3 Comparison with Kolmogorov-Smirnov based estimator

Remark that under $H_0(t)$, the cumulative distribution function F satisfies $F(\theta - t) = 1 - F(\theta + t)$. Then, considering the empirical cumulative distribution function $t \mapsto \hat{F}_m(t) := \dfrac{1}{m^2}\sum_{i,j} \mathbb{1}_{X_{i,j} \leq t}$, which is a robust estimator of F, one can build an alternative symmetry test. Let us note that $\hat{F}_m(t^-) = 1 - \hat{p}_m^{\mathcal{A}}(t)$ with $\hat{p}_m^{\mathcal{A}}(t)$ as in Definition 2.3.4.

Proposition 2.4.5. *Let $t \in (0, \infty)$. Under $H_0(t)$, it holds that*

$$m\left(\frac{1-\hat{p}_m^{\mathcal{A}}(\theta - t)}{\hat{p}_m^{\mathcal{A}}(\theta + t)} - 1\right) \xrightarrow[m\to\infty]{d,H_0} \mathcal{N}\left(0, (\sigma^{\text{k-s}})^2(\theta + t)\right), \tag{2.14}$$

with $(\sigma^{\text{k-s}})^2(\theta + t) = \frac{2}{p(\theta+t)}$.

The proof of Proposition 2.4.5 is postponed to Section 2.7.
Let us denote

$$\hat{\sigma}_m^{\text{k-s}}(\theta + t) = \sqrt{\frac{2}{\hat{p}_m^{\mathcal{A}}(\theta + t)}} \quad \text{and} \quad R_{m,\theta}^{\text{k-s}}(t) := \frac{1-\hat{p}_m^{\mathcal{A}}(\theta - t)}{\hat{p}_m^{\mathcal{A}}(\theta + t)}.$$

One can provide an alternative Kolmogorov-Smirnov based test statistic with asymptotic level α

$$\phi_m^{\text{k-s}}(\hat{\sigma}^{\text{k-s}}) = \mathbb{1}_{\left\{|\frac{m}{\hat{\sigma}_m^{\text{k-s}}(\theta+t)}(R_{m,\theta}^{\text{k-s}}(t)-1)| \geq q_{1-\alpha/2}\right\}}. \tag{2.15}$$

Remark 4. In particular for $s \in I$ we can prove that $\sigma^2(s) < \sigma^2_{\text{k-s}}(s)$, where $\sigma^2(s)$ is given by (2.7) and $\sigma^2_{\text{k-s}}(s)$ by (2.14), as shown in Figure 2.11 in Appendix 2.A2. Then, the perimeter based test has a smaller variance than the alternative Kolmogorov-Smirnov one.

2.5 Some numerical studies for the proposed symmetry test

In this section, we report simulation results for our symmetry test, for samples of 500 images of size $m \times m$, for $m = 100, 512, 1024$ and different choices of threshold level. Firstly, we display the results for three symmetrical distributions (Gaussian, Student and Uniform distributions, see Figure 2.4) and three asymmetrical ones (Exponential, Chi-squared and Skew-normal distributions, see Figure 2.5).

For a better approximation of θ, we use the mean estimator provided by the `NumPy` library, making use of the fact that for a symmetrical distribution it is equivalent to use the mean or

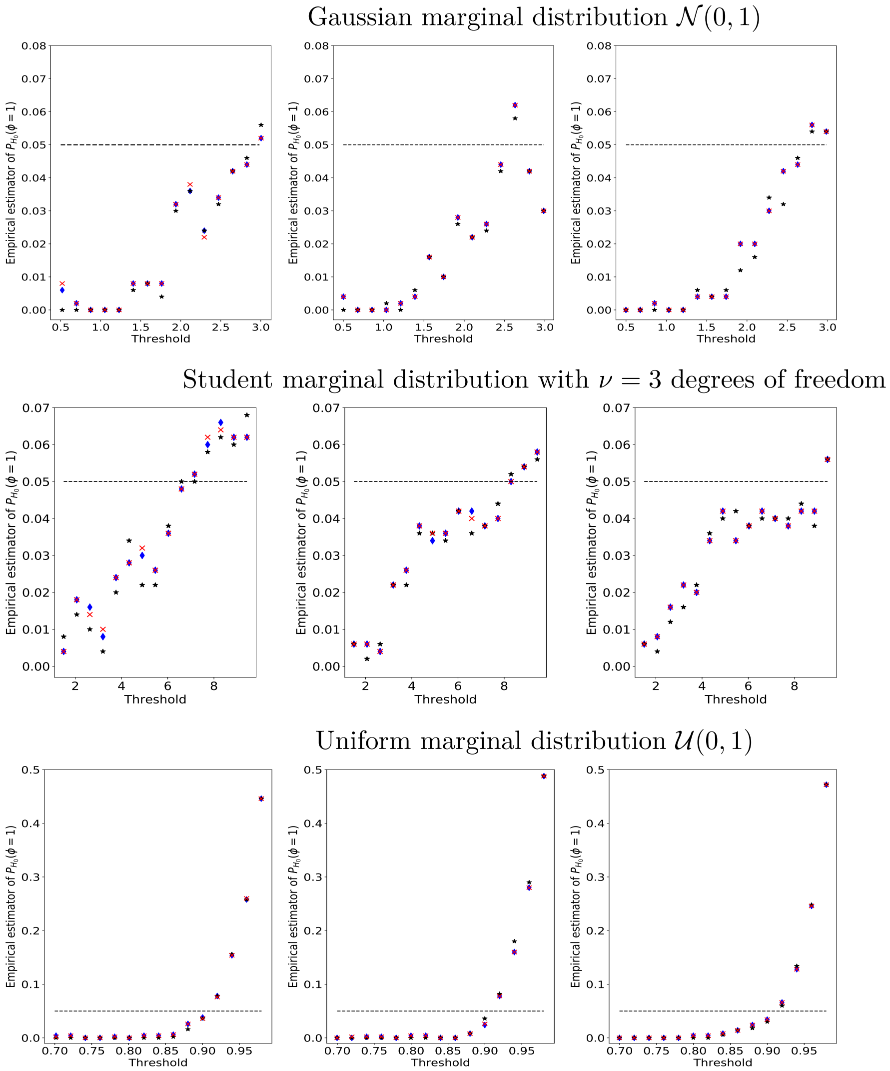

Gaussian marginal distribution $\mathcal{N}(0,1)$

Student marginal distribution with $\nu = 3$ degrees of freedom

Uniform marginal distribution $\mathcal{U}(0,1)$

Figure 2.4 – Under H_0 hypothesis. Average of the empirical values of $\mathbb{P}_{H_0(t)}(\phi_m^{\mathcal{P}} = 1)$ for different thresholds t, for 500 Montecarlo simulations and for $m = 100$ (left panels), 512 (center panels) and 1024 (right panels). We consider Gaussian marginal distribution $\mathcal{N}(0,1)$ (first row), Student marginal distribution with $\nu = 3$ degrees of freedom (second row), Uniform marginal distribution $\mathcal{U}(0,1)$ (third row) and three different test statistics: $\phi_m^{\mathcal{P}}(\hat{\sigma}^{\mathcal{P}})$ as in (2.12) (blue diamonds), $\phi_m^{\mathcal{P}}(\hat{\sigma}^{\mathcal{A}})$ as in (2.13) (red crosses) and $\phi_m^{\text{k-s}}(\hat{\sigma}^{\text{k-s}})$ as in (2.15) (black stars). Threshold $\alpha = 0.05$ is displayed by a dashed horizontal line.

median to characterize the symmetry of a distribution [*i.e.* a random variable X is symmetrically distributed around θ, the center of symmetry, if its distribution function F satisfies $F(\theta - x) = 1 - F(\theta + x)$], although, we decided to use the median estimator for θ in the alternative hypothesis. As we can appreciate in Figure 2.4, the test is able to successfully accept the H_0 hypothesis. However, the choice of the threshold is crucial in regard of the quality of the test. Unsurprisingly, for extreme thresholds, the test is less precise. We will focus on this important point in Section 2.6 below. Notice that the performances of our test statistic $\phi_m^{\mathcal{P}}$ with the two proposed estimators of the variance $\hat{\sigma}^{\mathcal{A}}$ and $\hat{\sigma}^{\mathcal{P}}$ (in red crosses and blue diamonds, respectively) seem to be globally similar. Furthermore, these satisfactory results are comparable to those obtained with the Kolmogorov-Smirnov based estimator in (2.15) (black stars).

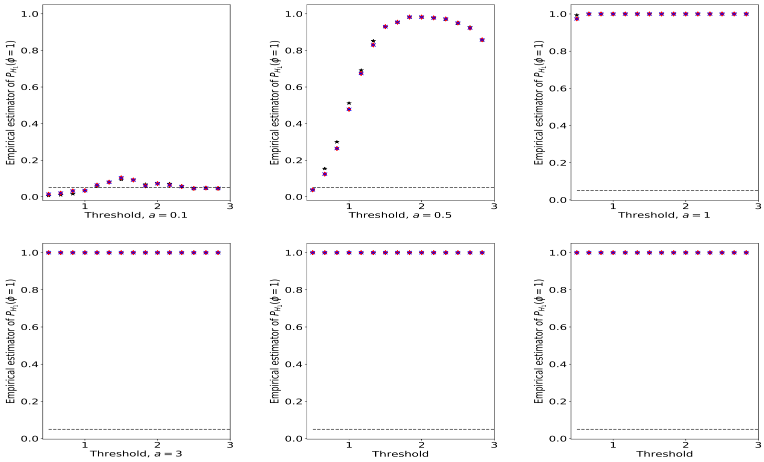
Skew-normal, Exponential and Chi-squared marginal distributions

Figure 2.5 – Under H_1 hypothesis. Average of the empirical values of $\mathbb{P}_{H_1(t)}(\phi_m^{\mathcal{P}} = 1)$ for different thresholds t, for 500 Montecarlo simulations for $m = 512$ with a skew-normal marginal distribution centered around its median value, with different choices of parameter $a = 0.1, 0.5, 1, 3$ (from first to fourth panel), Exp$(1) - \theta$ distribution (fifth panel) and $\chi^2 - \theta$ distribution of degree of freedom 1 (sixth panel), θ been the median value of the image. We consider different test statistics: $\phi_m^{\mathcal{P}}(\hat{\sigma}^{\mathcal{P}})$ as in (2.12) (blue crosses), $\phi_m^{\mathcal{P}}(\hat{\sigma}^{\mathcal{A}})$ as in (2.13) (red diamonds) and $\phi_m^{\text{k-s}}(\hat{\sigma}^{\text{k-s}})$ as in (2.15) (black stars). Threshold $\alpha = 0.05$ is displayed by a dashed horizontal line.

Figure 2.5 numerically describes the good performance of our test $\phi_m^{\mathcal{P}}$ to distinguish $H_1(t)$ from $H_0(t)$, for $t \in \mathbb{R}_+^\star$, to test the alternative hypothesis, we choose to consider the median estimator to compute the value of θ. We focus our study on three asymmetric distributional cases: Skew-normal distribution with probability density function given by $f(x) = 2\phi(x)\Phi(ax)$, for $x \in \mathbb{R}$, with $a \geq 0$, $\phi(\cdot)$ (*resp.* $\Phi(\cdot)$) the standard normal probability density function (*resp.* standard normal cumulative distribution function), Exponential distribution with parameter 1 and χ^2 distribution with degree of freedom 1. Unsurprising, in the skew-normal case, we observe that when a is larger the power of the test increases, indeed the smaller the parameter a, the less asymmetric the distribution will be. This behavior can be easily observed for the four chosen levels of skewness parameter $a = 0.1, 0.5, 1, 3$ in Figure 2.5 (from first to fourth panel).

INVESTIGATION OF THE RATIO BEHAVIOR IN THE SPATIALLY DEPENDENT FRAMEWORK In this section, we aim to investigate the behavior of the ratios previously constructed using the perimeter and Kolmogrov-Smirnov method in a dependent framework. Let recall some notations

$$R_{m,\theta}(t) = \frac{\check{\mathcal{P}}_m(\theta - t)}{\check{\mathcal{P}}_m(\theta + t)} \quad \text{and} \quad R^{\text{k-s}}_{m,\theta}(t) = \frac{1 - \hat{p}_m^{\mathcal{A}}(\theta - t)}{\hat{p}_m^{\mathcal{A}}(\theta + t)},$$

with $\check{\mathcal{P}}_m(\cdot)$ as in Definition 2.2.1 and $\hat{p}_m^{\mathcal{A}}(\cdot)$ as in Definition 2.3.4.

In Figures 2.6 and 2.7 we evaluate for 500 Montecarlo simulations the average of the absolute error between the estimated ratio $R_{m,\theta}(t)$ and $R^{\text{k-s}}_{m,\theta}(t)$ and the targeted value 1, *i.e.*,

$$\widehat{\mathbb{E}}[|R_{m,\theta}(t)-1|] \quad \text{and} \quad \widehat{\mathbb{E}}[|R^{\text{k-s}}_{m,\theta}(t)-1|].$$

In Figure 2.6 we consider a smooth Gaussian random field X of zero mean and unit variance of covariance structure given by $\rho(x) = \exp\left(-\kappa ||x||_2^2\right)$ (under H_0 hypothesis), in Figure 2.7 a chi-squared field with degree of freedom given by X^2 (under H_1 hypothesis, see for instance Section 2.2.2 in Biermé et al. (2019)).

We can observe in these numerical studies, that the ratio constructed by using $R_{m,\theta}(t)$ performs slightly better than the one with $R^{\text{k-s}}_{m,\theta}$ in a dependent framework (for a small spatial dependence parameter κ, see right panels in Figures 2.6 and 2.7). This can be motivated by the fact that, in the considered dependent framework, the perimeter is a natural suitable candidate to get information about the underlying spatial structure and take into account the interconnection between the pixels.

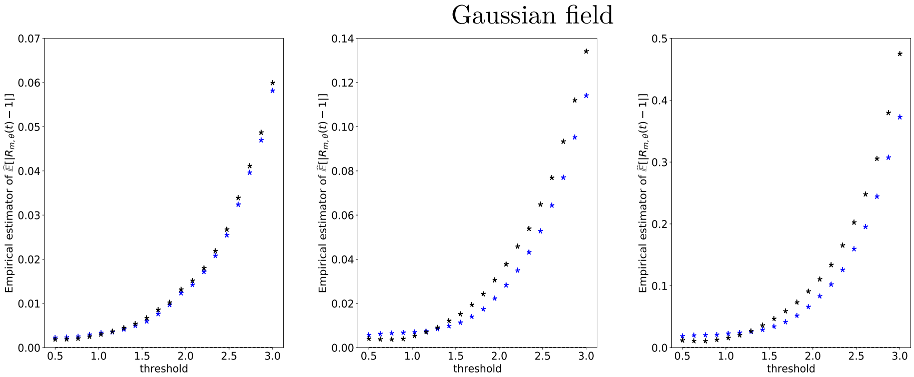

Figure 2.6 – Under H_0 hypothesis. $\widehat{\mathbb{E}}[|R_{m,\theta}(t)-1|]$ (blue stars) and $\widehat{\mathbb{E}}[|R^{\text{k-s}}_{m,\theta}(t)-1|]$ (black stars), for different thresholds t, for 500 Montecarlo simulations and $m = 512$. We consider a smooth stationnary Gaussian random field of covariance structure given by $\rho(x) = \exp\left(-\kappa ||x||_2^2\right)$, $x \in \mathbb{R}^2$ for different values of κ: 1 (left panel), 0.1 (center panel) and 0.01 (right panel).

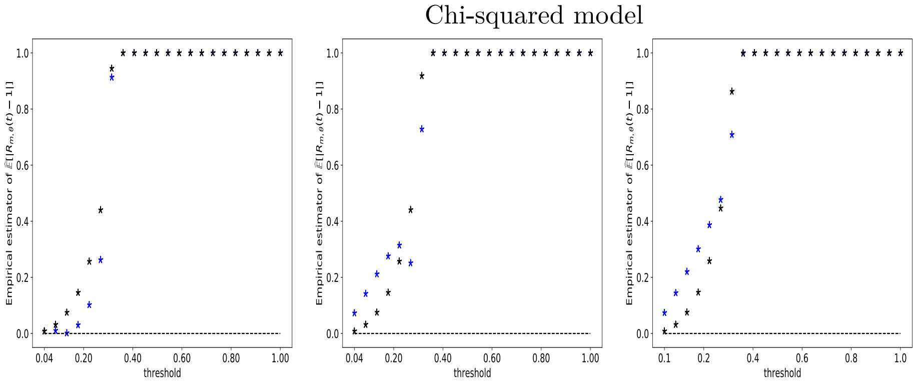

Figure 2.7 – Under H_1 hypothesis. $\widehat{\mathbb{E}}[|R_{m,\theta}(t)-1|]$ (blue stars) and $\widehat{\mathbb{E}}[|R^{\text{k-s}}_{m,\theta}(t)-1|]$ (black stars), for different thresholds t, for 500 Montecarlo simulations and $m = 512$. We consider a chi-square field with 1 degree of freedom, i.e., $\frac{1}{\sqrt{2}}X(t)^2 - \theta$, with X a centered with unit variance smooth stationnary Gaussian random field of covariance structure given by $\rho(x) = \exp\left(-\kappa||x||_2^2\right)$, $x \in \mathbb{R}^2$ and θ the median value of $\frac{1}{\sqrt{2}}X(t)^2$, represented for different values of κ: 1 (left panel), 0.1 (center panel) and 0.01 (right panel).

Here we investigate the behavior of the empirical ratios and not of the associated test statistics to reduce the bias induced by the empirical estimation of unknown variances. These numerical investigations allow us to conjecture that, in a dependent framework, the geometrical feature of the perimeter contains important information about the field.

2.6 Perimeter based symmetry test for large threshold and dense tiling

Following the considerations in Section 2.5, we aim to improve the quality of the proposed test for large thresholds. As in Dalmao et al. (2017), we firstly study the convergence of the ratio between the first two moments of the unscaled perimeter $\mathcal{P}_m$ (see Equations (2.3) and (2.4)). In Lemma 2.6.1 below, the expectation and the variance are proven to have the same order of magnitude for large threshold and dense tiling.

Lemma 2.6.1 (First two moments ratio for large threshold)**.** *Let $\mathcal{P}_m(t)$ as in* (2.1) *and $\mu_{\mathcal{P}}(p_t, m)$ and $\sigma^2_{\mathcal{P}}(p_t, m)$ the associated mean and variance. Let (t_m) be a sequence of positive real numbers such that $p_{t_m} \to 0$ as $m \to \infty$, then,*

$$\frac{\sigma^2_{\mathcal{P}}(p_{t_m}, m)}{\mu_{\mathcal{P}}(p_{t_m}, m)} \xrightarrow[m\to\infty]{} 4,$$

and furthermore, for m large enough,

$$0.5 \;\leq\; \frac{\sigma^2_{\mathcal{P}}(p_{t_m}, m)}{\mu_{\mathcal{P}}(p_{t_m}, m)} \;\leq\; 4.$$

The proof of Lemma 2.6.1 is postponed to Section 2.7. By using Lemma 2.6.1 we can now formulate a bivariate Central Limit Theorem for our geometrical feature for $m \to \infty$ and large thresholds.

Proposition 2.6.2 (Bivariate Central Limit Theorem for large threshold and dense tiling)**.** *Let* $0 < \gamma < 2$ *and* $t_{(m,\gamma)}$ *and* $s_{(m,\gamma)}$ *two points of continuity for the cumulative distribution function* F*, such that*

$$t_{(m,\gamma)} := F^{-1}(\tfrac{1}{m^\gamma}) \quad \textit{and} \quad s_{(m,\gamma)} := F^{-1}(1 - \tfrac{1}{m^\gamma}).$$

Then, it holds that

$$\sqrt{\frac{m^2 \mathbb{E}(\check{\mathcal{P}}_m(t_{(m,\gamma)}))}{4}} \left(\begin{pmatrix} \dfrac{\check{\mathcal{P}}_m(t_{(m,\gamma)})}{\mathbb{E}(\check{\mathcal{P}}_m(t_{(m,\gamma)}))} \\ \dfrac{\check{\mathcal{P}}_m(s_{(m,\gamma)})}{\mathbb{E}(\check{\mathcal{P}}_m(s_{(m,\gamma)}))} \end{pmatrix} - \begin{pmatrix} 1 \\ 1 \end{pmatrix} \right) \xrightarrow[m\to\infty]{d} \mathcal{N}\left(\begin{pmatrix} 0 \\ 0 \end{pmatrix}, \begin{pmatrix} 1 & 0 \\ 0 & 1 \end{pmatrix} \right). \tag{2.16}$$

The proof of Proposition 2.6.2 is postponed to Section 2.7. Note that we have written $\mathbb{E}\left(\check{\mathcal{P}}_m(t_{(m,\gamma)})\right)$ and $\mathbb{E}\left(\check{\mathcal{P}}_m(s_{(m,\gamma)})\right)$ in (2.16) for visual symmetry purposes although those two quantities are equal (see Equation (2.3)). Finally, we can easily derive the following result.

Corollary 2.6.3. *Under assumptions of Proposition 2.6.2, it holds that*

$$\sqrt{\frac{m^2 \mathbb{E}(\check{\mathcal{P}}(t_{(m,\gamma)}))}{8}} \left(\frac{\check{\mathcal{P}}(t_{(m,\gamma)})}{\check{\mathcal{P}}(s_{(m,\gamma)})} - 1 \right) \xrightarrow[m\to\infty]{d} \mathcal{N}(0,1). \tag{2.17}$$

Furthermore,

$$\sqrt{\frac{m^2 \check{\mathcal{P}}_m(t_{(m,\gamma)})}{8}} \left(\frac{\check{\mathcal{P}}(t_{(m,\gamma)})}{\check{\mathcal{P}}(s_{(m,\gamma)})} - 1 \right) \xrightarrow[m\to\infty]{d} \mathcal{N}(0,1). \tag{2.18}$$

Equation (2.17) is obtained via the Delta method applied to Proposition 2.6.2. Finally, Equation (2.18) is given by using that, for $m \to \infty$, $\check{\mathcal{P}}_m(t_{(m,\gamma)})/\mathbb{E}(\check{\mathcal{P}}_m(t_{(m,\gamma)})) \xrightarrow{\mathbb{P}} 1$ and by applying the Slutsky Theorem.

Using Corollary 2.6.3, one can build a modified version of the empirical accessible test statistic $\phi_m^{\mathcal{P}}$ in (2.9) with asymptotic level α, adapted to large thresholds. Under $H_0(t)$ hypothesis, let θ be the median value of the distribution and $u_{(m,\gamma)} \in \mathbb{R}_+^\star$ so that $\theta + u_{(m,\gamma)} := F^{-1}(1 - \frac{1}{m^\gamma})$, and $\theta - u_{(m,\gamma)} := F^{-1}(\frac{1}{m^\gamma})$. Coming back to the ratio $R_{m,\theta}$ introduced in Section 2.4, we have

$$R_{m,\theta}(u_{(m,\gamma)}) := \frac{\check{\mathcal{P}}_m(\theta - u_{(m,\gamma)})}{\check{\mathcal{P}}_m(\theta + u_{(m,\gamma)})}.$$

Then, from Corollary 2.6.3, it holds that

$$\hat{v}_{(m,\gamma)}(R_{m,\theta}(u_{(m,\gamma)}) - 1) \xrightarrow[m\to\infty]{d,H_0} \mathcal{N}(0,1) \quad \text{with} \quad \hat{v}_{(m,\gamma)} = \sqrt{\frac{m^2 \check{\mathcal{P}}(\theta - u_{(m,\gamma)})}{8}}.$$

This asymptotic allows us to define a new symmetry test statistic by prescribing

$$\phi_m^{\mathcal{P}}(\hat{v}_{(m,\gamma)}) = \mathbb{1}_{\left\{\hat{v}_{(m,\gamma)}|R_{m,\theta}(u_{(m,\gamma)})-1| \geq q_{1-\alpha/2}\right\}}. \tag{2.19}$$

Conversely to Equation (2.9), the main statistical interest of the test in (2.19) is to avoid the estimation of the variance. Furthermore, as one can remark for instance in the numerical study in Figure 2.8, global performances of the test in (2.19) are similar to those obtained in the same distributional framework in Figure 2.4. This means that we can obtain similar $p-$values with less effort in terms of moment estimations. Furthermore, notice that, since $\gamma = \frac{-\ln(p_{u_{m,\gamma}})}{\ln(m)}$ and $\gamma \in (0, 2)$, the range of admissible values for $u_{m,\gamma}$ from Proposition 2.6.2 is growing with m.

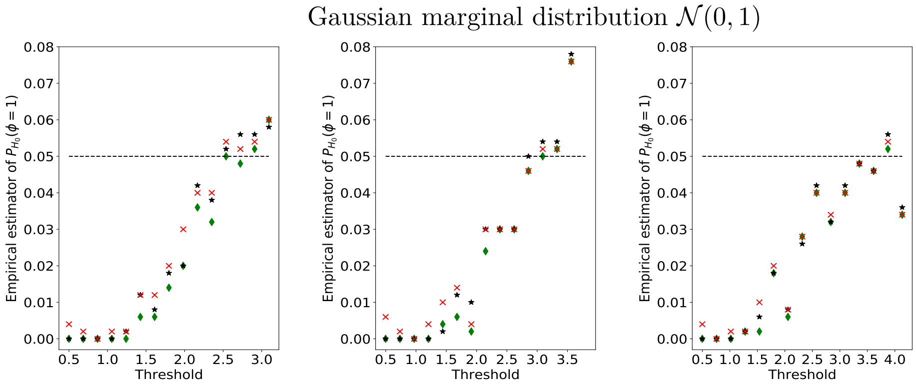

Figure 2.8 – Under H_0 hypothesis. Average of the empirical values of $\mathbb{P}_{H_0(t)}(\phi_m^{\mathcal{P}} = 1)$ for different thresholds $t_{m,\gamma}$, for 500 Montecarlo simulations, for $m = 100$ (left panels), 512 (center panels) and 1024 (right panels). We consider a Gaussian marginal distribution $\mathcal{N}(0, 1)$ and different test statistics: $\phi_m^{\mathcal{P}}(\hat{\sigma}^{\mathcal{A}})$ as in (2.13) (red stars), $\phi_m^{\text{k-s}}(\hat{\sigma}^{\text{k-s}})$ as in (2.15) (black stars) and $\phi_m^{\mathcal{P}}(\hat{v}_{(m,\gamma)})$ as in (2.19) (green diamonds). Threshold $\alpha = 0.05$ is displayed by a dashed horizontal line.

In order to better appreciate the statistical equivalent performance of the four proposed test statistics, we gathered in Table 2.1 averaged values of the empirical $\mathbb{P}_{H_0(t)}(\phi_m^{\mathcal{P}} = 1)$ and associated standard deviations for different thresholds and several distributional models. We underline in bold some values for which the last proposed test in (2.19) seems slightly outperform the other ones especially for large threshold values (see Table 2.1).

Gaussian marginal distribution $\mathcal{N}(0,1)$

Thresholds $t_{m,\gamma}$	1.0	1.85	2.69	3.54
$\mathbb{P}_{H_0}(\phi_m^{\mathcal{P}}(\hat{\sigma}^{\mathcal{P}})=1)$	0.0 (0.0)	0.018 (0.133)	0.048 (0.214)	0.040 (0.196)
$\mathbb{P}_{H_0}(\phi_m^{\mathcal{A}}(\hat{\sigma}^{\mathcal{A}})=1)$	0.0 (0.0)	0.018 (0.133)	0.048 (0.214)	0.038 (0.191)
$\mathbb{P}_{H_0}(\phi_m^{\text{k-s}}(\hat{\sigma}^{\text{k-s}})=1)$	0.0 (0.0)	0.018 (0.133)	0.050 (0.218)	0.040 (0.196)
$\mathbb{P}_{H_0}(\phi_m^{\mathcal{P}}(\hat{v})=1)$	0.0 (0.0)	**0.016 (0.125)**	0.048 (0.214)	0.038 (0.191)

Student marginal distribution $df=3$

Thresholds $t_{m,\gamma}$	1.5	3.62	5.75	7.87
$\mathbb{P}_{H_0}(\phi_m^{\mathcal{P}}(\hat{\sigma}^{\mathcal{P}})=1)$	0.006 (0.077)	0.01 (0.099)	0.034 (0.181)	0.038 (0.191)
$\mathbb{P}_{H_0}(\phi_m^{\mathcal{A}}(\hat{\sigma}^{\mathcal{A}})=1)$	0.006 (0.077)	0.01 (0.099)	0.034 (0.181)	0.038 (0.191)
$\mathbb{P}_{H_0}(\phi_m^{\text{k-s}}(\hat{\sigma}^{\text{k-s}})=1)$	0.002 (0.045)	0.01 (0.099)	0.032 (0.176)	0.038 (0.191)
$\mathbb{P}_{H_0}(\phi_m^{\mathcal{P}}(\hat{v})=1)$	**0.0 (0.0)**	0.01 (0.099)	0.032 (0.176)	0.038 (0.191)

Uniform marginal distribution $\mathcal{U}(0,1)$

Thresholds $t_{m,\gamma}$	0.7	0.78	0.85	0.93
$\mathbb{P}_{H_0}(\phi_m^{\mathcal{P}}(\hat{\sigma}^{\mathcal{P}})=1)$	0.002 (0.045)	0.0 (0.0)	0.004 (0.063)	0.094 (0.292)
$\mathbb{P}_{H_0}(\phi_m^{\mathcal{A}}(\hat{\sigma}^{\mathcal{A}})=1)$	0.002 (0.045)	0.0 (0.0)	0.004 (0.063)	0.094 (0.292)
$\mathbb{P}_{H_0}(\phi_m^{\text{k-s}}(\hat{\sigma}^{\text{k-s}})=1)$	0.0 (0.0)	0.0 (0.0)	0.004 (0.063)	0.096 (0.295)
$\mathbb{P}_{H_0}(\phi_m^{\mathcal{P}}(\hat{v})=1)$	0.0 (0.0)	0.0 (0.0)	0.0 (0.0)	**0.064 (0.245)**

Table 2.1 – Under H_0 hypothesis. Average of the empirical values of $\mathbb{P}_{H_0(t)}(\phi_m^{\mathcal{P}}=1)$ and associated standard deviations for different thresholds $t_{m,\gamma}$, for 500 Montecarlo simulations, for $m=1024$. We consider different test statistics: $\phi_m^{\mathcal{P}}(\hat{\sigma}^{\mathcal{P}})$ as in (2.12), $\phi_m^{\mathcal{P}}(\hat{\sigma}^{\mathcal{A}})$ as in (2.13), $\phi_m^{\text{k-s}}(\hat{\sigma}^{\text{k-s}})$ as in (2.15) and finally $\phi_m^{\mathcal{P}}(\hat{v}_{(m,\gamma)})$ as in (2.19).

2.7 Proofs

Proof of Proposition 2.3.1. One can start by observing that both $f_1^{(t)}(l,k)$ and $f_2^{(t)}(k,l)$ follow a Bernoulli distribution with parameter $2p_t(1-p_t)$. Thus, using Equation (2.1), one can write

$$\begin{aligned}\mathbb{E}(\mathcal{P}_m(t)) = \mathbb{E}(\mathcal{P}_m^{(1)}(t)+\mathcal{P}_m^{(2)}(t)) &= 2\sum_{l=1}^{m}\sum_{k=2}^{m}\mathbb{E}(f_1^{(t)}(l,k)) \\ &= 4m(m-1)p_t(1-p_t).\end{aligned}$$

Thus we obtain the result for $\mathbb{E}\left(\check{\mathcal{P}}_m\right)$ dividing by m^2. $\square$

Proof of Proposition 2.3.2. Without loss of generality, one can assume that $t \leq s$. We use here Definition 2.1 of the perimeter. Let us start by making use of the fact that $(\mathcal{P}_m^{(1)}(s),\mathcal{P}_m^{(1)}(t)) \overset{d}{=} (\mathcal{P}_m^{(2)}(s),\mathcal{P}_m^{(2)}(t))$. Thus,

$$\text{Cov}\left(\mathcal{P}_m(s),\mathcal{P}_m(t)\right) \quad = \quad 2\text{Cov}\left(\mathcal{P}_m^{(1)}(s),\mathcal{P}_m^{(1)}(t)\right) + 2\text{Cov}\left(\mathcal{P}_m^{(2)}(s),\mathcal{P}_m^{(1)}(t)\right).$$

Firstly,

$$\begin{aligned}\operatorname{Cov}\left(\mathcal{P}_m^{(1)}(s), \mathcal{P}_m^{(1)}(t)\right) &= \operatorname{Cov}\left(\sum_{l=1}^{m}\sum_{k=2}^{m} f_1^{(s)}(l,k), \sum_{i=1}^{m}\sum_{j=2}^{m} f_1^{(t)}(i,j)\right)\\ &= \sum_{l=1}^{m}\sum_{k=2}^{m}\sum_{j=2}^{m} \operatorname{Cov}\left(f_1^{(s)}(l,k), f_1^{(t)}(i,j)\right),\end{aligned}$$

where we have used that for $\forall k, l,$ if $, i \neq l,$ $\operatorname{Cov}\left(f_1^{(s)}(l,k),\ f_1^{(t)}(i,j)\right) = 0$.

In the above sum, there will be only three cases for which the covariance function is different from 0: $j = k, j = k+1$ and $j = k-1$.

1. If $j = k$,

$$\begin{aligned}\mathbb{E}(f_1^{(s)}(l,k) f_1^{(t)}(l,k)) &= \mathbb{P}\left(f_1^{(s)}(l,k) = 1 \ \cap\ f_1^{(t)}(l,k) = 1\right)\\ &= \mathbb{P}\big(((X_{l,k-1} < s \ \cap\ X_{l,k} \geq s) \ \cup\ (X_{l,k-1} \geq s \ \cap\ X_{l,k} < s))\\ &\quad \cap\ ((X_{l,k-1} < t \ \cap\ X_{l,k} \geq t) \ \cup\ (X_{l,k-1} \geq t \ \cap\ X_{l,k} < t))\big)\\ &= \mathbb{P}\Bigg(\big(X_{l,k-1} < s \ \cap\ X_{l,k} \geq s \ \cap\ X_{l,k-1} < t \ \cap\ X_{l,k} \geq t\big)\\ &\quad \cup\ \big(X_{l,k-1} < s \ \cap\ \underbrace{X_{l,k} \geq s \ \cap\ X_{l,k} < t}_{=\emptyset} \cap X_{l,k-1} \geq t\big)\\ &\quad \cup\ \big(\underbrace{X_{l,k-1} \geq s \ \cap\ X_{l,k-1} < t}_{=\emptyset} \cap X_{l,k} < s \ \cap\ X_{l,k} \geq t\big)\\ &\quad \cup\ (X_{l,k-1} \geq s \ \cap\ X_{l,k} < s \ \cap\ X_{l,k-1} \geq t \ \cap\ X_{l,k} < t)\Bigg)\\ &= \mathbb{P}\big(X_{l,k-1} < t \ \cap\ X_{l,k} \geq s\big) + \mathbb{P}\big(X_{l,k-1} \geq s \ \cap\ X_{l,k} < t\big)\\ &= p_s(1-p_t) + (1-p_t)p_s\\ &= 2p_s(1-p_t).\end{aligned}$$

Thus,

$$\begin{aligned}\operatorname{Cov}\left(f_1^{(s)}(l,k), f_1^{(t)}(l,k)\right) &= 2p_s(1-p_t) - 2p_s(1-p_s)2p_t(1-p_t)\\ &= 2p_s(1-p_t)(1-2p_t+2p_tp_s).\end{aligned}$$

2. If $j = k+1$,

$$\begin{aligned}\mathbb{E}(f_1^{(s)}(l,k) f_1^{(t)}(l,k+1)) &= \mathbb{P}\big(f_1^{(s)}(l,k) = 1 \ \cap\ f_1^{(t)}(l,k+1) = 1\big)\\ &= \mathbb{P}\big(((X_{l,k-1} < s \ \cap\ X_{l,k} \geq s) \ \cup\ (X_{l,k-1} \geq s \ \cap\ X_{l,k} < s))\\ &\quad \cap\ ((X_{l,k} < t \ \cap\ X_{l,k+1} \geq t) \ \cup\ (X_{l,k} \geq t \ \cap\ X_{l,k+1} < t)))\\ &= \mathbb{P}\big((X_{l,k-1} < s \ \cap\ \underbrace{X_{l,k} \geq s \ \cap\ X_{l,k} < t}_{=\emptyset} \cap X_{l,k+1} \geq t)\\ &\quad \cup\ (X_{l,k-1} < s \ \cap\ X_{l,k} \geq s \ \cap\ X_{l,k} \geq t \ \cap\ X_{l,k+1} < t)\\ &\quad \cup\ (X_{l,k-1} \geq s \ \cap\ X_{l,k} < s \ \cap\ X_{l,k} < t \ \cap X_{l,k+1} \geq t)\end{aligned}$$

$$
\begin{aligned}
&\quad \cup\ (X_{l,k-1} \geq s\ \cap\ X_{l,k} < s\ \cap\ X_{l,k} \geq t\ \cap\ X_{l,k+1} < t)\big)\\
&= \mathbb{P}(X_{l,k-1} < s)\mathbb{P}(X_{l,k} \geq s)\mathbb{P}(X_{l,k+1} < t)\\
&\quad +\ \mathbb{P}(X_{l,k-1} \geq s)\mathbb{P}(X_{l,k} < t)\mathbb{P}(X_{l,k+1} \geq t)\\
&\quad +\ \mathbb{P}(X_{l,k-1} \geq s)\mathbb{P}(X_{l,k} \geq t\ \cap\ X_{l,k} < s)\mathbb{P}(X_{l,k+1} < t)\\
&= (1-p_s)p_s(1-p_t) + (1-p_t)p_t p_s + p_s(p_t - p_s)(1-p_t)\\
&= p_s(1-p_t)(1+2p_t-2p_s).
\end{aligned}
$$

Thus,

$$
\begin{aligned}
\operatorname{Cov}\left(f_1^{(s)}(l,k), f_1^{(t)}(l,k+1)\right) &= p_s(1-p_t)(1+2p_t-2p_s) - 2p_s(1-p_s)2p_s(1-p_t)\\
&= p_s(1-p_t)(1-2p_t-2p_s+4p_t p_s).
\end{aligned}
$$

3. Similarly, if $j = k-1$,

$$
\begin{aligned}
\operatorname{Cov}(f_1^{(s)}(l,k), f_1^{(t)}(l,k-1)) &= \operatorname{Cov}(f_1^{(s)}(l,k), f_1^{(t)}(l,k+1))\\
&= p_s(1-p_t)(1-2p_t-2p_s+4p_t p_s).
\end{aligned}
$$

Thus,

$$
\begin{aligned}
\operatorname{Cov}\big(\mathcal{P}_m^{(1)}(s), \mathcal{P}_m^{(1)}(t)\big) &= \sum_{l=1}^{m}\sum_{k=2}^{m} \operatorname{Cov}\left(f_1^{(s)}(l,k), f_1^{(t)}(l,k)\right)\\
&\quad + \sum_{l=1}^{m}\sum_{k=3}^{m} \operatorname{Cov}\left(f_1^{(s)}(l,k), f_1^{(t)}(l,k+1)\right)\\
&\quad + \sum_{l=1}^{m}\sum_{k=3}^{m} \operatorname{Cov}\left(f_1^{(s)}(l,k), f_1^{(t)}(l,k-1)\right)\\
&= 2m(m-1)p_s(1-p_t)(1-2p_t(1-p_s))\\
&\quad +\ 2m(m-2)p_s(1-p_t)(1+2p_t-2p_s-4p_t(1-p_s)).
\end{aligned}
$$

Now, let us compute the inter-level covariance between the horizontal contributions to the perimeter and the vertical ones:

$$
\begin{aligned}
\operatorname{Cov}\left(\mathcal{P}_m^{(1)}(s), \mathcal{P}_m^{(2)}(t)\right) &= \operatorname{Cov}\left(\sum_{l=1}^{m}\sum_{k=2}^{m} f_1^{(s)}(l,k), \sum_{i=1}^{m}\sum_{j=2}^{m} f_2^{(t)}(j,i)\right)\\
&= \sum_{l=1}^{m}\sum_{k=2}^{m}\sum_{i=1}^{m}\sum_{j=2}^{m} \operatorname{Cov}\left(f_1^{(s)}(l,k), f_2^{(t)}(j,i)\right).
\end{aligned}
$$

To this aim, notice that the covariance between cells is non equal to zero only if the cells are neighbors, that implies that

$$
\text{for } i \notin \{k-1,k\} \text{ or for } l \notin \{j-1,j\}\ \operatorname{Cov}(f_1(l,k), f_2(j,i)) =\ 0.
$$

Thus,

$$\begin{aligned}\mathrm{Cov}(\mathcal{P}_m^1(s),\mathcal{P}_m^2(t)) = \sum_{k=2}^{m}\sum_{j=2}^{m}\Big(&\mathrm{Cov}(f_1^{(s)}(j-1,k),f_2^{(t)}(j,k-1))\\ &+\ \mathrm{Cov}(f_1^{(s)}(j,k),f_2^{(t)}(j,k-1))\\ &+\ \mathrm{Cov}(f_1^{(s)}(j-1,k),f_2^{(t)}(j-1,k))\\ &+\ \mathrm{Cov}(f_1^{(s)}(j,k),f_2^{(t)}(j,k))\Big).\end{aligned}$$

Due to the *i.i.d* setting (see Figure 2.9), one can remark that the four types of covariance in the above sum are equal and are equal to $\mathrm{Cov}(f_1^{(s)}(l,k),f_2^{(t)}(l,k+1))$.

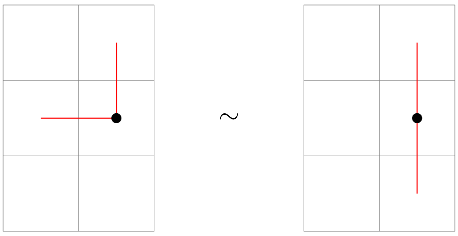

Figure 2.9 – Representation of the configuration between $(f_1(l,k),f_2(l+1,k-1))$ (left panel) and $(f_1(l,k),f_1(l,k+1))$ (right panel), the black dot represents the cell (k,l).

Thus,

$$\begin{aligned}\mathrm{Cov}(\mathcal{P}_m^1(s),\mathcal{P}_m^2(t)) &= 4(m-1)^2\mathrm{Cov}(f_1^{(s)}(l,k),f_2^{(t)}(l,k+1))\\ &= 4(m-1)^2p_s(1-p_t)(1+2p_t-2p_s-4p_t(1-p_s)).\end{aligned}$$

Putting all elements together, we get the covariance function of the unscaled perimeter:

$$\begin{aligned}\mathrm{Cov}\left(\mathcal{P}_m(s),\mathcal{P}_m(t)\right) = 4\,p_s(1-p_t)((4m^2-7m+2)\\ -2p_t(1-p_s)(7m^2-13m+4)+2(p_t-p_s)(3m^2-6m+2)).\end{aligned}$$

Hence, the result. ☐

Proof of Theorem 2.3.3. In order to prove this result, we will use the well known Cramèr-Wold method. For the sake of completeness we recall it below.

Theorem 2.7.1 (Cramèr-Wold method, see, *e.g.*, Billingsley (1995), p. 383)**.** *Let* $\overline{X}^m = (X_1^m,\cdots,X_r^m)$ *and* $\overline{X} = (X_1,\cdots,X_r)$ *be random vectors of dimension* $r\geq 1$*. Then,* $\overline{X}^m$ *converges in distribution to* $\overline{X}$ *if and only if*

$$\textstyle\sum_{i=1}^r a_iX_i^m \xrightarrow[m\to+\infty]{d} \sum_{i=1}^r a_iX_i,$$

for each $(a_1,\cdots,a_r)\in\mathbb{R}^r$*, i.e., if every fixed linear combination of the coordinates of* $\overline{X}^m$ *converges in distribution to the correspondent linear combination of coordinates of* $\overline{X}$*.*

We first need to introduce some notations. Let $V_m = \{1,\ldots,m\}\times\{2,\ldots,m\}$ $a_1,\ldots,a_r\in\mathbb{R}$, $t_1,\ldots,t_r\in\mathbb{R}$, $(l,k)\in V_m$ and $i\in\{1,\ldots,r\}$. Let $\mathcal{P}_m(t_i)$ as in Equation

(2.1). We introduce

$$\begin{aligned} Y_{l,k}(t_i) = {} & \mathbb{1}_{(Z^{(t_i)}_{l,k-1}= 0 \,\cap\, Z^{(t_i)}_{l,k}= 1) \,\cup\, (Z^{(t_i)}_{l,k-1}= 1 \,\cap\, Z^{(t_i)}_{l,k}= 0)} \\ & + \mathbb{1}_{(Z^{(t_i)}_{k-1,l}= 0 \,\cap\, Z^{(t_i)}_{k,l}= 1) \,\cup\, (Z^{(t_i)}_{k-1,l}= 1 \,\cap\, Z^{(t_i)}_{k,l}= 0)}. \end{aligned}$$

Note that $0 \leq Y_{l,k}(t_i) \leq 2$ *a.s.* and $|Y_{l,k}(t_i) - \mathbb{E}(Y_{l,k}(t_i))| \leq 2$, thus $|\sum_{i=1}^r a_i(Y_{k,l}(t_i) - \mathbb{E}(Y_{l,k}(t_i)))| \leq 2\sum_{i=1}^r |a_i|$. We note

$$W^m_{l,k} = \frac{1}{m}\sum_{i=1}^{r} a_i\big[Y_{l,k}(t_i) - \mathbb{E}(Y_{l,k}(t_i)))\big], \tag{2.20}$$

and finally,

$$S_m = \sum_{l=1}^{m}\sum_{k=2}^{m} W^m_{l,k} = \frac{a_1}{m}(\mathcal{P}_m(t_1) - \mathbb{E}(\mathcal{P}_m(t_1))) + \ldots + \frac{a_r}{m}(\mathcal{P}_m(t_r) - \mathbb{E}(\mathcal{P}_m(t_r))).$$

Using the Cramèr-Wold method, we need to prove that

$$S_m \xrightarrow[m\to\infty]{d} \mathcal{N}\left(0,\ \sum_{i=1}^{r} a_i^2\Sigma^\star_r(i,i) + \sum_{0\leq i<j\leq r} 2a_ia_j\Sigma^\star_r(i,j)\right),$$

with $\Sigma^\star_r$ as in ((2.5)). To this purpose we use the following weaker version of Theorem 1 of Heinrich (1986) for bounded variables (see p.200 in Heinrich (1986) for details).

Proposition 2.7.2. *Let* $V_m = \{1,\ldots,m\}\times\{2,\ldots,m\}$ *and* $\{X^m_z, z \in V_m\}$ *be a sequence of* 1*-dependent random field, and* $S_m = \sum_{z\in V_m} X^m_z$*. If the following three conditions are satisfied:*

(i) $\forall\epsilon > 0$, $\sum_{z\in V_m}\mathbb{P}(|X^m_z| \geq \epsilon) \xrightarrow[m\to\infty]{} 0$,

(ii) $\sum_{z\in V_m}\mathbb{E}((X^m_z)^2) \leq C < +\infty$,

(iii) $\mathbb{E}(S_m) \xrightarrow[m\to\infty]{} 0$ *and* $Var(S_m) \xrightarrow[m\to\infty]{} \sigma^2$ *with* $\sigma^2 \in (0,\infty)$,

then, $S_m \xrightarrow[m\to\infty]{d} \mathcal{N}(0,\sigma^2)$.

We start by showing that $\{W^m_z, z \in V_m\}$ satisfies *(i)*. For $\epsilon > 0$, we get that,

$$\begin{aligned} \sum_{(l,k)\in V_m}\mathbb{P}\left(|W^m_{l,k}| \geq \epsilon\right) &\leq \sum_{(l,k)\in V_m}\frac{\mathbb{E}(|W^m_{l,k}|^3)}{\epsilon^3} \\ &\leq \frac{(2\sum_{i=1}^r |a_i|)^3 \times m(m-1)}{(m\epsilon)^3} \xrightarrow[m\to\infty]{} 0. \end{aligned}$$

To prove that $\{W^m_z, z \in V_m\}$ satisfies *(ii)*, we write

$$\sum_{(l,k)\in V_m}\mathbb{E}\left(\left(W^m_{l,k}\right)^2\right) \leq m(m-1)\left(\frac{2}{m}\sum_{i=1}^{r}|a_i|\right)^2 \leq \left(2\sum_{i=1}^{r}|a_i|\right)^2.$$

For *(iii)* we observe that $\mathrm{Var}(S_m) = \mathrm{Var}\left(\frac{a_1}{m}\mathcal{P}_m(t_1) + \ldots + \frac{a_r}{m}\mathcal{P}_m(t_r)\right)$ thus, as $m \to \infty$, $\mathrm{Var}\left(\frac{a_1}{m}\mathcal{P}_m(t_1) + \ldots + \frac{a_r}{m}\mathcal{P}_m(t_r)\right) \to \sum_{i=1}^{r} a_i^2 \Sigma_r^\star(i,i) + \sum_{0 \leq i < j \leq r} 2a_i a_j \Sigma_r^\star(i,j)$, by Equation (2.5). Using the auxiliary Proposition 2.7.2 proves Theorem 2.3.3. ☐

Proof of Proposition 2.3.5. Let θ be the median value of the underlying distribution. We first start with solving the quadratic Equation (2.6) for $m = 2$ under the condition that $t > \theta$ ($i.e$ $p(t) < \frac{1}{2}$). We get that $p(t) = \dfrac{1}{2}\left(1 - \sqrt{1 - 2\mathbb{E}\left(\check{\mathcal{P}}_2(t)\right)}\right)$. Since we are in an *i.i.d.* framework, the variables $\check{\mathcal{P}}_2^i(t)$ for each sub-image S_i are *i.i.d*, and, by using the Law of Large numbers, $\overline{S}_m(t) := \frac{4}{m^2}\sum_i \check{\mathcal{P}}_2^i(t)$ is an estimator of $\mathbb{E}\left(\check{\mathcal{P}}_2(t)\right)$. Applying the Central Limit Theorem, we get

$$\sqrt{\frac{m^2}{4}}\left(\overline{S}_m(t) - \mathbb{E}\left(\check{\mathcal{P}}_2(t)\right)\right) \xrightarrow[m\to\infty]{d}, \mathcal{N}(0, \sigma_{\check{\mathcal{P}}}^2(t,2)), \tag{2.21}$$

with $\sigma_{\check{\mathcal{P}}}^2(t,2) = \mathrm{Var}\left(\check{\mathcal{P}}_2(t)\right) = p_t(1-p_t)\left(1 - 3p_t(1-p_t)\right)$. We apply the Delta method to Equation (2.21) using the function g as defined in Proposition 2.3.4. Note that g is differentiable on $(0, \frac{1}{2})$ and that for $t \neq \frac{1}{2}$, $\mathbb{E}\left(\check{\mathcal{P}}_2(t)\right) < \frac{1}{2}$ Thus

$$\sqrt{\frac{m^2}{4}}\left(g(\overline{S}_m(t)) - g(\mathbb{E}\left(\check{\mathcal{P}}_2(t)\right))\right) \xrightarrow[m\to\infty]{d} g'(\mathbb{E}\left(\check{\mathcal{P}}_2(t)\right)\mathcal{N}(0, \sigma_{\check{\mathcal{P}}}^2(t,2)),$$

with $g'(x) = \dfrac{1}{2\sqrt{1-2x}}$. Since $\sqrt{1 - 2\mathbb{E}\left(\check{\mathcal{P}}_2(t)\right)} = 1 - 2p_t$, we get

$$m\left(\hat{p}_m^{\mathcal{P}}(t) - p(t)\right) \xrightarrow[m\to\infty]{d} \mathcal{N}\left(0, \frac{p(t)(1-p(t))\Big(1 - 3p(t)(1-p(t))\Big)}{4(1-2p(t))^2}\right).$$

Hence, the result for $\hat{p}_m^{\mathcal{P}}$. For $\hat{p}_m^{\mathcal{A}}$, the result is a classical consequence of the Central Limit Theorem. ☐

Proof of Proposition 2.4.1. Let $t, s \in \mathbb{R}$ with $t < s$. Let

$$\mu := \lim_{m\to\infty}\begin{pmatrix}\mu_{\check{\mathcal{P}}_m}(t)\\ \mu_{\check{\mathcal{P}}_m}(s)\end{pmatrix} = \begin{pmatrix}4p_t(1-p_t)\\ 4p_s(1-p_s)\end{pmatrix} \text{ and } g : \begin{pmatrix}x\\ y\end{pmatrix} \mapsto \frac{x}{y}.$$

Applying the Delta method to the multivariate Central Limit Theorem 2.3.3, we get the following result

$$m\left(\frac{\check{\mathcal{P}}_m(t)}{\check{\mathcal{P}}_m(s)} - \frac{\mu_{\check{\mathcal{P}}_m}(t)}{\mu_{\check{\mathcal{P}}_m}(s)}\right) \xrightarrow[m\to\infty]{d} \mathcal{N}\left(0, \nabla g(\mu)^T \Sigma_2^\star \nabla g(\mu)\right),$$

with $\nabla g(\mu) = \begin{pmatrix}\dfrac{1}{4p_s(1-p_s)}\\ \dfrac{-4p_t(1-p_t)}{(4p_s(1-p_s))^2}\end{pmatrix}$, and $\Sigma_2^\star$ as in Theorem 2.3.3. Thus,

$$\nabla g(\mu)^T \Sigma_2^\star \nabla g(\mu) = \frac{p_t(1-p_t)}{(p_s(1-p_s))^3}\Big(p_s(1-p_s) - 2p_s(1-p_t) - 3p_s(p_t - p_s)(1-p_t)$$

$$+\,p_t(1-p_t)\Big).$$

□

Proof of Proposition 2.4.2. From Proposition 2.4.1 it holds that,

$$m\left(R_{m,\theta}(t)-\frac{\mu_{\check{\mathcal{P}}_m}(\theta-t)}{\mu_{\check{\mathcal{P}}_m}(\theta+t)}\right)\xrightarrow[m\to\infty]{d,H_0}\mathcal{N}\left(0,\tilde{\sigma}^2(\theta-t,\theta+t)\right). \tag{2.22}$$

Let us denote $\sigma:=\sigma(\theta+t)=\sqrt{\frac{(2p_{\theta+t}-1)(3p_{\theta+t}-2)}{p_{\theta+t}(1-p_{\theta+t})^2}}$ the standard deviation of the ratio under $H_0(t)$ and $\tilde{\sigma}$ the standard deviation in (2.22). Let $\phi_m^{\mathcal{P}}(\sigma)$ as in Equation (2.8). Under the alternative hypothesis $H_1(t)$, $p_{\theta-t}\neq 1-p_{\theta+t}$. Besides, $p_{\theta-t}\neq p_{\theta+t}$. Let define $\delta=1-\frac{p_{\theta-t}(1-p_{\theta-t})}{p_{\theta+t}(1-p_{\theta+t})}$. By hypothesis $\delta\neq 0$. Recall that

$$\frac{\mu_{\check{\mathcal{P}}_m}(\theta-t)}{\mu_{\check{\mathcal{P}}_m}(\theta+t)}=\frac{p_{\theta-t}(1-p_{\theta-t})}{p_{\theta+t}(1-p_{\theta+t})},\quad\text{then}\quad\frac{\mu_{\check{\mathcal{P}}_m}(\theta-t)}{\mu_{\check{\mathcal{P}}_m}(\theta+t)}=1-\delta.$$

Then, we get

$$\begin{aligned}\mathbb{P}_{H_1(t)}(\phi_m^{\mathcal{P}}(\sigma)=1)&=\mathbb{P}_{H_1(t)}\left(\left|\frac{m}{\tilde{\sigma}}\Big(R_{m,\theta}(t)-1+\delta-\delta\Big)\right|\ \geq\ q_{1-\alpha/2}\frac{\sigma}{\tilde{\sigma}}\right)\\&=\mathbb{P}_{H_1(t)}\left(\frac{m}{\tilde{\sigma}}\left(R_{m,\theta}(t)-\frac{\mu_{\check{\mathcal{P}}_m}(\theta-t)}{\mu_{\check{\mathcal{P}}_m}(\theta+t)}\right)-\frac{m}{\tilde{\sigma}}\delta\geq\ q_{1-\alpha/2}\frac{\sigma}{\tilde{\sigma}}\right)\\&\quad+\mathbb{P}_{H_1(t)}\left(\frac{m}{\tilde{\sigma}}\left(R_{m,\theta}(t)-\frac{\mu_{\check{\mathcal{P}}_m}(\theta-t)}{\mu_{\check{\mathcal{P}}_m}(\theta+t)}\right)-\frac{m}{\tilde{\sigma}}\delta\leq -q_{1-\alpha/2}\frac{\sigma}{\tilde{\sigma}}\right).\end{aligned}$$

Then

$$\mathbb{P}_{H_1(t)}(\phi_m^{\mathcal{P}}(\sigma)\xrightarrow[m\to\infty]{}1,$$

hence, we get the result. □

Proof of Corollary 2.4.3 . Considering the continuous mapping $\psi : x\mapsto\left(\frac{(2x-1)(3x-2)}{x(1-x)^2}\right)^{-\frac{1}{2}}$ and the fact that $\hat{p}_m(\theta+t)$ is a robust estimator of $p(\theta+t)$, we get that $\psi(\hat{p}_m(\theta+t))\xrightarrow[m\to\infty]{a.s.}\psi(p(\theta+t))$ where $\psi(p(\theta+t))=\frac{1}{\sigma(\theta+t)}$. Thus, applying the Slutsky Theorem to (3.10), we get

$$m\psi(\hat{p}_m(\theta+t))(R_{m,\theta}(t)-1)\xrightarrow[m\to\infty]{d,H_0}\psi(p(\theta+t))\mathcal{N}(0,\sigma^2(\theta+t)).$$

Hence the result. □

Proof of Proposition 2.4.5. For the sake of simplicity, let us note $\theta-t=u$ and $\theta+t=s$, for $t \in (0,\infty)$ and $\mu = \begin{pmatrix} 1-p_u \\ 1-p_s \end{pmatrix}$. We recall that, $\forall x \in \mathbb{R}$

$$\hat{F}_m(x^-) = \frac{1}{m^2}\sum_{i=1}^{m}\sum_{j=1}^{m} \mathbb{1}_{\{X_{i,j}<x\}}.$$

Furthermore, from the bivariate Central Limit Theorem,

$$m\left(\begin{pmatrix} \hat{F}_m(u^-) \\ \hat{F}_m(s^-) \end{pmatrix} - \begin{pmatrix} F(u^-) \\ F(s^-) \end{pmatrix}\right) \xrightarrow[m\to\infty]{d} \mathcal{N}\left(\begin{pmatrix} 0 \\ 0 \end{pmatrix}, \begin{pmatrix} (1-p_u)p_u & (1-p_u)p_s \\ (1-p_u)p_s & (1-p_s)p_s \end{pmatrix}\right).$$

Applying the Delta method using the function $g : \begin{pmatrix} x \\ y \end{pmatrix} \mapsto \dfrac{x}{1-y}$, it holds that

$$m\left(\frac{\hat{F}_m(u^-)}{1-\hat{F}_m(s^-)} - 1\right) \xrightarrow[m\to\infty]{d} \mathcal{N}\left(0, \nabla g(\mu)^T \begin{pmatrix} (1-p_u)p_u & (1-p_u)p_s \\ (1-p_u)p_s & (1-p_s)p_s \end{pmatrix} \nabla g(\mu)\right)$$

with $\nabla g(\mu) = \begin{pmatrix} \frac{1}{p_s} \\ \frac{1-p_u}{(p_s)^2} \end{pmatrix}$. Since under $H_0(t)$, $p_u = 1-p_s$, then,

$$\nabla g(\mu)^T \begin{pmatrix} (1-p_u)p_u & (1-p_u)p_s \\ (1-p_u)p_s & (1-p_s)p_s \end{pmatrix} \nabla g(\mu) = \begin{pmatrix} \frac{1}{p_s} & \frac{1}{p_s} \end{pmatrix} \begin{pmatrix} p_u p_s & p_s^2 \\ p_s^2 & p_u p_s \end{pmatrix} \begin{pmatrix} \frac{1}{p_s} \\ \frac{1}{p_s} \end{pmatrix} = \frac{2}{p_s}.$$

Then,

$$m\left(\frac{\hat{F}_m(u^-)}{1-\hat{F}_m(s^-)} - 1\right) \xrightarrow[m\to\infty]{d,H_0} \mathcal{N}\left(0, \frac{2}{p_s}\right).$$

Hence the result. ☐

Proof of Lemma 2.6.1. We recall from Equation (2.3) that we have, $\mu_{\mathcal{P}}(p_t,m) = 4p_t(1-p_t)m(m-1)$, and from Equation (2.4)

$$\sigma^2_{\mathcal{P}}(p_t,m) = 4p_t(1-p_t)((4m^2-7m+2) - 2p_t(1-p_t)(7m^2-13m+4)).$$

Then, the ratio is equal to

$$\frac{\sigma^2_{\mathcal{P}}(p_t,m)}{\mu_{\mathcal{P}}(p_t,m)} = \frac{(4-\frac{7}{m}+\frac{2}{m^2}) - 2p_t(1-p_t)(7-\frac{13}{m}+\frac{4}{m^2})}{(1-\frac{1}{m})}. \tag{2.23}$$

Let $r^\star_m := \dfrac{(4-\frac{7}{m}+\frac{2}{m^2})}{1-\frac{1}{m}}$, then,

$$\left|\frac{\sigma^2_{\mathcal{P}}(p_t,m)}{\mu_{\mathcal{P}}(p_t,m)} - r^\star_m\right| \leq \left|\frac{2p_t(1-p_t)(7m-13+\frac{4}{m})}{(m-1)}\right| \leq \left|14p_t(1-p_t)\right|.$$

Hence, uniformly in m,

$$\frac{\sigma^2_{\mathcal{P}}(p_t,m)}{\mu_{\mathcal{P}}(p_t,m)} \xrightarrow[p_t\to 0]{} r^\star_m. \tag{2.24}$$

Thus, as $m\to\infty$, $\dfrac{\sigma^2_{\mathcal{P}}(p_t,m)}{\mu_{\mathcal{P}}(p_t,m)}$ tends to $4 = \lim_{m\to\infty} r^\star_m$.

For the second item, we can note that $p_t(1-p_t)$ reaches its maximal value at $p_t = 1/2$. It follows that

$$\frac{\sigma^2_{\mathcal{P}}(p_t, m)}{\mu_{\mathcal{P}}(p_t, m)} \geq \frac{(4m^2 - 7m + 2) - \frac{1}{2}(7m^2 - 13m + 4)}{m(m-1)} \quad = \quad \frac{1}{2}\,.$$

Hence, we have proven that for m large enough,

$$\frac{1}{2} \leq \frac{\sigma^2_{\mathcal{P}}(p_t, m)}{\mu_{\mathcal{P}}(p_t, m)} \leq 4,$$

where the second part of the inequality is due to (2.23) and (2.24). □

Proof of Proposition 2.6.2. Let us first notice that $\mathbb{E}\left(\mathcal{P}(t_{m,\gamma})\right) = \mathbb{E}(\mathcal{P}(s_{m,\gamma}))$, since $p_{t_{m,\gamma}} = 1 - \dfrac{1}{m^\gamma} = 1 - p_{s_{m,\gamma}}$. In order to prove the result, we will establish that $\forall\, a_1, a_2 \in \mathbb{R}$

$$\sqrt{\frac{1}{4\mathbb{E}\left(\mathcal{P}(t_{m,\gamma})\right)}}\left(a_1\left(\mathcal{P}\left(t_{m,\gamma}\right) - \mathbb{E}\left(\mathcal{P}\left(t_{m,\gamma}\right)\right)\right) + a_2\left(\mathcal{P}\left(s_{m,\gamma}\right) - \mathbb{E}\left(\mathcal{P}\left(s_{m,\gamma}\right)\right)\right)\right)$$
$$\xrightarrow[m\to\infty]{d} \mathcal{N}(0, a_1^2 + a_2^2).$$

To prove this statement, we will follow the same idea as in the proof of Theorem 2.3.3, introducing the following notations, similar to (2.20),

$$\widetilde{W}^m_{l,k} = \sqrt{\frac{1}{4\mathbb{E}\left(\mathcal{P}(t_{m,\gamma})\right)}}\Bigg(a_1\left(\mathcal{P}_m(t_{m,\gamma}) - \mathbb{E}(\mathcal{P}_m(t_{m,\gamma}))\right) + a_2\left(\mathcal{P}_m(s_{m,\gamma}) - \mathbb{E}\left(\mathcal{P}_m(s_{m,\gamma})\right)\right)\Bigg)$$

and finally, $S_m = \sum_{l=1}^m \sum_{k=2}^m \widetilde{W}^m_{l,k}$.
In order to show that $S_m \xrightarrow[m\to\infty]{d} \mathcal{N}(0, a_1^2 + a_2^2)$, we will check that the family $\{\widetilde{W}^m_z, z \in V_m\}$ satisfies the three conditions of Proposition 2.7.2.

To show that $\{\widetilde{W}^m_z, z \in V_m\}$ satisfies *(i)*, we proceed as in the proof of Theorem 2.3.3. For $\epsilon > 0$ and choosing $p > \dfrac{4}{2-\gamma}$, we get that,

$$\begin{aligned}\sum_{(l,k)\in V_m} \mathbb{P}\left(\left|\widetilde{W}^m_{l,k}\right| \geq \epsilon\right) \leq \sum_{(l,k)\in V_m} \frac{\mathbb{E}\left(\left|\widetilde{W}^m_{l,k}\right|^p\right)}{\epsilon^p} &\leq \frac{\left(2\sum_{i=1}^2 |a_i|\right)^p m(m-1)}{\epsilon^p\,\sqrt{\left(4 \times 4m(m-1) \times \frac{1}{m^\gamma}(1 - \frac{1}{m^\gamma})\right)^p}}\,, \\ &\leq Cm^{2-\frac{1}{2}p(2-\gamma)},\end{aligned}$$

for some positive constant C. As $p > \dfrac{4}{2-\gamma}$, $Cm^{2-\frac{1}{2}p(2-\gamma)} \xrightarrow[m\to\infty]{} 0$.
To show that $\{\widetilde{W}^m_z, z \in V_m\}$ satisfies *(ii)*,

$$\begin{aligned}\sum_{(l,k)\in V_m} \mathbb{E}\left(\left(W^m_{l,k}\right)^2\right) &= \sum_{(l,k)\in V_m} \frac{1}{4\mathbb{E}\left(\mathcal{P}(t_{m,\gamma})\right)} \mathrm{Var}\left(a_1 Y_{l,k}\left(t_{m,\gamma}\right) + a_2 Y_{l,k}\left(s_{m,\gamma}\right)\right) \\ &\leq \frac{2m(m-1)}{4\mathbb{E}\left(\mathcal{P}\left(t_{m,\gamma}\right)\right)}\left(a_1^2 \mathrm{Var}\left(Y_{1,2}\left(t_{m,\gamma}\right)\right) + a_2^2 \mathrm{Var}\left(Y_{1,2}\left(s_{m,\gamma}\right)\right)\right).\end{aligned}$$

Let us recall that $Y_{1,2}(t)$ is a sum of two Bernoulli random variables with parameter $2p_t(1-p_t)$. Hence, $\mathrm{Var}\,(Y_{1,2}(t_{m,\gamma})) \leq 2p_{t_{m,\gamma}}(1-p_{t_{m,\gamma}})$.
Since $p_{t_{m,\gamma}} = 1 - p_{s_{m,\gamma}}$, we have

$$\sum_{(l,k)\in V_m} \mathbb{E}\left(\left(W_{l,k}^m\right)^2\right) \leq \frac{m(m-1)}{4\mathbb{E}\left(\mathcal{P}\left(t_{m,\gamma}\right)\right)}(a_1^2+a_2^2) \times 8p_{t_{m,\gamma}}(1-p_{t_{m,\gamma}}) \;\leq\; a_1^2+a_2^2.$$

Thus, the sum is bounded. Finally, for (iii),

$$\begin{aligned}
\mathrm{Var}(S_m) &= \mathrm{Var}\left(\sqrt{\frac{1}{4\mathbb{E}\left(\mathcal{P}(t_{m,\gamma})\right)}}\left(a_1\mathcal{P}_m(t_{m,\gamma}) + a_2\mathcal{P}_m(s_{m,\gamma})\right)\right)\\
&= \frac{1}{4\mathbb{E}\left(\mathcal{P}(t_{m,\gamma})\right)}\left(a_1^2\mathrm{Var}(\mathcal{P}(t_{m,\gamma})) + 2a_1a_2\mathrm{Cov}(\mathcal{P}(t_{m,\gamma}),\mathcal{P}(s_{m,\gamma})) + a_2^2\mathrm{Var}(\mathcal{P}(t_{m,\gamma}))\right)\\
&= \frac{(a_1^2+a_2^2)}{4\mathbb{E}(\mathcal{P}(t_{m,\gamma}))}\mathrm{Var}(\mathcal{P}(t_{m,\gamma})) + \frac{1}{4m(m-1)}\frac{2a_1a_2}{4p_{t_{m,\gamma}}(1-p_{t_{m,\gamma}})}\mathrm{Cov}(\mathcal{P}(t_{m,\gamma}),\mathcal{P}(s_{m,\gamma})). \qquad (2.25)
\end{aligned}$$

Note that $s_{m,\gamma} > t_{m,\gamma}$, thus, by Proposition 2.3.2,

$$\begin{aligned}
\mathrm{Cov}\,(\mathcal{P}(t_{m,\gamma}),\mathcal{P}(s_{m,\gamma})) = 4\,p_{s_{m,\gamma}}(1-p_{t_{m,\gamma}})((&4m^2-7m+2)\\
&- 2p_{t_{m,\gamma}}(1-p_{s_{m,\gamma}})(7m^2-13m+4)\\
&+ 2(p_{t_{m,\gamma}}-p_{s_{m,\gamma}})(3m^2-6m+2)).
\end{aligned}$$

Given that $p_{t_{m,\gamma}} = 1 - p_{s_{m,\gamma}}$, we have

$$\begin{aligned}
\mathrm{Cov}\,(\mathcal{P}(t_{m,\gamma}),\mathcal{P}(s_{m,\gamma})) = 4\,&(1-p_{t_{m,\gamma}})^2((4m^2-7m+2)\\
&- 2p_{t_{m,\gamma}}^2(7m^2-13m+4) + 2(2p_{t_{m,\gamma}}-1)(3m^2-6m+2)).
\end{aligned}$$

Recall that, $p_{t_{m,\gamma}} \to 1$, thus, $\dfrac{\mathrm{Cov}\,(\mathcal{P}(t_{m,\gamma}),\mathcal{P}(s_{m,\gamma}))}{m(m-1)p_{t_{m,\gamma}}(1-p_{t_{m,\gamma}})} \xrightarrow[m\to\infty]{} 0$. Hence, from Equation (2.25), we get that $\mathrm{Var}\,(S_m) \xrightarrow[m\to\infty]{} a_1^2+a_2^2$, since $\dfrac{\mathrm{Var}\,(\mathcal{P}(t_{m,\gamma}))}{\mathbb{E}\,(\mathcal{P}(t_{m,\gamma}))} \xrightarrow[m\to\infty]{} 4$ by Lemma 2.6.1.

□

ACKNOWLEDGMENTS: This work has been partially supported by the project ANR MISTIC (ANR-19-CE40-0005) and by the French government, through the 3IA Côte d'Azur Investments in the Future project managed by the National Research Agency (ANR) with the reference number ANR-19-P3IA-0002.

2.A1 Numerical illustrations of Theorem 2.3.3

In order to illustrate the multivariate CLT of Theorem 2.3.3, we follow the example given by Di Bernardino et al. (2014). We start by simulating a sample of 900 images of size 1000×1000 pixels generated from a Uniform distribution and compute the perimeter without the border using the Algorithm 3 associated to the binary image for a threshold $t = 0.5$. We create the histogram of the variable:

$$A_m(t) = \frac{m\left(\check{\mathcal{P}}_m(t) - \mathbb{E}(\check{\mathcal{P}}_m(t))\right)}{\sqrt{\sigma^{\star 2}(t)}} \tag{2.26}$$

and compare it to the plot of Gaussian density. To illustrate the bivariate CLT, let $s = 0.6$ and $t = 0.2$, we use the Python function `stats.normaltest` from `scipy`'s library to do a normal test based on D'Agostino and Pearson (1973)'s method. This function tests whether a sample differs from a normal distribution. Thus, we plot the p-value of the test conducted on the projection $\cos(\theta)A_m(t)+\sin(\theta)A_m(s)$ for $\theta \in [0, 2\pi)$. This method mimics the Cramèr-Wold Theorem 2.7.1. We also use the Mahalanobis distance to show the joint Gaussianity. This illustration is based on the fact that if $\mathbf{X} \sim \mathcal{N}_d(\mu, \Sigma)$ then, the Mahalanobis distance D^2 with entries D_i^2

$$D_i^2 = (X_i - \mu)'\Sigma^{-1}(X_i - \mu), i = 1, \dots, m^2$$

is distributed according to a χ_d^2-distribution with d degrees of freedom. Using the theoretical value of $\Sigma^\star$ and numerically estimating the sample average μ, we compute the value D_i^2 and compare it with a χ_d^2-distribution, using the QQ-plot method. In Figure 2.10, we gathered the obtained results from these numerical studies which confirm the joint normal behaviour of $(A_m(t), A_m(s))$.

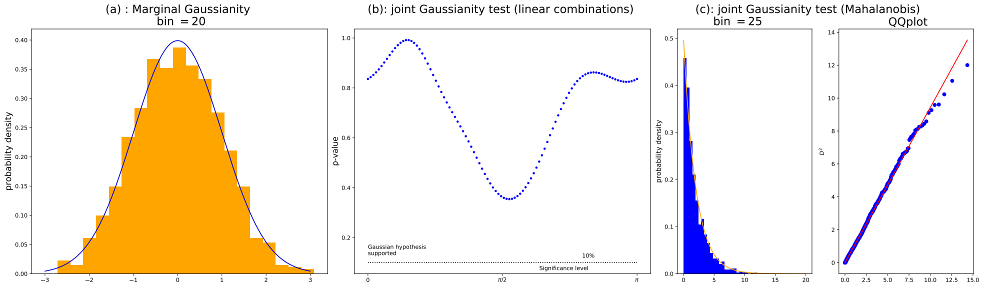

Figure 2.10 – **(a.)** Univariate Gaussianity of $A_m(t)$ in (2.26) for $m = 1200$ and $t = 0.5$ for a bin size equal to 20. The solid blue line represents the corresponding standard Gaussian density. We propose two validation methods of the multivariate Gaussianity of the bivariate vector $(A_m(s), A_m(t))$ with $s = 0.6$ and $t = 0.2$. **(b.)** $p-$value for $\cos(\theta)A_m(t) + \sin(\theta)A_m(s)$ for $\theta \in [0, 2\pi)$, computed using the function `stats.normaltest` from `scipy`. **(c.)** Estimated probability density of D^2 (blue histogram) and theoretical Chi-squared density (red curve). QQ-plot between the theoretically predicted χ_2^2 quantiles and the empirical quantiles of D^2.

2.A2 Comparison between $\sigma^2(s)$ and $\sigma^2_{\text{k-s}}(s)$ variances

Figure 2.11 below provides a comparison between the two variance values $\sigma^2(s)$ in (2.7) (red full line) and $(\sigma_{\text{k-s}})^2(s)$ in (2.14) (black dashed line), for $p_s \in (0, 0.5)$. As notice in Remark 4, Figure 2.11 shows that the variance of the ratio computed using the perimeter is lower than the variance of the ratio computed using a Kolmogorov Smirnov method.

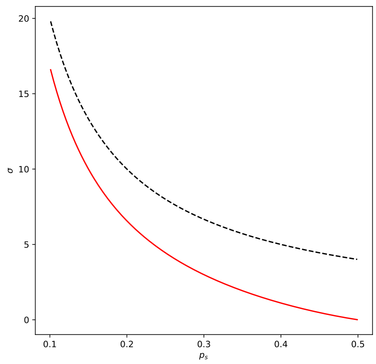

Figure 2.11 – Variance values $\sigma^2(s)$ in (2.7) in (red full line) and $(\sigma_{\text{k-s}})^2(s)$ in (2.14) (black dashed line), for $p_s \in (0.1, 0.5)$

2.A3 Optimization problem for the variance function

For statistical purposes, it is important to identify the points where the variance function in Equation (2.4) reaches its maximum and minimum values.

Let us consider the following optimization problem :

$$\begin{aligned} p_t^\star &= \operatorname{argmin}_{p_t} \sigma^2_{\check{\mathcal{P}}}(p_t, m) \\ &= \operatorname{argmin}_{p_t} \frac{4}{m^4} p_t(1-p_t)((4m^2-7m+2) - 2p_t(1-p_t)(7m^2-13m+4)). \end{aligned}$$

By using XCAS, we get that the set of extrema of this variance function is equal to

$$\left\{ \frac{1}{2} - \frac{\sqrt{84m^4 - 324m^3 + 416m^2 - 200m + 32}}{28m^2 - 52m + 16}, \frac{1}{2}, \frac{1}{2} + \frac{\sqrt{84m^4 - 324m^3 + 416m^2 - 200m + 32}}{28m^2 - 52m + 16} \right\} := \{\alpha_1, \alpha_2, \alpha_3\}.$$

By doing an analytical study, we get the maximum value of the variance is reached on α_1 and α_3 and the minimum value for α_2 (see Figure 2.12 for an illustration in the Uniform white noise model).

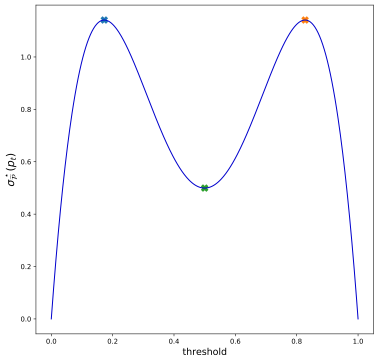

Figure 2.12 – Curve of the variance function in Equation (2.4) for a Uniform white noise model for $m = 1024$, the extrema are reached at $p_t \in \{0.172, 0.5, 0.82\}$.

3 Sationnary Gaussian framework

This chapter resumes the work presented in the preprint (Abaach et al. (2023)), M. Abaach, H. Biermé, E. Di Bernardino, and A. Estrade. Local isotropy test based on the oriented perimeter of digitalized images. working paper, Mar. 2023. hal-04037394. URL https://hal.science/hal-04037394/.

3.1 Introduction

The main objective of our study is to be able to decide whether the texture of a grey-level image is isotropic or not. By the texture of an image, we mean the microscopic structure that is captured by the covariance function at the pixels scale. In order to achieve this goal, we propose a methodology built on a statistical test for which all steps are rigorously validated. The originality of our approach is to stick on the geometrical features of the image without trying to identify the full distribution of the underlying Gaussian random field that is supposed to serve as a model. More precisely, our observable statistic will be the perimeter of the black domain of the thresholded image.
In the previous literature, a number of non-parametric tests of directional dependence have been developed using both the spatial and spectral representations of random fields (see, e.g, Weller and Hoeting (2016), Guan et al. (2004)). A comparative study with these methods is proposed in Section 3.5. The present paper is part of the methodological literature that deals

with statistical inference based on geometrical observable features given by the Lipschitz-Killing curvatures (LKC) of the excursion sets. In image analysis, *i.e.* in a two dimensional setting, an excursion set is a region of the image where the pixel's values are higher than a fixed level, the level set is the boundary of the excursion set and the LKC's are the three natural Minkowski functionals: Euler characteristic (number of connected components minus number of holes), perimeter (length of the level set), area (Lebesgue measure of the excursion set). Although such type of statistical study of the excursion set is an old engineers task (see Longuet-Higgins (1957) for instance), it has recently received much attention from a probability theory and mathematical statistics point of view. To cite some of these papers, let us quote Worsley (1996) or Telschow et al. (2020) where the localization of peaks is inferred from the observation of the Euler characteristic of excursion sets in neuro-imaging and in the Cosmic Microwave Background radiation, Molina and Feito (2002) where isotropy is tested through the observation of the gradient, Di Bernardino et al. (2017) or Biermé et al. (2019) where a test of Gaussianity is produced based on the Euler characteristic of excursion sets, Abaach et al. (2021) where a test of symmetry is produced based on the perimeter of thresholded images. Among this dense literature, let us focus on two specific articles, Cabaña (1987); Berzin (2021), with a similar objective as ours, namely a test of isotropy, based on similar observations, namely the length of level sets. Both papers are concerned with affine two-dimensional continuous random fields, *i.e.* stationary random fields X defined on $\mathbb{R}^2$ and given as $X(\cdot) = Z(A\cdot)$, where Z is centered, stationary and isotropic defined on $\mathbb{R}^2$ and A is a deterministic matrix that can be reduced to $A = \begin{pmatrix} a & 0 \\ 0 & b \end{pmatrix} \begin{pmatrix} \cos\theta & \sin\theta \\ -\sin\theta & \cos\theta \end{pmatrix}$, $a, b \in \mathbb{R}$, $\theta \in [0, 2\pi)$. Within this continuous parametric frame, X is isotropic in distribution if and only if $a = b$. In both articles, a test of isotropy is constructed, based on the measurement of the respective horizontal and vertical components of the length of the level sets. In the former article, some mixing condition yields a Gaussian asymptotics of the normalized level set length, while in the latter article, a Gaussian condition yields a similar result. This central limit theorem is the crux for establishing a fair statistical test. Let us insist on the continuous setting that is assumed in those papers whereas our study definitively deals with discrete images. Our precise setting will be presented later on in the introductory section. Implementations of this type of "geometrical" methods can be found in medical imaging and image analysis in general, cosmology, hydrology, sea waves modelling, etc.

As an example, let us exhibit some medical images that can be handled with our methodology. In this introductory part, we just show the images and a first tentative of descriptive statistics. The statistical results that we are able to infer from our methodology is detailed at the end of the present paper (see Section 3.6). We analyzed 211 X-ray images of calcaneus bones in order to detect the eventual anisotropic nature of the micro-architecture since bone texture anisotropy is of special interest for the diagnosis of osteoporosis (see Chappard et al. (2005) for instance or Wani and Arora (2020) for a review). We first applied a preprocessing step in order to get stationary images and then consider the thresholded images at various empirical quantile levels t_α, *i.e.* for $\alpha \in (0, 1)$, there exists a proportion α of the image values smaller than t_α.

As observable statistics, we use the respective numbers of horizontal and vertical edges that separate a black pixel from a white pixel of the binary image. We name these counters as oriented perimeters, horizontal and vertical respectively. In case of an isotropic texture, the ratio of the two oriented perimeters should be close to one. At the opposite, if the observed ratio is far from one, then some anisotropy is expected in the microscopic texture of the image. The ratio has been computed for each image of the panel at various empirical quantile levels t_α. In Figure 3.2, the distribution of the obtained ratios is summarized in a

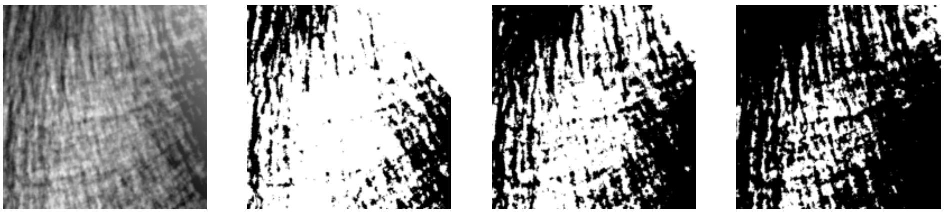

Figure 3.1 – Pre-processed bone X-ray image, with its associated excursion sets thresholded at the first, second and third quartiles.

boxplot for each level.

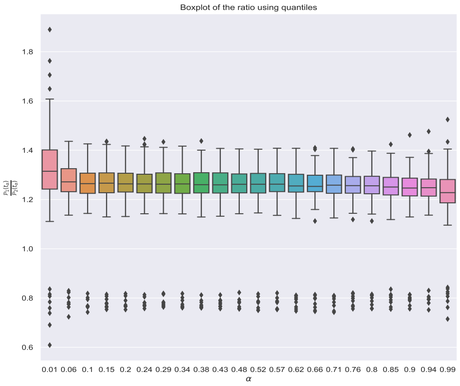

Figure 3.2 – For $\alpha \in [0.01, 0.99]$, we represent the boxplot of the ratio between the two oriented perimeters computed at t_α level, $\mathcal{P}^1(t_\alpha), \mathcal{P}^2(t_\alpha)$, for stationary thresholded images of bone X-rays.

We observe that the boxplots of the ratio between the horizontal and vertical perimeters are not distributed around one, whatever the considered level. Moreover, for almost all images the observed ratios are above one whereas for some images extreme values are observed below one. We checked the fact that these below one extreme cases all belong to the same small group of images. Nevertheless, what is relevant on this sample of X-ray images of calcaneus is that the anisotropy of the texture can be revealed at any threshold level by simply comparing two single counters. It is worth to note that this anisotropy, although obvious through the proposed image analysis procedure, is not perceptible to the naked eye. With a very different approach based on quadratic variations, the same sample of images has been analyzed in Biermé et al. (2009) and the same conclusion has been obtained: the calcaneus X-ray images are anisotropic. In Richard (2016), the investigation of the anisotropy property of textures was applied to medical images, in combination with a measure of texture roughness, as a means of detecting lesions in mammograms.

Let us now present in details what is the content of our study. As already said, we aim at constructing a statistical test of isotropy based on the observation at small scale of the image. Our observation will be very sparse since it is reduced to count the horizontal and vertical edges that are involved at the interface between the black and the white pixels of the binary image. This geometrical quantity is nothing but the discrete perimeter (see Biermé and Desolneux (2021)), considering separately the horizontal contribution and the vertical one. In our inference only elementary steps are performed in order to compute this geometrical feature. This has a low computational cost compared for instance to isotropy-testing procedure based on spectral methods requiring matrix inversions (see e.g., Guan et al. (2004)).

Assuming that the original grey-level image is a discrete Gaussian stationary field, we are able to explicitly compute the first two moments of the so-called oriented perimeter. Our study of moments includes the asymptotic behavior as the number of pixels goes to infinity. We then establish a Central Limit Theorem for the joint oriented perimeters at various levels under a summability condition of the covariance function. The perimeter being given as a sum of functionals of correlated Gaussian variables, the main argument for the CLT that we use is borrowed from Breuer-Major result as exposed in Arcones (1994). Let us note that a similar study was performed in Abaach et al. (2021) but under a very different context since the underlying Gaussian field was supposed to be a white noise. The induced totally independent structure of the pixels led to simple computations and estimations which are not allowed anymore in the correlated situation that we consider in the present paper.

The next step of our method consists in building the promised statistical test. More precisely, ρ being the covariance function of the Gaussian field and (e_1, e_2) being the canonical basis of $\mathbb{R}^2$, we consider the null hypothesis $H0: \ \rho(e_1) = \rho(e_2)$ that we call "local pixel isotropy" through a misuse of language. We exhibit a statistic depending on the ratio of the oriented perimeters that goes to one under $H0$ thanks to the CLT previously established. Moreover, we prove the consistency of the proposed test. Let us insist on the fact that our test is a non-parametric one so that the alternative hypothesis reduces to $H1: \ \rho(e_1) \neq \rho(e_2)$. A by-product of our method is the measurement of the anisotropy through the ratio between the oriented perimeters.

The theoretical study is completed by extensive numerical illustrations based on simulated data. We sample Gaussian fields with compact support covariances and use affine deformations to get anisotropic models. The performances of our test are illustrated on those models. The crucial question of estimating the variance of the perimeter is also explored. Finally, we apply our method to the calcaneus X-ray images that we have already presented. It allows us to infer properties and to estimate quantities that could be of interest from a medical point of view.

The paper is organized as follows. Section 3.2 is devoted to the presentation of the mathematical framework, namely the grid that defines the pixels and implies the discrete nature of the Gaussian random field that we use as a model for the grey-level image. We also precisely define the notion of discrete oriented perimeters that we consider all over the article. In Section 3.3, we proceed to the statistical study of the oriented perimeters by computing their first two moments and establishing a joint central limit theorem for both various directions and various levels. This central limit theorem allows us to build the announced local pixel isotropy test and to establish its asymptotic properties. Section 3.4 contains the numerical studies. This section is dedicated to Monte Carlo estimations of the variance of the oriented perimeter for a Gaussian affine model and to numerical illustrations of the local pixel isotropy test for the same toy model. In Section 3.5 we propose a comparison in terms of obtained p_{values} with the semivariogram based isotropy test proposed by Guan et al. (2004). The statistical analysis for bone X-rays images can be found in Section 3.6. We end the paper by a concluding Section 3.7. We provide some supplementary lemmas that are used in the computation of the second moment of the oriented perimeter and in the numerical computations (see Appendix 3.A1) as well as the proofs of the results and theorems presented in the paper (see Appendix 3.A2).

3.2 Mathematical framework

3.2.1 Construction of the binary image

Let m be an integer with $m \geq 2$. Without loss of generality, we consider our observation window as the unit square $S = [0, m]^2$ and we divide it into m^2 pairwise disjoint squares. We denote by e_1, e_2 the elements of the canonical basis of $\mathbb{R}^2$, and we introduce the following notations.

- $\mathbb{G}_m := [0, m)^2 \cap \mathbb{Z}^2$ is the set of points in S that are considered. We write $x = (x_1, x_2)$ with $x_1, x_2 \in \{0, \dots, m-1\}$ for any $x \in \mathbb{G}_m$.
- For $x \in \mathbb{G}_m$, $C_m(x) := x + [0,1]^2$ will be referred to as a *cell*. Note that $S = \cup_{x \in \mathbb{G}_m} C_m(x)$.
- We denote by $\mathcal{E}_m^{(1)}$, $\mathcal{E}_m^{(2)}$ the set of vertical and horizontal edges in $\mathring{S}$, and for each $x \in \mathbb{G}_m$, we denote by $w_i(x)$ the intersection $C_m(x) \cap C_m(x + e_i)$ with $i \in \{1, 2\}$, that is an edge corresponding to a segment of length 1. And finally,

$$\mathbb{G}_m^{(1)} := \left\{ x \in \mathbb{G}_m;\ C_m(x) \cap C_m(x + e_1) \subset \mathring{S} \right\} = [\![0, m-2]\!] \times [\![0, m-1]\!],$$

$$\mathbb{G}_m^{(2)} := \left\{ x \in \mathbb{G}_m;\ C_m(x) \cap C_m(x + e_2) \subset \mathring{S} \right\} = [\![0, m-1]\!] \times [\![0, m-2]\!].$$

Figure 3.3 shows an example of a square tiling with $m = 4$.

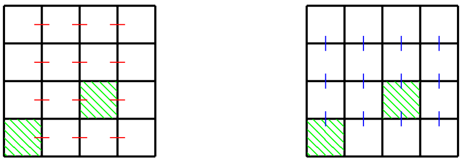

Figure 3.3 – Square tiling for $m = 4$ and associated cells $C_4((0,0))$ and $C_4((2,1))$ (green stripes). We represent the vertical edges w_1 in red and the horizontal ones w_2 in blue.

Using this square tiling, we observe $(X_x)_{x \in \mathbb{G}_m}$, which we assume coincides with values of a stationary Gaussian random field $(X_x)_{x \in \mathbb{Z}^2}$. The stationarity hypothesis means that for all $h \in \mathbb{Z}^2$,

$$\left(X_{x+h}; x \in \mathbb{Z}^2\right) \overset{fdd}{=} \left(X_x; x \in \mathbb{Z}^2\right),$$

where fdd denotes finite-dimensional distributions. We denote by $\rho(x) := \mathrm{Cov}\left(X_0, X_x\right),\ x \in \mathbb{Z}^2$, the covariance function of X. Considering a threshold parameter $t \in \mathbb{R}$, we introduce the associated binary image $Z_t^{(m)} = \left(\mathbb{1}_{\{X_x \geq t\}}\right)_{x \in \mathbb{G}_m}$ where each cell $C_m(x)$ is associated to black or white according to whether $X_x \geq t$ or $X_x < t$. In Figure 3.4 we display several random generations of Gaussian random fields and their associated thresholded images. Sampling is provided by using the Matlab function `stationary_Gaussian_process` (MATLAB (2021)).

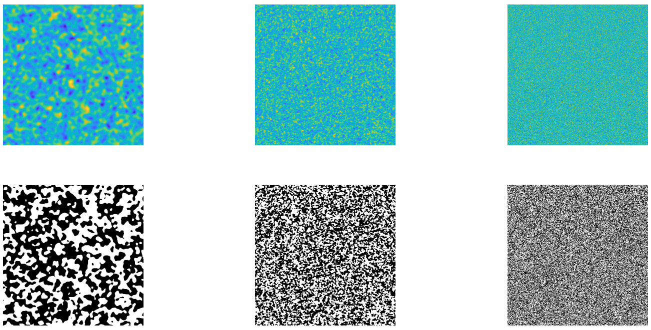

Figure 3.4 – Generations of Gaussian random fields with covariance $\rho(x) = e^{-\kappa||x||^2}$ (first row) and their respective thresholded image $Z_t^{(m)}$ for $t = 0$ and $m = 512$ (second row). We consider various values for κ, from left to right $\kappa = 0.01, 0.1, 1$.

3.2.2 Oriented perimeter of a binary image

For $t \in \mathbb{R}$, let $Z^{(m)} = Z_t^{(m)}$ be the binary image at the given threshold $t \in \mathbb{R}$. Following the approach presented in Biermé and Desolneux (2021), for each edge $w \in \mathcal{E}_m = \mathcal{E}_m^{(1)} \cup \mathcal{E}_m^{(2)}$, we aim to know whether w contributes to the perimeter of the black component of $Z^{(m)}$ (see Figure 3.5). Making use of the additive nature of the perimeter, one can start by computing the oriented perimeter given each direction, horizontal and vertical.

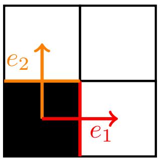

Figure 3.5 – A single horizontal edge in orange and a vertical one depicted in red contribute to the perimeter, $\mathcal{P} = 2$.

Following this consideration, we define the random quantity,

$$f_t^{(i)}(x) := \mathbb{1}_{\{\min(X_x, X_{x+e_i}) < t \leq \max(X_x, X_{x+e_i})\}}, \qquad x \in \mathbb{G}_m^{(i)}, \tag{3.1}$$

which takes into account the eventual contribution of the edge $w_i(x)$ to the perimeter of the black component of $Z^{(m)}$.

Let us now introduce the main tool of the present work.

Definition 3.2.1 (Oriented perimeter of a binary image $Z^{(m)}$).
For $t \in \mathbb{R}$, we denote by $\mathcal{P}_m^{(i)}(t)$ the sum of all contributions over the ith direction (vertical for $i = 1$ and horizontal for $i = 2$) and we call it the oriented perimeter of the binary image $Z^{(m)}$,

$$\mathcal{P}_m^{(i)}(t) = \sum_{x \in \mathbb{G}_m^{(i)}} f_t^{(i)}(x). \tag{3.2}$$

The perimeter of $Z^{(m)}$ is given by $\mathcal{P}_m(t) := \mathcal{P}_m^{(1)}(t) + \mathcal{P}_m^{(2)}(t)$.

3.3 Statistics of the oriented perimeter

3.3.1 First moment

Let us start this study by investigating the first moment of the oriented perimeter $\mathcal{P}_m^{(i)}(t)$. The study of the second moment is postponed to Section 3.3.2.

In view of Equation (3.1), we make an observation that will appear very useful in the following: for any $a, b, t \in \mathbb{R}$,

$$\min(a,b) \leq t \leq \max(a,b) \iff |2t-(a+b))| \leq |b-a|\,.$$

Noting that for any $x \in \mathbb{G}_m^{(i)}$, we have $\mathbb{P}(X_x = X_{x+e_i}) = \mathbb{P}(X_0 = X_{e_i}) = 0$ as soon as $\rho(e_i) \neq 1$, we get

$$f_t^{(i)}(x) = \mathbb{1}_{\{|2t-(X_x+X_{x+e_i}))| \leq |X_x - X_{x+e_i}|\}} \quad a.s. \tag{3.3}$$

Theorem 3.3.1 (First moment of the oriented perimeter)**.** *We assume that* $(X_x)_{x\in\mathbb{G}_m}$ *is a stationary Gaussian centered with unit variance random field. Let* $i \in \{1,2\}$ *and let us denote by* $\rho(e_i) = \operatorname{Cov}(X_0, X_{e_i}) \in [-1,1]$. *Let* $t \in \mathbf{R}$, *the expected value of the oriented perimeter in* (3.2) *is given by*

$$\mathbb{E}\left(\mathcal{P}_m^{(i)}(t)\right) = m(m-1)\mathbb{E}\left(f_t^{(i)}(0)\right) = m(m-1)h(t,\rho(e_i)),$$

where

- *if* $c \neq -1$,

$$\begin{aligned} h(t,c) &= \int_c^1 \frac{\exp(-t^2/(1+u))}{\pi\sqrt{(1-u^2)}}\,du \qquad (3.4)\\ &= \mathbb{E}\left(\Phi\left(\frac{2t+\sqrt{2(1-c)}|N|}{\sqrt{2(1+c)}}\right) - \Phi\left(\frac{2t-\sqrt{2(1-c)}|N|}{\sqrt{2(1+c)}}\right)\right), \qquad (3.5)\end{aligned}$$

with $N \sim \mathcal{N}(0,1)$ *and* Φ *being the cumulative distribution function of the standard Gaussian;*

- *if* $c = -1$, $h(t,-1) = 2\left(1-\Phi(|t|)\right)$.

The proof of Theorem 3.3.1 is postponed to Appendix 3.A2.

Let us emphasize that Equation (3.4) yields

$$h(t,c) \underset{c\to 1^-}{\sim} \frac{\sqrt{1-c}}{\pi\sqrt{2}}\exp(-t^2/2).$$

In particular, this situation occurs, assuming to observe the discretisation of a continuous Gaussian field Y on a grid of small resolution $\varepsilon > 0$ such that $X(x) = Y(\varepsilon x)$, $x \in \mathbf{Z}^2$ since in this case $1-\rho(e_i) = \frac{1}{2}\operatorname{Var}(Y(\varepsilon e_i) - Y(0)) \underset{\varepsilon\to 0}{\to} 0$. Then Theorem 3.3.1 extends the corresponding result of Theorem 3.2 in Biermé and Desolneux (2021) where the asymptotic behavior for $\varepsilon \to 0$ is computed in the case of positively correlated Gaussian field. Note also that, in this *infill* regime, the ratio $\mathbb{E}\left(\mathcal{P}_m^{(1)}(t)\right)/\mathbb{E}\left(\mathcal{P}_m^{(2)}(t)\right)$ is therefore invariant in regard to $t \in \mathbb{R}$.

Remark 5 (Degenerate dependence cases)**.**

- In the case of a fully dependent field, *i.e* $\rho(e_i) = 1$, then $\mathbb{E}\left(\mathcal{P}_m^{(i)}(t)\right) = 0$.
- In the independent case, *i.e.* $\rho(e_i) = \mathrm{Cov}\left(X_0, X_{e_i}\right) = 0$, from Equation (3.5), we can write,

$$\begin{aligned}\mathbb{E}\left(\mathcal{P}_m^{(i)}(t)\right) &= m(m-1)\mathbb{E}\left(\Phi\left(\sqrt{2}\,t + |N|\right) - \Phi\left(\sqrt{2}\,t - |N|\right)\right)\\ &= 2m(m-1)\Phi(t)\left(1-\Phi(t)\right),\end{aligned}$$

  where we get the second identity by applying the variable change $(y,z) \mapsto \left(\frac{y-z}{\sqrt{2}}, \frac{y+z}{\sqrt{2}}\right)$. In this *i.i.d.* setting, we recover the same result as in Abaach et al. (2021) (see Proposition 3.1).

Integrating $\mathbb{E}(\mathcal{P}_m^{(i)}(t))$ along t in $\mathbb{R}$ with function h given by Equation (3.4) and using Fubini-Tonelli Theorem, we deduce the next corollary.

Corollary 3.3.2. *Under the same assumptions as in Theorem 3.3.1, it holds that, for* $i = 1, 2$,

$$\int_{\mathbb{R}} \mathbb{E}\left(\mathcal{P}_m^{(i)}(t)\right) dt = \frac{2m(m-1)}{\sqrt{\pi}} \left(\sqrt{1-\rho(e_i)}\right).$$

In image processing, the total variation of an image $u \in L^1_{loc}(\mathbf{R}^2)$ which is given by $\int_S |\nabla u| dx$ is a common and well studied object. It is possible to link this quantity to the perimeter of u, by applying the coarea formula, $\int_S |\nabla u| dx = \int_{\mathbb{R}} \mathcal{P}(t) dt$ with $\mathcal{P}(t)$ being the perimeter associated to the level set of the image u at level t. The above corollary provides a simple expression for the first moment of the total variation and links it directly to $\rho(e_i)$, the covariance evaluated in the ith direction. Note that it could be used as an estimator for $\rho(e_i)$.

Let us now remark that, for all $t \in \mathbf{R}$, the map $c \mapsto h(t,c)$ introduced in Theorem 3.3.1, Equation (3.4) is strictly non-increasing on $(-1,1)$. It follows that the corresponding result holds for the expected oriented perimeter.

Corollary 3.3.3. *Let* $\overline{X}, \tilde{X}$ *be two stationary centered Gaussian random fields with unit variance, and* $\bar{\rho}, \tilde{\rho}$ *their respective covariance structure. We have the following result: for* $1 \leq i, j \leq 2$,

$$\textit{if} \quad \tilde{\rho}(e_i) < \bar{\rho}(e_j) \quad \textit{then} \quad \mathbb{E}\left(\mathcal{P}_{m,\tilde{\rho}}^{(i)}(t)\right) > \mathbb{E}\left(\mathcal{P}_{m,\bar{\rho}}^{(j)}(t)\right),\ \forall t \in \mathbb{R}.$$

As a consequence, $\mathbb{E}\left(\mathcal{P}_m^{(1)}(t)\right) \neq \mathbb{E}\left(\mathcal{P}_m^{(2)}(t)\right)$ if and only if $\rho(e_1) \neq \rho(e_2)$. Now, assuming that the field X is isotropic, one consequence would be that $\rho(e_1) = \rho(e_2)$, which is equivalent to $\mathbb{E}\left(\mathcal{P}_m^{(1)}(t)\right) / \mathbb{E}\left(\mathcal{P}_m^{(2)}(t)\right) = 1$. Hence, in the case of isotropy, the ratio $\mathcal{P}_m^{(1)}(t)/\mathcal{P}_m^{(2)}(t)$ would be distributed around 1. This consideration will be crucial for the proposed local pixel isotropy testing procedure that we discuss later in Section 3.3.3.

3.3.2 Second moment

We now concentrate on the covariance function of the oriented perimeter. Let us consider a stationary Gaussian random field $(X_x)_{x\in\mathbb{Z}^2}$ with zero mean and unit variance whose covariance structure is given by $\rho(x) = \mathrm{Cov}\left(X_0, X_x\right)$. The stationarity assumption yields the next lemma. Its proof is postponed to Appendix.

Lemma 3.3.4. *Let $s, t \in \mathbb{R}$. We have*

$$\mathrm{Cov}\left(\mathcal{P}_m(t), \mathcal{P}_m(s)\right) = \sum_{1 \leq i,j \leq 2} \mathrm{Cov}(\mathcal{P}_m^{(i)}(t), \mathcal{P}_m^{(j)}(s)), \tag{3.6}$$

with

$$\mathrm{Cov}\left(\mathcal{P}_m^{(1)}(t), \mathcal{P}_m^{(1)}(s)\right) = \sum_{x_2=(1-m)}^{m-1} \sum_{x_1=(2-m)}^{m-2} (m - |x_2|)\,(m - 1 - |x_1|)\,\mathrm{Cov}\left(f_t^{(1)}(0), f_s^{(1)}(x)\right),$$

$$\mathrm{Cov}\left(\mathcal{P}_m^{(2)}(t), \mathcal{P}_m^{(2)}(s)\right) = \sum_{x_1=(1-m)}^{m-1} \sum_{x_2=(2-m)}^{m-2} (m - |x_1|)\,(m - 1 - |x_2|)\,\mathrm{Cov}\left(f_t^{(2)}(0), f_s^{(2)}(x)\right),$$

and finally,

$$\mathrm{Cov}\left(\mathcal{P}_m^{(1)}(t), \mathcal{P}_m^{(2)}(s)\right) \\ = \sum_{x_1=2-m}^{m-1} \sum_{x_2=1-m}^{m-2} (m - |x_1| - \mathbb{1}_{x_1 \leq 0})\,(m - |x_2| - \mathbb{1}_{x_2 \geq 0})\,\mathrm{Cov}\left(f_t^{(1)}(0), f_s^{(2)}(x)\right).$$

The above lemma shows that getting the value of the oriented perimeter covariance requires the computation of all the elements $\mathrm{Cov}\left(f_t^{(i)}(0), f_s^{(j)}(x)\right)$, $i, j \in \{1, 2\}$. Any of such elements has a two-, three- or four-cells structure, depending on the cardinality of the set $\{0, e_i, x, x + e_j\}$. Figure 3.6 shows the five types of configurations depending on the orientations i, j and the position of x on the grid. Note that these configurations are generic ones. Indeed any possible configuration can be reduced to one of them by applying a single symmetry and/or a single translation. For this reason, in Lemma 3.3.6 below we focus our attention only on three typical configurations.

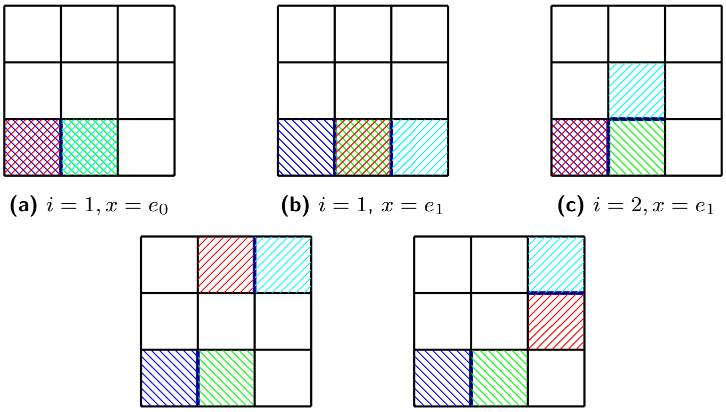

(a) $i = 1, x = e_0$ **(b)** $i = 1,\ x = e_1$ **(c)** $i = 2, x = e_1$

(d) $i = 1, x = e_1 + 2e_2$ **(e)** $i = 2, x = 2e_1 + e_2$

Figure 3.6 – Illustration of the two-cells (case (a)), three-cells (case (b)-(c)) and four-cells (case (d)-(e)) configurations involved in the computation of $\mathrm{Cov}\left(f_t^{(1)}(0), f_s^{(i)}(x)\right)$.

We now state a classical result that validates the fact that, under a mild assumption, the computation of previous sums in Lemma 3.3.4 breaks down as 2-cells, 3-cells and 4-cells contributions, where the involved Gaussian vector is non-degenerate whatever the configuration. For a self-contained purpose, we give a proof of the next lemma in Appendix3.A2.

Lemma 3.3.5. *Let* $n \in \mathbb{Z}^+, n > 0$ *and* $(X_x)_{x\in\mathbb{Z}^2}$ *be a stationary Gaussian random field and* ρ *its covariance function. Let us assume that* ρ *admits a spectral density. Then, if* $x_1, \dots, x_n$ *are* n *distinct points in* $\mathbf{Z}^2$*, the covariance matrix* Σ_n *of the Gaussian vector* $(X_{x_1}, \dots, X_{x_n})$*, is invertible.*

In order to compute $\mathbb{E}\left(f_t^{(1)}(0)\, f_s^{(i)}(x)\right)$, and recalling (3.3) when $|\rho(e_i)| \neq 1$, we introduce the following independent Gaussian variables,

$$\Delta_x^{(i)} := X_{x+e_i} - X_x \quad \text{and} \quad S_x^{(i)} := X_{x+e_i} + X_x. \tag{3.7}$$

Note that the covariance matrix of $(\Delta_0^{(1)}, S_0^{(1)}, \Delta_x^{(i)}, S_x^{(i)})$ has the same rank as the covariance matrix of $(X_0, X_{e_1}, X_x, X_{x+e_i})$ since the former Gaussian vector is obtained from the latter through an invertible linear transformation. Moreover, if ρ corresponds to a spectral measure that has a density then, using Lemma 3.3.5, we can state that the rank of the covariance matrix of $(X_0, X_{e_1}, X_x, X_{x+e_i})$ is equal to the cardinality of the set $\{0, e_1, x, x+e_i\}$.

Next lemma summarizes the way to compute $\mathbb{E}\left(f_t^{(1)}(0)\, f_s^{(i)}(x)\right)$ depending on the number of cells that are concerned.

Lemma 3.3.6. *With the notation* (3.7),

- *if card*$\{0, e_1, x, x+e_i\} = 4$,

$$\mathbb{E}\left(f_t^{(1)}(0)\, f_s^{(i)}(x)\right) = \mathbb{E}\left(\mathbb{1}_{\left\{|2t - S_0^{(1)}| \le |\Delta_0^{(1)}|\right\}} \mathbb{1}_{\left\{|2s - S_x^{(i)}| \le |\Delta_x^{(i)}|\right\}}\right);$$

- *if card*$\{0, e_1, x, x+e_i\} = 3$ *with* $x = e_1$ *and* $i = 1$ *or 2,*

$$\mathbb{E}\left(f_t^{(1)}(0)\, f_s^{(i)}(e_1)\right) = \mathbb{E}\left(\mathbb{1}_{\left\{|2t - S_0^{(1)}| \le |\Delta_0^{(1)}|\right\}} \mathbb{1}_{\left\{|2s - (S_0^{(1)} + \Delta_0^{(1)} + \Delta_{e_1}^{(i)})| \le |\Delta_{e_1}^{(i)}|\right\}}\right);$$

- *if card*$\{0, e_1, x, x+e_i\} = 2$ *with* $x = 0$ *and* $i = 1$,

$$\mathbb{E}\left(f_t^{(1)}(0)\, f_s^{(1)}(0)\right) = \mathbb{E}\left(\mathbb{1}_{\left\{|2t - S_0^{(1)}| \le |\Delta_0^{(1)}|\right\}} \mathbb{1}_{\left\{|2s - S_0^{(1)}| \le |\Delta_0^{(1)}|\right\}}\right).$$

In Appendix 3.A1, we provide closed formulas for $\mathbb{E}\left(f_t^{(1)}(0)\, f_s^{(i)}(x)\right)$ in each of the three typical configurations that are mentioned in the above lemma (see Lemmas 3.A1.1, 3.A1.3 and 3.A1.2). Such formulas can be obtained via a classical Gaussian regression. We actually don't use this formalism and prefer to write the considered projections with explicit coefficients. In this way we will able to numerically approximate the theoretical covariance (see Section 3.4). These formulas also permit to exhibit an explicit upper bound for the covariance of the oriented perimeter as stated in the next lemma.

Lemma 3.3.7. *Let* $x \in \mathbb{Z}^2$ *such that the covariance matrix of the Gaussian vector* $(X_0, X_{e_1}, X_x, X_{x+e_i})$ *is invertible and let us define*

$$r(x) = \max\left(|\rho(x)|, |\rho(x+e_i)|, |\rho(x-e_1)|, |\rho(x+e_i-e_1)|\right).$$

Then, for any $s, t \in \mathbb{R}$*, there exists a constant* $C \in \mathbb{R}^+$ *that depends on* (s,t) *such that*

$$|\,Cov\left(f_t^{(1)}(0), f_s^{(i)}(x)\right)| \leq Cr(x).$$

The proof of Lemma 3.3.7 is postponed to Appendix.

3.3.3 Local pixel isotropy test using the oriented perimeters

In order to construct a local pixel isotropy test using the oriented perimeters of the binary image, we first establish a Central Limit Theorem (CLT) for the variables $(\mathcal{P}_m^{(i)}(t))_m$ as m goes to infinity. To do that, we add some assumptions on the covariance function ρ of the field X.

$$(\mathcal{A}1)\ \ \lim_{m\to\infty} m^{-2} \sum_{x,y\in\mathbb{G}_m} \rho(x-y+h) \text{ exists } \forall\, h \in \{0, e_i, e_j, e_i - e_j; 1 \leq i, j \leq 2\}.$$

$$(\mathcal{A}2)\ \ \lim_{m\to\infty} m^{-1} \sum_{k,l=0}^{m} \rho((k-l)e_i + \varepsilon e_j) \ \text{ exists } \ \forall\, \{i,j\} = \{1,2\} \text{ and } \varepsilon \in \{0,1\}.$$

$$(\mathcal{A}3)\ \ \lim_{m\to\infty} m^{-2} \sum_{x,y\in\mathbb{G}_m} \rho(x-y)^2 \text{ exists.}$$

Note that if $\sum_{x\in\mathbf{Z}^2} |\rho(x)| < \infty$ then it also fulfills the three Assumptions $(\mathcal{A}1)$, $(\mathcal{A}2)$ and $(\mathcal{A}3)$.

Theorem 3.3.8. *(Multi-directional multivariate CLT for r-thresholds). We consider that* $(X_x)_{x\in\mathbf{Z}^2}$ *is a stationary standard Gaussian field with a covariance function that satisfies* $(\mathcal{A}1)$, $(\mathcal{A}2)$ *and* $(\mathcal{A}3)$*. Let* r *be a positive integer and* $t_1, \cdots, t_r \in \mathbb{R}$*. Then,*

$$\frac{1}{m}\left(\begin{pmatrix} \mathcal{P}_m^{(1)}(t_1) \\ \vdots \\ \mathcal{P}_m^{(1)}(t_r) \\ \mathcal{P}_m^{(2)}(t_1) \\ \vdots \\ \mathcal{P}_m^{(2)}(t_r) \end{pmatrix} - \begin{pmatrix} \mathbb{E}(\mathcal{P}_m^{(1)}(t_1)) \\ \vdots \\ \mathbb{E}(\mathcal{P}_m^{(1)}(t_r)) \\ \mathbb{E}(\mathcal{P}_m^{(2)}(t_1)) \\ \vdots \\ \mathbb{E}(\mathcal{P}_m^{(2)}(t_r)) \end{pmatrix}\right) \xrightarrow[m\to\infty]{d} \mathcal{N}\left(0,\, \Sigma_{2r}^{\star}\right),$$

where $\xrightarrow{d}$ *stands for the convergence in distribution and* $\mathcal{N}\left(0,\, \Sigma_{2r}^{\star}\right)$ *for the* $2r$*-dimensional centered Gaussian distribution with covariance matrix* $\Sigma_{2r}^{\star}$ *given by*

$$\Sigma_{2r}^{\star}(l,i,k,j) := \lim_{m\to\infty} \operatorname{Cov}\left(\frac{1}{m}\mathcal{P}_m^{(i)}(t_l), \frac{1}{m}\mathcal{P}_m^{(j)}(t_k)\right), \tag{3.8}$$

for $i, j \in \{1,2\}$ *and* $k, l \in \{1, \ldots, r\}$*.*

The proof of Theorem 3.3.8 is postponed to Appendix. It is based on a convergence theorem formulated by Arcones Arcones (1994). The assumptions $(\mathcal{A}1)$, $(\mathcal{A}2)$ and $(\mathcal{A}3)$ are exactly the ones that are necessary in the cited theorem. They ensure the existence of a finite limit in (3.8) but no insurance is given concerning the non-degeneracy of the matrix $\Sigma_{2r}^{\star}$.

Let us mention that we could have used the formalism of Cayley graphs exposed in Reddy et al. (2018) to get our central limit theorem but it would have required a stronger assumption on the Gaussian field, namely an exponentially decaying covariance function, and no stronger conclusion on the non-degeneracy limit variance would have been obtained.

We are now in position to construct the promised local pixel isotropy test. As previously discussed, we now aim to build a test using the specific structure of the mean perimeter in the case of local pixel isotropy. Let us consider the null hypothesis

$$H_0 \quad : \quad \rho(e_1) = \rho(e_2).$$

Under H_0, we remark that $\mathbb{E}\left(\mathcal{P}_m^{(1)}(t)\right) = \mathbb{E}\left(\mathcal{P}_m^{(2)}(t)\right)$ for all t. Making use of Theorem 3.3.8 for the Δ-method, we first need to introduce the scaled perimeters defined as $\tilde{\mathcal{P}}_m^{(i)}(t) = \frac{1}{m(m-1)}\mathcal{P}_m^{(i)}(t)$ in such a way that we have now

$$m\left(\tilde{\mathcal{P}}_m^{(i)}(t_l) - h(t_l, \rho(e_i))\right)_{1\leq i\leq 2, 1\leq l\leq r} \xrightarrow[m\to\infty]{d} \mathcal{N}\left(0, \Sigma_{2r}^{\star}\right),$$

with $h(t,c)$ defined by (3.4) in Theorem 3.3.1. Since $\frac{\mathcal{P}_m^{(1)}(t)}{\mathcal{P}_m^{(2)}(t)} = \frac{\tilde{\mathcal{P}}_m^{(1)}(t)}{\tilde{\mathcal{P}}_m^{(2)}(t)}$ and $\frac{\mathbb{E}(\mathcal{P}_m^{(1)}(t))}{\mathbb{E}(\mathcal{P}_m^{(2)}(t))} = \frac{h(t,\rho(e_1))}{h(t,\rho(e_2))}$, we have the following Gaussian asymptotic result.

Proposition 3.3.9 (CLT for the ratio of oriented perimeters)**.** *Let $t \in \mathbb{R}$ and $\mathcal{P}_m^{(i)}(t)$ be the oriented perimeter over ith-direction ($i = 1, 2$) introduced in Definition 3.2.1. Under the same assumptions as in Theorem 3.3.8, it holds that,*

$$m\left(\frac{\mathcal{P}_m^{(1)}(t)}{\mathcal{P}_m^{(2)}(t)} - \frac{\mathbb{E}\left(\mathcal{P}_m^{(1)}(t)\right)}{\mathbb{E}\left(\mathcal{P}_m^{(2)}(t)\right)}\right) \xrightarrow[m\to\infty]{d} \mathcal{N}\left(0, \tilde{\sigma}^2(t)\right), \tag{3.9}$$

with $\tilde{\sigma}^2(t) = \frac{\sigma_{1,1}^{\star}(t)\mu_2(t)^2 - 2\mu_2(t)\mu_1(t)\sigma_{1,2}^{\star}(t) + \sigma_{2,2}^{\star}(t)\mu_1(t)^2}{\mu_2(t)^4}$, $\mu_i(t) = h(t, \rho(e_i))$ *as in* (3.4) *and* $\sigma_{i,j}^{\star}(t) = \Sigma_2^{\star}(1, i, 1, j)$ *as in* (3.8).
Furthermore, under H_0, it holds that

$$m\left(\frac{\mathcal{P}_m^{(1)}(t)}{\mathcal{P}_m^{(2)}(t)} - 1\right) \xrightarrow[m\to\infty]{d, H_0} \mathcal{N}\left(0, \tilde{\sigma}_{H_0}^2(t)\right), \tag{3.10}$$

with $\tilde{\sigma}_{H_0}^2(t) = \frac{\sigma_{1,1}^{\star}(t) + \sigma_{2,2}^{\star}(t) - 2\sigma_{1,2}^{\star}(t)}{\mu_2(t)^2}$.

Taking advantage of the last proposition, we base our pixel isotropy test on the following ratio,

$$R_m(t) = \frac{\mathcal{P}_m^{(1)}(t)}{\mathcal{P}_m^{(2)}(t)}.$$

Assuming that $\tilde{\sigma}^2(t) > 0$ and considering a consistent empirical estimator $\hat{\sigma}_m^2(t)$ of $\tilde{\sigma}^2(t)$, then, from Proposition 3.3.9, it holds that

$$\frac{m}{\sqrt{\hat{\sigma}_m^2(t)}}\left(R_m(t) - 1\right) \xrightarrow[m\to\infty]{d, H_0} \mathcal{N}\left(0, 1\right).$$

Take a confidence level $\alpha \in (0,1)$ and set $q_{1-\frac{\alpha}{2}}$ such that $\mathbb{P}\left(|\mathcal{N}(0,1)| \leq q_{1-\frac{\alpha}{2}}\right) = 1 - \frac{\alpha}{2}$. We define the accessible test $\hat{\phi}_m(t)$ with asymptotic level α as

$$\hat{\phi}_m(t) = \mathbb{1}_{\left\{\frac{m}{\sqrt{\hat{\sigma}_m^2(t)}}|R_m(t)-1| \geq q_{1-\frac{\alpha}{2}}\right\}}. \tag{3.11}$$

Let us now raise the consistency question of the proposed test statistic under the alternative hypothesis $H_1\ :\ \rho(e_1) \neq \rho(e_2)$. According to Corollary 3.3.3, if $\rho(e_1) \neq \rho(e_2)$ then $\mathbb{E}\left(\mathcal{P}_m^1(t)\right)/\mathbb{E}\left(\mathcal{P}_m^2(t)\right) \neq 1$, for all $t \in \mathbf{R}$. Hence, we have the following result.

Proposition 3.3.10 (Consistency of the proposed isotropy test)**.** *For all* $t \in \mathbf{R}$*,*

$$\mathbb{P}_{H_1}\left(\hat{\phi}_m(t) = 1\right) \to 1 \qquad as \qquad m \to \infty.$$

Theorem 3.3.8 insures the existence of the asymptotic covariance of the oriented perimeter but does not give any information regarding the expression of the covariance.

Since we have no guarantees of the positivity of $\tilde{\sigma}^2(t) > 0$ in Proposition 3.3.9, the chosen formalism in Lemma 3.3.6 allows us to numerically evaluate the theoretical closed formulas for $\mathbb{E}\left(f_t^{(1)}(0)\, f_s^{(i)}(x)\right)$, explicitly given in Lemmas 3.A1.1, 3.A1.3 and 3.A1.2. The crucial numerical approximation study presented in Section 3.4 below, allows us to explore the non-degeneracy of the obtained variances and the well-posedness property of our test procedure. Furthermore, using classical empirical methods, we compare our numerically evaluated theoretical second moments with their empirical counterparts.

3.4 Numerical studies

The model we use to illustrate the theoretical results is a parametric model that belongs to the class of affine Gaussian processes with a covariance function of compact support, commonly known as m-dependent field. The parameter m designates the range of dependence meaning that for $||x||_2 > m$, $\mathrm{Cov}\left(X_0, X_x\right) = 0$ and in particular $\mathrm{Cov}\left(f_t^{(1)}(0), f_s^{(i)}(x)\right) = 0$. This model falls within the framework of the Central Limit Theorem 3.3.8. The parametric nature proves to be advantageous in the analysis of the behavior of the test under the alternative hypothesis ($H1$). Let X be a stationary, isotropic centered Gaussian field with a spherical covariance function given by $\rho(x) = (1-3||x||_2/2C+(||x||_2^3/2C^3)\mathbb{1}_{\{||x||_2\leq C\}}, x \in \mathbb{R}^2$ (see Bulinski et al. (2012a)).

Let $\{Y(x; a, b, \theta); x \in \mathbb{R}^2\}$, be a random field equal in distribution to $\{X(Ax); x \in \mathbb{R}^2\}$ (see Cabaña (1987); Berzin (2021)), where

$$A := \begin{pmatrix} a & 0 \\ 0 & b \end{pmatrix} \begin{pmatrix} \cos(\theta) & \sin(\theta) \\ -\sin(\theta) & \cos(\theta) \end{pmatrix} \tag{3.12}$$

with $a, b \in \mathbb{R}^2$ and $\theta \in [0, \pi)$. The field Y is also Gaussian with covariance function given by $\rho_Y(x) = (1 - 3||Ax||_2/2C + (||Ax||_2)^3/2C^3)\mathbb{1}_{\{||Ax||_2\leq C\}}$. Note that $a \neq b$ if and only if Y is anisotropic. Initially, we chose to illustrate the computations of the statistics of the oriented perimeter, using this covariance structure with the values $\theta = 0$ and $a = 1$, then we consider different values for θ.

In this section, for the sake of readability, we will note MCINT the number of Monte-Carlo for the integral approximation of the closed formulas of the moments and n the number of Monte-Carlo sample generation for the empirical estimation of the mean and the variance.

Section 3.4.1 (*resp.* Section 3.4.2) is devoted to validate first (*resp.* second) moment theoretical results and in Section 3.4.3 we illustrate the finite sample performances of the proposed local pixel isotropy test. We recall that the sampling of the Gaussian fields were done using the Matlab function `stationary_Gaussian_process` (MATLAB (2021)).

3.4.1 Numerical studies of the expected oriented perimeter

We start our numerical studies with the first moment (see Figures 3.7 and 3.8). We compare the theoretical results obtained in Section 3.3.1 with the associated empirical counterparts.

Figure 3.7 is a plot of the value of $\mathbb{E}\left(f^{(2)}(t)\right)$ for $t \in [-3, 3]$, we compare the theoretical curve in Theorem 3.3.1 with the empirical one for different values of parameter b. Figure 3.8 shows the evolution of $\mathbb{E}\left(f_t^{(2)}(0)\right)$ in Theorem 3.3.1 as a function of $\rho(e_2)$, the empirical curve in Figures 3.7 and 3.8 is computed by simulating Gaussian vectors of dimension 2 with the proper covariance structure and computing the expectation of the indicator function directly. As b grows, $\rho(e_2)$ goes to 0, converging towards an independent framework, which increases the length of the perimeter in the direction e_2.

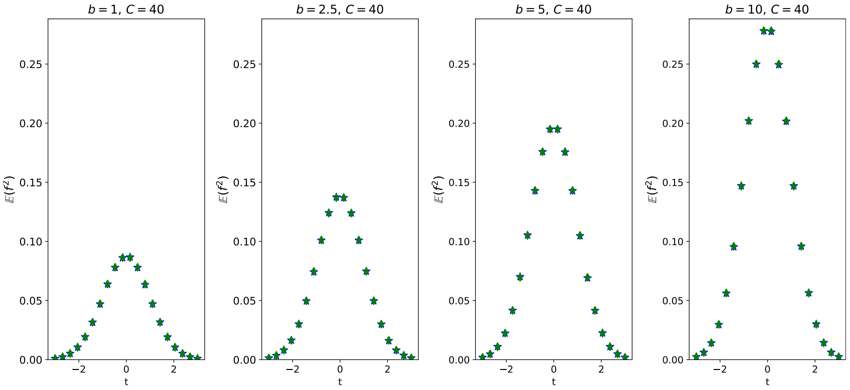

Figure 3.7 – We represent the values of $\mathbb{E}\left(f_t^{(2)}(0)\right)$ in Theorem 3.3.1 Formula (3.5) computed for different values of b as a function of the threshold t. The theoretical result is depicted using green diamonds and the empirical estimated values are in blue stars. The expectation in (3.5) is computed with $\text{MCINT} = 100000$, different values of $b = 1, 2.5, 5, 10$ and $C = 40$.

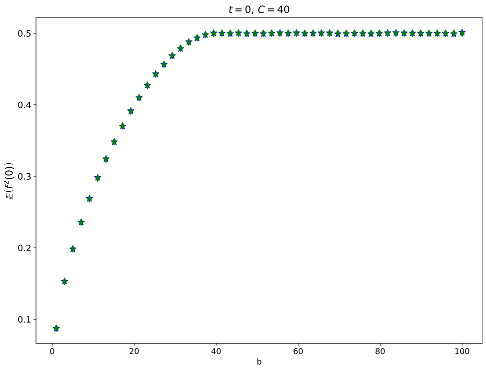

Figure 3.8 – We represent the theoretical values of $\mathbb{E}\left(f_0^{(2)}(0)\right)$ in Theorem 3.3.1 (green diamonds) for several values of parameter b and with $C = 40$. The expectation in Equation (3.5) is computed with $\text{MCINT} = 100000$.

3.4.2 Numerical studies of the oriented perimeter variances

As already remarked in Section 3.3.2, since we have no guarantees of the positivity of $\tilde{\sigma}^2(t)$ in Proposition 3.3.9, in this section, we numerically evaluate the theoretical closed formulas in Lemmas 3.A1.1, 3.A1.3 and 3.A1.2 for the second moment. Furthermore, we provide a comparison with their empirical counterparts.

To this aim, we consider two approaches for the empirical estimation of variance $\tilde{\sigma}^2(t)$ in Proposition 3.3.9.

The first approach relies on having n independent realizations of the random field $(X_x)_{x \in \mathbb{G}_m}$ (*i.e* n-images of size m). We start by fixing the threshold level t and computing the ratio $(R_{m,i}(t))_{i \leq n}$, for all n images. Then we consider the classical empirical estimator of the variance denoted here $\hat{\sigma}^{(1)}_{n,m}(t)$. In the following we will refer to this method as *the Monte Carlo* method.

The second considered method is inspired by Di Bernardino and Duval (2020) and is referred to as the *sub-window* method. It consists in dividing the observation window S in $M_m \in \mathbb{N}$ patches, computing the ratio on each individual patch and computing the empirical variance, denoted here $\hat{\sigma}^{(2)}_{M_m,m}(t)$. To establish the consistency of this second estimator, we compute it on domains that are infinitely distant, mimicking the classical context of *i.i.d.* random variables described above (see Di Bernardino and Duval (2020), Section 3.1.1).

In Figure 3.9 we consider the same Gaussian covariance model as in (3.12) for angle $\theta = 0$, $C = 40$ and $b = 1$. We display the values of the empirical variances of the ratio of the oriented perimeter $\hat{\sigma}^{(1)}_{n,m}(t)$ (blue stars) and $\hat{\sigma}^{(2)}_{M_m,m}(t)$ (red crosses) versus the theoretical numerically approximated values (green diamonds) obtained in Proposition 3.3.9, Equation (3.10).

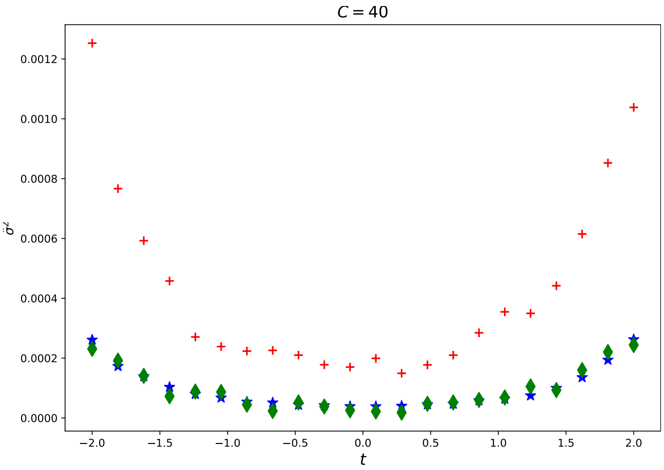

Figure 3.9 – Variances of the ratio of the oriented perimeter for the Gaussian covariance model in (3.12) with angle $\theta = 0$, $C = 40$ and $b = 1$. We display the values of estimators $\hat{\sigma}^{(1)}_{n,m}(t)$ (blue stars) $\hat{\sigma}^{(2)}_{M_m,m}(t)$ (red crosses) versus the theoretical associated values (green diamonds) by using Equation (3.10) with MCInt $= 100000$. To compute $\hat{\sigma}^{(1)}_{n,m}(t)$ we use a Monte Carlo $n = 2000$ images of size $m = 512$ and for $\hat{\sigma}^{(2)}_{M_m,m}(t)$, we used an image of size $m = 4800$ and the size of patches $M_m = 240$.

Figure 3.10 represents the numerically approximated theoretical variances (both panels, green diamonds) of the perimeter $\mathrm{Var}\left(\frac{1}{m}\mathcal{P}_m(t)\right)$ in Equation (3.6) for serval levels t and for different values of C. We consider MCInt $= 100000$. Recall that C is the length of the compact support of the covariance function ρ (*i.e.*, the bigger the value of C the stronger the dependence in the field). We observe in Figure 3.10 that the second moment of the perimeter is an increasing function of C and that the variance is maximal for the values $t = -1$ and $t = 1$ and reaches a local pixel minimum on $t = 0$.

Furthermore, in Figure 3.10 we display empirical variances computed using the Monte Carlo method $\hat{\sigma}^{(1)}_{n,m}(t)$ (blue stars in both panels) and sub-window method $\hat{\sigma}^{(2)}_{M_m,m}(t)$ (red crosses in right panel).

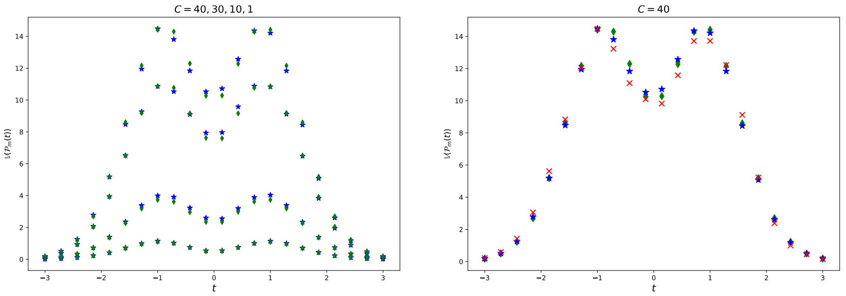

Figure 3.10 – In both panels, we represent the theoretical values of Var$\left(\frac{1}{m}\mathcal{P}_m(t)\right)$, $m = 512$ from Equation (3.6) in green diamonds with $\text{MC}\textsc{Int}= 100000$. In both panels, we display the empirical variance values $\hat{\sigma}^{(1)}_{n,m}(t)$ in blue stars with $n = 2000$. In the left panel we set $b = 1$ and from top to bottom $C = 40, 30, 10, 1$. In the right panel, we consider $b = 1$ and $C = 40$ and we add the estimation of the variance by using the sub-window method $\hat{\sigma}^{(2)}_{M_m,m}(t)$ in red crosses, with the image of size $m = 4800$ and the size of patches $M_m = 240$.

3.4.3 Numerical studies of local pixel isotropy test

To illustrate the finite sample behavior of our local pixel isotropy test, we choose to strategies.

i) Computing the empirical probability on n samples, $\hat{\mathbb{P}}_{H_0}(\hat{\phi}_m(t) = 1)$, with $i = 1, \ldots, n$ and $\hat{\phi}_{m,i}(t) = \mathbb{1}_{\{m/\sqrt{\hat{\sigma}^2_m(t)}|R_{m,i}(t)-1| \geq q_{1-\frac{\alpha}{2}}\}}$ with significant level $\alpha = 0.05$ (see Equation (3.11)), where the ratio $R_{m,i}$ is empirically evaluated generated sampels.

ii) Computing the $p-$value

$$\hat{p}_{\text{value}} = \frac{1}{n}\sum_{i=1}^{n} 2\mathbb{P}\left(\mathcal{N}(0,1) \geq |z_i|\right) \text{ with } z_i = (R_{m,i}(t) - 1)/\sqrt{\hat{\sigma}^2_m(t)}. \tag{3.13}$$

The variance $\hat{\sigma}^2_m(t)$ in items *i)* and *ii)* above is estimated via the Monte Carlo method $\hat{\sigma}^{(1)}_{n,m}(t)$ in Figure 3.11 and via the sub-window $\hat{\sigma}^{(2)}_{M_m,m}(t)$ in Figure 3.13.

for H_0 and the p_{value} for H_1 (see Figure 3.11 and Figure 3.13) for $b = 1$ and $b = 1.5$ and for $C = 40$ and $C = 20$.

In Figure 3.11, notice that under H_0 (*i.e.,* $b = 1$, first and second panels), the values of $\hat{\mathbb{P}}_{H_0}(\hat{\phi}_m(t) = 1)$ range from 0.04 and 0.06 and under H_1 (for instance for $b = 1.5$, third and fourth panels) the average value of the p_{value} is $< 10^{-4}$. We also explore the behavior of the test in a more constrained setting (less image data for the Monte Carlo method and an image of smaller size for the sub-window method). The small size of the patch forces us to restrain the study to threshold levels that are in the neighborhood of 0. That would ensure that one can find observations of the excursion set. Notice that the level $t = 0$ is the global maximum of the expected oriented perimeter (see Figure 3.7) and a local pixel minimum of the variance (see Figure 3.10), which makes it the optimal level to consider for inference purposes.

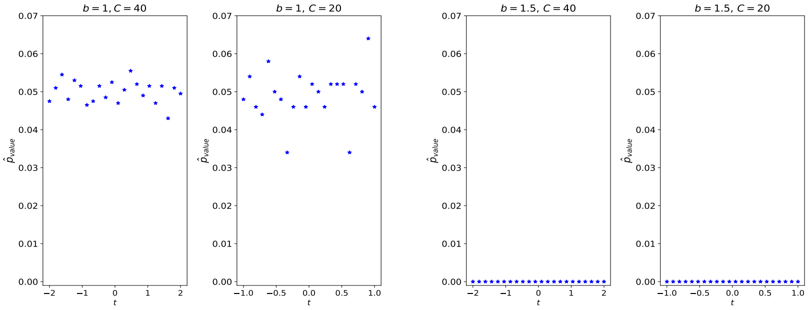

(a) Under H_0 : $\mathbb{P}_{H_0}(\hat{\phi}_m(t) = 1)$ **(b)** Under H_1 : $\hat{p}_{\text{value}}$

Figure 3.11 – We represent the value of $\mathbb{P}_{H_0}(\hat{\phi}_m(t) = 1)$, (panel (a)) and the $\hat{p}_{\text{value}} = \frac{1}{n}\sum_{i=1}^{n} 2\mathbb{P}\left(\mathcal{N}(0,1) \geq |z_i|\right)$ with $z_i = (R_{m,i}(t) - 1)/\sqrt{\hat{\sigma}^{(1)}_{n,m}(t)}$ (panel (b)). The variance $\hat{\sigma}^{(1)}_{n,m}(t)$ is computed using the Monte Carlo estimator of the variance by considering for the first and third image starting from the left $n = 2000$ images of size $m = 512$ and $C = 40$ and $t \in [-2, 2]$. For the second and fourth we consider $n = 500$ images of size $m = 512$, $C = 20$ and $t \in [-1, 1]$, $b = 1$ for H_0 and $b = 1.5$ for H_1.

In Figure 3.12, we explore the robustness of our local pixel isotropy test with respect to the choice of angle θ in the considered Gaussian covariance model in (3.12). The results are similar to those presented in Figure 3.11. These results can be compared with those in Figure 3.11 (third anf fourth panels).

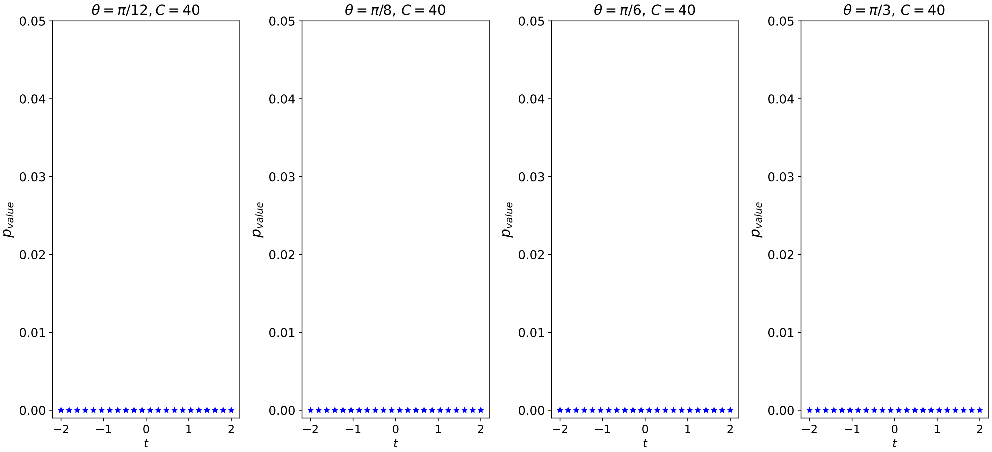

Figure 3.12 – We represent the value of $\hat{p}_{\text{value}} = \frac{1}{n}\sum_{i=1}^{n} 2\mathbb{P}\left(\mathcal{N}(0,1) \geq |z_i|\right)$ with $z_i = \frac{R_{m,i}(t)-1}{\sqrt{\hat{\sigma}^{(1)}_{n,m}(t)}}$. The estimation of the variance is obtained via the Monte Carlo method (*i.e.* $\hat{\sigma}^{(1)}_{n,m}(t)$) by considering $n = 2000$ images of size $m = 512$, for $b = 1.5$, $C = 40$ and different values of the angle $\theta = \pi/12, \pi/8, \pi/6, \pi/3$.

In Table 3.1 we present the $\hat{p}_{\text{value}}$ of the test computed using the Monte Carlo estimator of the variance ($i.e.$ $\hat{\sigma}^{(1)}_{n,m}(t)$) by considering $n = 2000$ images of size $m = 512$, for critical values of $b = 1.1$ and $b = 1.2$, $C = 40$ and several levels in $[-2, 2]$.

t b	-2	-1	-0.5	0	0.2	0.5	1	2
1.1	0.04	$< 10^{-4}$	$< 10^{-4}$	$< 10^{-4}$	$< 10^{-4}$	$< 10^{-4}$	$< 10^{-4}$	0.04
1.2	0.0001	$< 10^{-4}$	$< 10^{-4}$	$< 10^{-4}$	$< 10^{-4}$	$< 10^{-4}$	$< 10^{-4}$	0.0002

Table 3.1 – Obtained $\hat{p}_{\text{value}}$ of the proposed test computed using the Monte Carlo estimator of the variance by considering $n = 2000$ images of size $m = 512$.

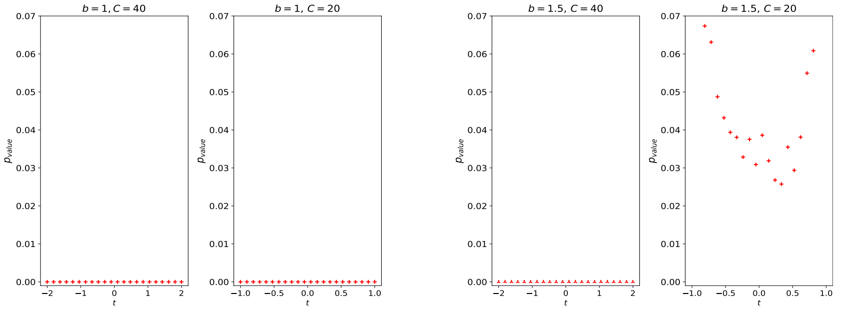

(a) Under H_0 : $\mathbb{P}_{H_0}(\hat{\phi}_m(t) = 1)$ **(b)** Under H_1 : $\hat{p}_{\text{value}}$

Figure 3.13 – We represent the value of $\mathbb{P}_{H_0}(\hat{\phi}_m(t) = 1)$, (panel (a)) and the $\hat{p}_{\text{value}} = \frac{1}{n}\sum_{i=1}^{n} 2\,\mathbb{P}\left(\mathcal{N}(0,1) \geq |z_i|\right)$ with $z_i = (R_{m,i}(t) - 1)/\sqrt{\hat{\sigma}^{(1)}_{n,m}(t)}$ (panel (b)). The variance $\hat{\sigma}^{(2)}_{M_m,m}(t)$ is computed using the sub-window method by considering for the first and third image starting from the left one single image of size $m = 4800$ and $M_m = 240$ for $C = 40$ and $t \in [-2, 2]$. Finally, for the second and fourth, we consider $m = 1024$ and $M_m = 32$ for $C = 20$ and $t \in [-1, 1]$, $b = 1$ for H_0 and $b = 1.5$ for H_1. For the panel (a) we considered a Monte Carlo $n = 100$.

3.5 Comparative study

We now proceed to a comparative study with Guan et al. (2004). This purely nonparametric method is based on the estimation of the semivariogram γ of the random field X, (*i.e* $\gamma(h) = \mathrm{Var}\,(X_{s+h} - X_s)$, for $h, s \in \mathbb{R}^2$). The main idea is that under the isotropy hypothesis the values of γ at any two spatial lags h_1 and h_2 that have the same norm are equal, regardless of the direction of the lags.

The isotropy test in Guan et al. (2004) involves the estimation of the semivariogram, γ, on a finite set of chosen lags, and then establishing a Central Limit Theorem when the domain increases and under moment and mixing conditions on the random field. A p_{value} can be obtained from an asymptotic χ^2 distribution. The simulation for Guan et al. (2004) are provided using the function `GuanTestGrid` from the `R package spTest` (see Weller (2018)). Since this method is based on the estimation of the complete covariance matrix, it implies a high computational cost. For this reason the considered simulation study is limited to $m = 24$ size images.

In Figure 3.14 (left panel) we draw a realisation of the considered Gaussian random fields with exponential covariance for $m = 24$ size image. We also represented two excursion sets (Figure 3.14, center and right panels). For the sake of fairness, we chose to apply the perimeter based isotropy test for two threshold levels $t = 0$ and $t = 1$. The threshold level $t = 0$ is one that maximizes the mean and minimizes the variance of the perimeter (see Figure 3.7 and Figure 3.10), which makes it the perfect candidate for our inference procedure (Figure 3.15, left panel). However, since we do not necessarily have access to the value of the mean of the field, therefore, we also present the result of the test for another threshold level, $t = 1$ (Figure 3.15, right panel).

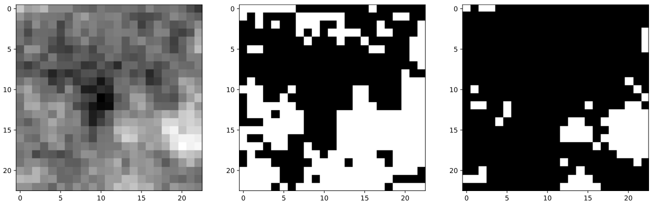

Figure 3.14 – A realisation of a Gaussian random fields with covariance $\rho(x) = e^{-\kappa||x||^2}$ and $m = 24$ and the associated thresholded image for $t = 0$ (center panel) and $t = 1$ (right panel).

In Figure 3.15 we represent the boxplot of the distribution of the p_{value} for both methods. For the Guan et al. (2004)'s method we display the approximate finite-sample adjusted p_{value} computed by using the sub-blocks created by the moving windows (see Guan et al. (2004), Section 3.3 for details). The p_{value} of our perimeter method are computed by using the Monte Carlo estimator of the variance, i.e., $\hat{\sigma}^{(1)}(t)$.

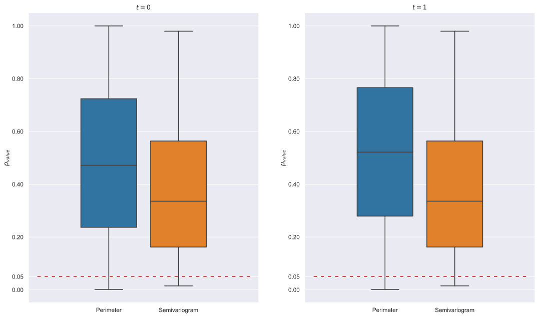

Figure 3.15 – We represent the two boxplots of the distribution of the p_{value} computed using the perimeter based method (blue color) and the approximate finite-sample adjusted p_{value} (orange color). The p_{value} of our perimeter method are computed by using $\hat{\sigma}^{(1)}(t)$ to estimate the variance and fixing the threshold value to $t = 0$ (left panel) and $t = 1$ (right panel). The computations for both methods are provided with Monte Carlo $= 300$ of $m = 24$ size images.

ON THE COMPUTATIONAL COMPLEXITY OF TWO METHODS In practice, the core of our method is based on just counting the number of transitions between black and white pixels in the thresholded image. For this feature, our method is highly amenable to the treatment of large data-sets. Conversely, the Guan et al. (2004)'s method requires the estimation of the semivariogram function and the covariance function values of the random field, besides to establish the statistic test it is required to proceed to a matrix inversion. This approach is significantly more computationally demanding and, thus, less suitable for the analysis of high-resolution images.

3.6 Local pixel isotropy test on bone X-rays

Description of the considered bone X-rays. The studied X-ray images were acquired at INSERM U658 (Orleans, France) using a standardized procedure Lespessailles et al. (2007, 2008). They were obtained on the calcaneus (a heel bone) with a direct digital X-ray prototype (BMA$^{\mathrm{TM}}$, D3A Medical Systems, Orleans, France) with focal distance 1.15 m and X-ray parameters 55 kV and 20 mAs. The high-resolution digital detector integrated into the device prototype had a 50 μm pixel size, providing a spatial resolution of 8 line pairs per millimeter at 10% modulation transfer function. For each subject, the software device selected a region of interest (ROI) of constant size 400×400 pixels corresponding at a same position using three predefined anatomical landmarks localized by the operator (see Figure 3.16). The database contains radiographs of 211 post menopausal women, it was previously studied in Biermé et al. (2009).

We first applied a pre-processing step in order to get stationary images. This step is performed by subtracting the trend which is represented by a plane obtained via a mean-square linear regression. Furthermore, to avoid boundaries issues, we decided to crop from a 400×400 image to a 380×380 image. It is also necessary to standardize the images to be in the centered and unit variance framework, considered in this work.

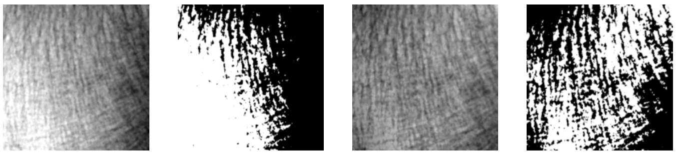

Figure 3.16 – Example of images before (first panel) and after (third panel) the stationary procedure and their excursion sets at quantile level $\alpha = 0.5$ (second and four panels, respectively).

A quick word regarding the choice of the threshold. To insure that the images of two excursion sets can be compared, we chose to select the threshold as quantile levels of the image. This method imposes a geometrical constraint on the choice of the threshold level, which guaranties the comparability of the excursion sets. Thus for an image X, for $\alpha \in (0, 1)$ the considered threshold is $t_\alpha = \hat{F}_X^{-1}(\alpha)$ with $\hat{F}_X$ the empirical cumulative distribution function of the image X. After this pre-processing, Figure 3.2 suggested the existence of two clusters in regard to the ratio of the two perimeters. Indeed, we observe a cluster of points for which the ratio $\mathcal{P}_1(t_\alpha)/\mathcal{P}_2(t_\alpha) < 1$. This means that the corresponding images are mis-oriented. Thus, before proceeding further with the local pixel isotropy test, we apply a second pre-processing step: a $\pi/2$-rotation to these specific images. The new obtained boxplots are gathered in Figure 3.17.

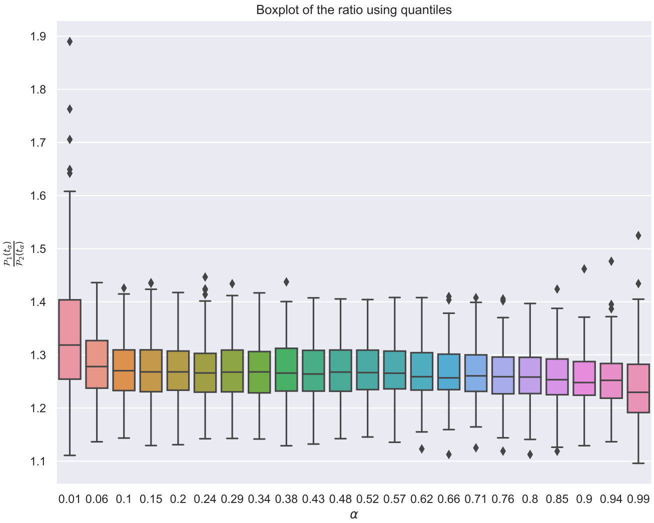

Figure 3.17 – For $\alpha \in [0.01, 0.99]$, we represent the boxplot of the ratios $(R_{m,i}(t_\alpha))_{i\leq 211}$, with $R_{m,i}(t_\alpha) = \mathcal{P}^{(1)}_{m,i}(t_\alpha)/\mathcal{P}^{(2)}_{m,i}(t_\alpha)$ at t_α level with $t_\alpha = \hat{F}_X^{-1}(\alpha)$, for bone X-rays after pre-processing stationary step and rotation, when necessary.

Applying the local pixel isotropy test.

We can now proceed to the local pixel isotropy test. To this aim, we compute $p_{\text{value},i}(t_\alpha) = 2\mathbb{P}\left(\mathcal{N}(0,1) > |R_i(t_\alpha) - 1)| / \hat{\sigma}^{(1)}_{211,380}(t_\alpha)\right)$, for each image X_i with the Monte Carlo estimated variance $\hat{\sigma}^{(1)}_{211,380}(t_\alpha)$ (see Section 3.4.2) and then we represent $\hat{p}_{\text{value},211} = \frac{1}{211}\sum_{i=1}^{211} p_{\text{value},i}(t_\alpha)$ in Figure 3.18.

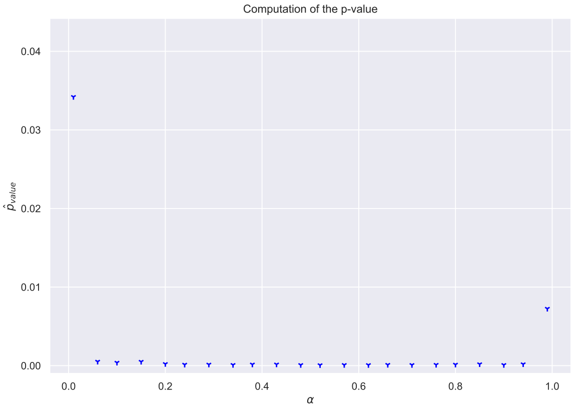

Figure 3.18 – For $\alpha \in [0.01, 0.99]$, we represent the p_{value} of the test computed for different levels t_α for stationary thresholded and eventually rotated images of bone X-rays.

As expected, the result of the hypothesis test $\hat{p}_{\text{value}} < 0.05$ indicates that the data exhibit anisotropy, this leads us to reject the hypothesis of pixel isotropy. Furthermore, when analyzing Figure 3.17, the distribution of the ratio $(R_{m,i}(t))_{i\leq n}$ seems to be invariant in regards to the threshold level, as already noticed in Remark 5. This suggests that the field is highly dependent.

In order to corroborate this intuition, we estimate $\rho(e_i)$ by applying Proposition 3.3.2 and using the total variation of the image. Figure 3.19 confirms the highly local pixel dependence behavior of the considered images, *i.e* $\hat{\rho}_i(e_j) \approx 1$ for $j = 1, 2$ and $1 \leq i \leq 211$.

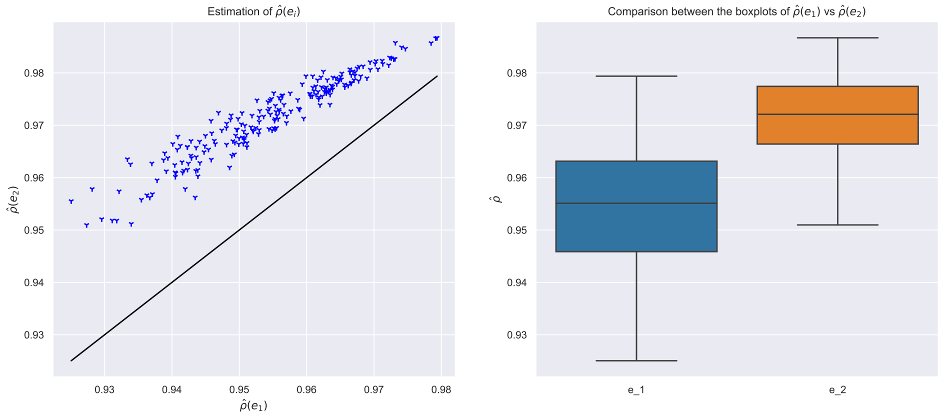

Figure 3.19 – In the left panel, we represent the couple $(\hat{\rho}_i(e_1), \hat{\rho}_i(e_2))$ for each image X_i. On the right panel, we represent the boxplot of $(\hat{\rho}_i(e_1))_{i \leq 211}$ (blue) and $(\hat{\rho}_i(e_2))_{i \leq 211}$ (orange).

3.7 Conclusion and discussion

In this paper, we have introduced a novel statistical technique for evaluating the local pixel isotropy property of a Gaussian random field. By utilizing the oriented perimeter of the excursion set, we were able to build a consistent test only based on this sparse observation. We also successfully applied the test to real world data to test the anisotropic nature of bone texture. As we have seen above, the proposed test does not require any prior knowledge of the field, however, it better performs when the selected threshold is close to the mean value of the field and worse for extreme levels t.

Notice that in this work, that we only test a form of local pixel isotropy, with preferential axis (e_1, e_2). There exist anisotropic models where $\rho(e_1) = \rho(e_2)$. This is the case of our Gaussian affine model when considering $\theta = \pi/4$. In Figure 3.20 we see that the proposed test accepts the H_0 hypothesis, that is verified by the model.

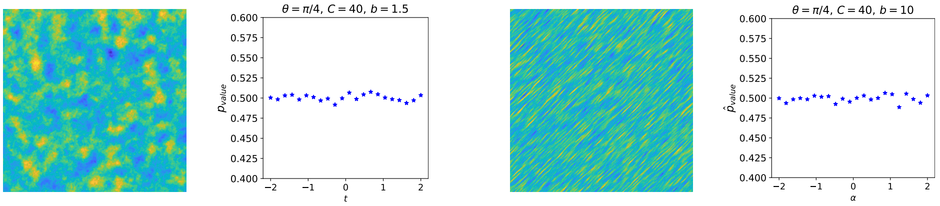

Figure 3.20 – We represent two generations of an affine Gaussian random fields with covariance of a compact support $\rho(x) = (1 - 3||Ax||_2/2C + (||Ax||_2)^3/2C^3)\mathbb{1}_{||Ax||_2 < C}$, as in (3.12) with $m = 512$, $\theta = \pi/4$, $C = 40$ and $b = 1.5$ (first panel) and $b = 10$ (third panel) respectively. We also display $\hat{p}_{\text{value}} = \frac{1}{n}\sum_{i=1}^{n} 2\mathbb{P}\left(\mathcal{N}(0,1) \geq |z_n|\right)$ with $z_i = (R_{m,i}(t) - 1)/\sqrt{\hat{\sigma}^{(1)}_{n,m}(t)}$ in blue color computed for a Monte Carlo $n = 2000$, for $b = 1.5$ (second panel) and $b = 10$ (fourth panel).

However, one could adapt results in the present paper by applying a rotation over a direction to the image, and then implement the test to verify if the field is anisotropic in

regard to that particular direction.
Another potential improvement, would be to study the behavior of the ratio between the first and second moments of the oriented perimeter in a dense tiling framework. If an equivalence between the two is established, it would short cut the inference of the variance, using the first moment instead, and hopefully increasing the performance of the test for extreme thresholds. Finally, we obtained a closed form for both the first and second moments which renders possible a thorough study of the infill framework (*i.e.* $\rho(e_i) \to 1$), which yields a shift from the discrete setting to the continuous one.

3.A1 Lemmas concerning the two-, three- and four-cells configurations

Lemma 3.A1.1 (Computation of the four-cells contribution)**.** *Let* $i = 1$ *or* 2*, and let* $x \in \mathbb{Z}^2$ *such that the covariance matrix of the Gaussian vector* $(X_0, X_{e_1}, X_x, X_{x+e_i})$ *is invertible. Let us define the following coefficients,*

$$\Delta\rho(x) = \rho(x - e_1) - \rho(x) \text{ and } S\rho(x) = \rho(x - e_1) + \rho(x).$$

Then, $\sigma_1^{(-)} > 0$*,* $\sigma_1^{(+)} > 0$*,* $\pi_W^{(-,i)}(x) > 0$ *and* $\pi_Z^{(+,i)}(x) > 0$*, where we have introduced the following quantities,*

$$\left\{\begin{array}{lcl} \sigma_1^{(-)} & = & \sqrt{2(1-\rho(e_1))} \\ \sigma_1^{(+)} & = & \sqrt{2(1+\rho(e_1))} \end{array}\right.$$
$$\left\{\begin{array}{lcl} \pi_U^{(-,i)}(x) & = & \frac{1}{\sigma_1^{(-)}}\left(\Delta\rho(x+e_i) - \Delta\rho(x)\right) \\ \pi_V^{(-,i)}(x) & = & \frac{1}{\sigma_1^{(+)}}\left(S\rho(x+e_i) - S\rho(x)\right) \\ \pi_W^{(-,i)}(x) & = & \left(2(1-\rho(e_i)) - \pi_U^{(-,i)}(x)^2 - \pi_V^{(-,i)}(x)^2\right)^{1/2} \end{array}\right.$$
$$\left\{\begin{array}{lcl} \pi_U^{(+,i)}(x) & = & \frac{1}{\sigma_1^{(-)}}\left(\Delta\rho(x) + \Delta\rho(x+e_i)\right) \\ \pi_V^{(+,i)}(x) & = & \frac{1}{\sigma_1^{(+)}}\left(S\rho(x) + S\rho(x+e_i)\right) \\ \pi_W^{(+,i)}(x) & = & \frac{-1}{\pi_W^{(-,i)}(x)}\left(\pi_U^{(-,i)}(x)\pi_U^{(+,i)}(x) + \pi_V^{(-,i)}(x)\pi_V^{(+,i)}(x)\right) \\ \pi_Z^{(+,i)}(x) & = & \left(2(1+\rho(e_i)) - \pi_U^{(+,i)}(x)^2 - \pi_V^{(+,i)}(x)^2 - \pi_W^{(+,i)}(x)^2\right)^{1/2}. \end{array}\right.$$

Moreover,

$$\begin{aligned} &\mathbb{E}\left(f_t^{(1)}(0) f_s^{(i)}(x)\right) \\ &= \mathbb{E}\Bigg(\mathbb{1}_{\left\{|2t - \sigma_1^{(+)}V| \le \sigma_1^{(-)}|U|\right\}} \qquad (3.14) \\ &\Big|\Phi_{\pi_Z^{(+,i)}(x)}\left(2s + \left(\pi_U^{(-,i)}(x) - \pi_U^{(+,i)}(x)\right)U + \left(\pi_V^{(-,i)}(x) - \pi_V^{(+,i)}(x)\right)V + \left(\pi_W^{(-,i)}(x) - \pi_W^{(+,i)}(x)\right)W\right) \\ &-\Phi_{\pi_Z^{(+,i)}(x)}\left(2s - \left(\pi_U^{(-,i)}(x) + \pi_U^{(+,i)}(x)\right)U - \left(\pi_V^{(-,i)}(x) + \pi_V^{(+,i)}(x)\right)V - \left(\pi_W^{(+,i)}(x) + \pi_W^{(-,i)}(x)\right)W\right)\Big|\Bigg) \end{aligned}$$

with $\Phi_{\pi_Z^{(+,i)}(x)}$ *the* $\mathcal{N}(0, (\pi_Z^{(+,i)}(x))^2)$*-cumulative distribution function and* $(U, V, W) \sim \mathcal{N}(0, I_3)$*.*

Proof. Recall that we have introduced $\Delta_x^{(i)}$ and $S_x^{(i)}$ in (3.7). The covariance matrix of the Gaussian vector $(\Delta_0^{(1)}, S_0^{(1)}, \Delta_x^{(i)}, S_x^{(i)})$ is equal to
$$\Sigma_i(x) = \begin{pmatrix} A_1 & B_i(x) \\ B_i^T(x) & A_i \end{pmatrix} \text{ with } A_i = \begin{pmatrix} 2(1-\rho(e_i)) & 0 \\ 0 & 2(1+\rho(e_i)) \end{pmatrix}$$

and $B_i(x) = \begin{pmatrix} \Delta\rho(x+e_i) - \Delta\rho(x) & \Delta\rho(x) + \Delta\rho(x+e_i) \\ S\rho(x+e_i) - S\rho(x) & S\rho(x) + S\rho(x+e_i) \end{pmatrix}$.

By assumption, $\Sigma_i(x)$ is invertible, thus, applying the Cholesky decomposition yields the existence of an invertible lower triangular matrix $L(x)$ such that $\Sigma_i(x) = L(x)L(x)^T$. The matrix $L(x)$ is given by

$$L(x) = \begin{pmatrix} \sigma_1^{(-)} & 0 & 0 & 0 \\ 0 & \sigma_1^{(+)} & 0 & 0 \\ \pi_U^{(-,i)}(x) & \pi_V^{(-,i)}(x) & \pi_W^{(-,i)}(x) & 0 \\ \pi_U^{(+,i)}(x) & \pi_V^{(+,i)}(x) & \pi_W^{(+,i)}(x) & \pi_Z^{(+,i)}(x) \end{pmatrix}$$

with the coefficients introduced in the statement of the lemma. Furthermore, $\det\left(L(x)\right) \neq 0$ implies that $\sigma_1^{(\pm)} \neq 0$, $\pi_W^{(-,i)}(x) \neq 0$ and $\pi_Z^{(+,i)}(x) \neq 0$ as stated in the quoted lemma. This decomposition allows us to write $\begin{pmatrix} \Delta_0^{(1)} \\ S_0^{(1)} \\ \Delta_x^{(i)} \\ S_x^{(i)} \end{pmatrix} = L(x) \begin{pmatrix} U \\ V \\ W \\ Z \end{pmatrix}$, with $(U,V,W,Z) \sim \mathcal{N}\left(0, I_4\right)$. Developing the indicator functions that appear in Lemma 3.3.6, we get the following expression

$$\begin{aligned} &\mathbb{E}\left(f_t^{(1)}(0) f_s^{(i)}(x)\right) \\ &= \mathbb{E}\left(\mathbb{1}_{\left\{|2t - S_0^{(1)}| \leq |\Delta_0^{(1)}|\right\}} \mathbb{1}_{\left\{|2s - S_x^{(i)}| \leq |\Delta_x^{(i)}|\right\}}\right) \\ &= \mathbb{E}\Bigg(\mathbb{1}_{\left\{|2t - S_0^{(1)}| \leq |\Delta_0^{(1)}|\right\}} \mathbb{1}_{\Big\{2s - \pi_U^{(+,i)}(x)U - \pi_V^{(+,i)}(x)V - \pi_W^{(+,i)}(x)W - |\Delta_x^{(i)}| \leq \pi_Z^{(+,i)}(x)Z} \\ &\qquad\qquad {}_{\leq 2s - \pi_U^{(+,i)}(x)U - \pi_V^{(+,i)}(x)V - \pi_W^{(+,i)}(x)W + |\Delta_x^{(i)}|\Big\}}\Bigg). \end{aligned}$$

The variable $\pi_Z^{(+,i)} Z \sim \mathcal{N}\left(0, \pi_Z^{(+,i)}(x)^2\right)$ and $\Phi_{\pi_Z^{(+,i)}(x)}$ being an increasing function, we get

$$\begin{aligned} &\mathbb{E}\left(f_t^{(1)}(0) f_s^{(i)}(x)\right) \\ &= \mathbb{E}\Bigg(\mathbb{1}_{\left\{|2t - \sigma_1^{(+)} V| \leq \sigma_1^{(-)} |U|\right\}} \\ &\Big|\Phi_{\pi_Z^{(+,i)}(x)}\left(2s - \pi_U^{(+,i)}(x)U - \pi_V^{(+,i)}(x)V - \pi_W^{(+,i)}(x)W + \Delta_x^{(i)}\right) \\ &-\Phi_{\pi_Z^{(+,i)}(x)}\left(2s - \pi_U^{(+,i)}(x)U - \pi_V^{(+,i)}(x)V - \pi_W^{(+,i)}(x)W - \Delta_x^{(i)}\right)\Big|\Bigg), \end{aligned}$$

which directly gives (3.14). □

Lemma 3.A1.2 (Computation of the three-cells contribution)**.** *Let $i = 1$ or 2 and let us assume that the covariance matrix of the Gaussian vector $(X_0, X_{e_1}, X_{e_1+e_i})$ is invertible. Then, considering the coefficients $\sigma_1^{(-)}$ $\sigma_1^{(+)}, \pi_U^{(-,i)}(e_1), \pi_V^{(-,i)}(e_1), \pi_W^{(-,i)}(e_1)$ that are defined in Lemma 3.A1.1, we have $\sigma_1^{(-)} > 0$, $\sigma_1^{(+)} > 0$, $\pi_W^{(-,i)}(e_1) > 0$, and*

$$\begin{aligned} &\mathbb{E}\left(f_t^{(1)}(0) f_s^{(i)}(e_1)\right) \\ &= \mathbb{E}\Bigg(\mathbb{1}_{\left\{|2t - \sigma_1^{(+)} V\big| \leq \big|\sigma_1^{(-)} U|\right\}} \mathbb{1}_{\left\{\sigma_1^{(-)} U + \sigma_1^{(+)} V \leq 2s\right\}} \end{aligned}$$

$$\begin{aligned}
&\left(1-\Phi_{\pi_W^{(-,i)}(e_1)}\left(s-\left(\frac{1}{2}\sigma_1^{(-)}+\pi_U^{(-,i)}(e_1)\right)U-\left(\frac{1}{2}\sigma_1^{(+)}+\pi_V^{(-,i)}(e_1)\right)V\right)\right)\right)\\
&+\mathbb{E}\Bigg(\mathbb{1}_{\left\{\left|2t-\sigma_1^{(+)}V\right|\leq\left|\sigma_1^{(-)}U\right|\right\}}\mathbb{1}_{\left\{\sigma_1^{(-)}U+\sigma_1^{(+)}V\geq 2s\right\}}\\
&\Phi_{\pi_W^{(-,i)}(e_1)}\left(s-\left(\frac{1}{2}\sigma_1^{(-)}+\pi_U^{(-,i)}(e_1)\right)U-\left(\frac{1}{2}\sigma_1^{(+)}+\pi_V^{(-,i)}(e_1)\right)V\right)\Bigg),
\end{aligned}\tag{3.15}$$

where Φ_α stands for the centered Gaussian distribution with variance α^2 and $(U,V)\sim\mathcal{N}(0,I_2)$.

Proof. Following a similar method as for the proof of Lemma 3.A1.1, let us consider the transformed vector $\left(\Delta_0^{(1)}, S_0^{(1)}, \Delta_{e_1}^{(i)}\right)$. Its covariance matrix is invertible by assumption and its Cholesky decomposition allows us to write $\begin{pmatrix}\Delta_0^{(1)}\\ S_0^{(1)}\\ \Delta_{e_1}^{(i)}\end{pmatrix} = K(e_1)\begin{pmatrix}U\\ V\\ W\end{pmatrix}$, with $(U,V,W)\sim\mathcal{N}(0,I_3)$ and

$$K(e_1)=\begin{pmatrix}\sigma_1^{(-)} & 0 & 0\\ 0 & \sigma_1^{(+)} & 0\\ \pi_U^{(-,i)}(e_1) & \pi_V^{(-,i)}(e_1) & \pi_W^{(-,i)}(e_1)\end{pmatrix}$$

Then, thanks to the three-cells case of Lemma 3.3.6, we have

$$\mathbb{E}\left(f_t^{(1)}(0)\,f_s^{(i)}(e_1)\right)=\mathbb{E}\left(\mathbb{1}_{\left\{|2t-S_0^{(1)}|\leq|\Delta_0^{(1)}|\right\}}\mathbb{1}_{\left\{|2s-(S_0^{(1)}+\Delta_0^{(1)}+\Delta_{e_1}^{(i)})|\leq|\Delta_{e_1}^{(i)}|\right\}}\right),$$

where we can use the vector (U,V,W) to write the first indicator function as

$$\mathbb{1}_{\left\{|2s-S_0^{(1)}|\leq|\Delta_0^{(1)}|\right\}}=\mathbb{1}_{\left\{|2s-\sigma_1^{(+)}V|\leq|\sigma_1^{(-)}U|\right\}},$$

and to split the second indicator function as

$$\begin{aligned}
\mathbb{1}_{\left\{|2s-S_x^{(i)}|\leq|\Delta_x^{(i)}|\right\}}=\;&\mathbb{1}_{\left\{\sigma_1^{(-)}U+\sigma_1^{(+)}V\leq 2s\right\}}\\
&\mathbb{1}_{\left\{\pi_W^{(-,i)}(e_1)W\geq\left(s-\left(\frac{1}{2}\sigma_1^{(-)}+\pi_U^{(-,i)}(e_1)\right)U-\left(\frac{1}{2}\sigma_1^{(+)}+\pi_V^{(-,i)}(e_1)\right)V\right)\right\}}\\
&+\mathbb{1}_{\left\{\sigma_1^{(-)}U+\sigma_1^{(+)}V\geq 2s\right\}}\\
&\mathbb{1}_{\left\{\pi_W^{(-,i)}(e_1)W\leq\left(s-\left(\frac{1}{2}\sigma_1^{(-)}+\pi_U^{(-,i)}(e_1)\right)U-\left(\frac{1}{2}\sigma_1^{(+)}+\pi_V^{(-,i)}(e_1)\right)V\right)\right\}}.
\end{aligned}$$

Putting everything together yields Equation (3.15). □

Figure 3.21 below is a numerical illustration of Equation (3.15) which validates the obtained theoretical result. The empirical curve in Figures 3.21 is computed by simulating Gaussian vectors of dimension 3 with the proper covariance structure and computing the expectation of the indicator function directly.

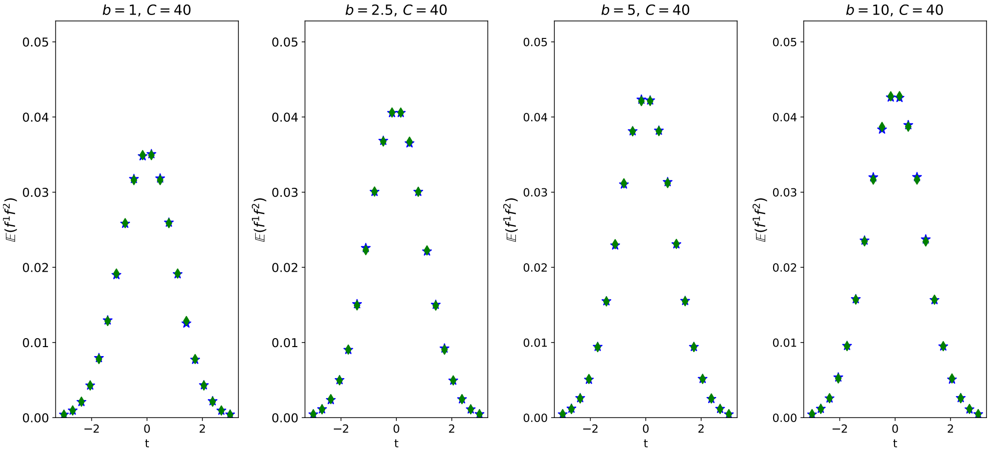

Figure 3.21 – In each panel, we represent the values of $\mathbb{E}\left(f_t^{(1)}(0)f_t^{(2)}(e_1)\right)$ computed using the same framework that was introduced in Section 3.4 for different values of b and $C = 40$. The value of the expectation in Equation (3.15) is represented in blue and the associated empirical values are in green. The computations are implemented with a $\mathrm{MCINT} = 100000$.

Lemma 3.A1.3 (Computation of the two cells contribution)**.** *Let* $Z \sim \mathcal{N}(0,1)$*. It holds that*

$$\mathbb{E}\left(f_t^{(1)}(0)f_s^{(1)}(0)\right) = \mathbb{E}\left(\left(\Phi\left(\frac{\sqrt{2}\max(t,s)+\sqrt{1-\rho(e_1)}|Z|}{\sqrt{1+\rho(e_1)}}\right) - \Phi\left(\frac{\sqrt{2}\min(t,s)-\sqrt{1-\rho(e_1)}|Z|}{\sqrt{1+\rho(e_1)}}\right)\right)\mathbb{1}_{\left\{|s-t|\le |Z|\sqrt{2(1-\rho(e_1))}\right\}}\right).$$

Proof. We apply the same strategy we use in the proof of Theorem 3.3.1. ☐

3.A2 Proofs

Proof of Theorem 3.3.1.
Considering formula (3.2) for $\mathcal{P}_m^{(i)}(t)$ and formula (3.3) for $f_t^{(i)}(x)$, and applying the stationarity hypothesis, one can write that,

$$\mathbb{E}\left(\mathcal{P}_m^{(i)}(t)\right) = m(m-1)\mathbb{E}\left(f_t^{(i)}(0)\right) = m(m-1)\mathbb{E}\left(\mathbb{1}_{\left\{\left|2t-S_0^{(i)}\right|\le\left|\Delta_0^{(i)}\right|\right\}}\right),$$

where $\Delta_0^{(i)} := X_{e_i} - X_0$ and $S_0^{(i)} := X_{e_i} + X_0$. The covariance matrix of the Gaussian vector $(\Delta_0^{(i)}, S_0^{(i)})$ is given by $\tilde{\Sigma}_i(0) = \begin{pmatrix} 2(1-\rho(e_i)) & 0 \\ 0 & 2(1+\rho(e_i)) \end{pmatrix}$, which directly implies that the two variables $\Delta_0^{(i)}$ and $S_0^{(i)}$ are independent. Hence, we can write

$$\Delta_0^{(i)} = \sqrt{2(1-\rho(e_i))}U \text{ and } S_0^{(i)} = \sqrt{2(1+\rho(e_i)}V \text{ with } (U,V) \sim \mathcal{N}(0, I_2).$$

If $\rho(e_i) \neq -1$, we get

$$\mathbb{E}\left(f_t^{(i)}(0)\right) = \mathbb{E}\left(\mathbb{1}_{\left\{\left|2t-S_0^{(i)}\right|\le\left|\Delta_0^{(i)}\right|\right\}}\right)$$

$$
\begin{aligned}
&= \mathbb{E}\left(\mathbb{1}_{\left\{\frac{2t-\sqrt{2(1-\rho(e_i))}|U|}{\sqrt{2(1+\rho(e_i))}}\le V\le\frac{2t+\sqrt{2(1-\rho(e_i))}|U|}{\sqrt{2(1+\rho(e_i))}}\right\}}\right)\\
&= \mathbb{E}\left(\Phi\left(\frac{2t+\sqrt{2(1-\rho(e_i))}|U|}{\sqrt{2(1+\rho(e_i))}}\right)-\Phi\left(\frac{2t-\sqrt{2(1-\rho(e_i))}|U|}{\sqrt{2(1+\rho(e_i))}}\right)\right)\\
&= h(t,\rho(e_i)),
\end{aligned}
$$

with function $h(t,\cdot)$ exactly as in (3.5).

We now consider the function $h_t := h(t,\cdot)$ defined on $(-1,1]$ through (3.5) as well as the intermediate function

$$
p_t(c) = \mathbb{E}\left(\Phi\left(\frac{2t+\sqrt{2(1-c)}|U|}{\sqrt{2(1+c)}}\right)\right).
$$

Using the symmetry properties of the cumulative distribution function Φ, we have $h_t(c) = p_t(c) - 1 + p_{-t}(c)$, thus h_t is smooth on $(-1,1)$ and its derivative is equal to $h'_t(c) = p'_t(c) + p'_{-t}(c)$. Moreover, for all $c \in (-1,1)$,

$$
\begin{aligned}
p'_t(c) &= \mathbb{E}\left(\frac{-2|U|-t\sqrt{2(1-c)}}{2(1+c)\sqrt{1-c^2}}\Phi'\left(\frac{2t+|U|\sqrt{2(1-c)}}{\sqrt{2(1+c)}}\right)\right)\\
&= \frac{\exp(-t^2/(1+c))}{2\sqrt{2\pi}(1+c)\sqrt{1-c^2}}\\
&\qquad \mathbb{E}\left(\left(-2|U|-t\sqrt{2(1-c)}\right)\exp\left(\frac{-t|U|\sqrt{2(1-c)}}{1+c}\right)\exp\left(\frac{-U^2(1-c)}{2(1+c)}\right)\right)\\
&= \frac{\exp(-t^2/(1+c))}{4\pi(1+c)\sqrt{1-c^2}}\\
&\qquad \int_{-\infty}^{\infty}\exp\left(-\frac{y^2}{1+c}\right)\left(\left(-2|y|-t\sqrt{2(1-c)}\right)\exp\left(\frac{-t|y|\sqrt{2(1-c)}}{1+c}\right)\right)dy\\
&= \frac{\exp(-t^2/(1+c))}{2\pi(1+x)\sqrt{1-c^2}}\exp\left(\frac{t^2(1-c)}{2(1+c)}\right)\\
&\qquad \int_{0}^{\infty}\left(-2y-t\sqrt{2(1-c)}\right)\exp\left(-\frac{\left(y+t\sqrt{2(1-c)}/2\right)^2}{1+c}\right)dy\\
&= \frac{-\exp(-t^2/(1+c))}{2\pi\sqrt{(1-c^2)}}.
\end{aligned}
$$

Thus, $h'_t(x) = \frac{-\exp(-t^2/(1+x))}{\pi\sqrt{(1-x^2)}}$ and besides $h(1) = 0$, which gives the desired formula (3.4) for $h_t(c)$.

If $c = -1$, then there exists $N \sim \mathcal{N}(0,1)$ such that $(X_0, X_{e_i}) \overset{d}{=} (N,-N)$ and thus,

$$
\mathbb{E}\left(f_t^{(i)}(0)\right) = \mathbb{E}\left(\mathbb{1}_{\{\min(N,-N)<t\le\max(N,-N)\}}\right) = \mathbb{P}\left(|t|\le|N|\right) = 2\left(1-\Phi\left(|t|\right)\right).
$$

☐

Proof of Lemma 3.3.4.

Let us start with the computation of $\mathrm{Cov}(\mathcal{P}_m^{(1)}(t), \mathcal{P}_m^{(1)}(s))$. By stationarity, we have

$$\mathrm{Cov}(\mathcal{P}_m^{(1)}(t), \mathcal{P}_m^{(1)}(s)) = \sum_{x \in \mathbb{G}_m^{(1)}} \sum_{y \in \mathbb{G}_m^{(1)}} \mathrm{Cov}\left(f_t^{(1)}(0), f_s^{(1)}(y-x)\right).$$

For $z_1 = y_1 - x_1$ one has

$$\left\{ \begin{array}{l} 0 \leq x_1 \leq m-2 \\ 0 \leq y_1 \leq m-2 \end{array} \right. \Leftrightarrow \left\{ \begin{array}{l} 2-m \leq z_1 \leq m-2 \\ \max(0, -z_1) \leq x_1 \leq \min(m-2, m-2-z_1) \end{array} \right. ,$$

and similarly for $z_2 = y_2 - x_2$

$$\left\{ \begin{array}{l} 0 \leq x_2 \leq m-1 \\ 0 \leq y_2 \leq m-1 \end{array} \right. \Leftrightarrow \left\{ \begin{array}{l} 1-m \leq z_2 \leq m-1 \\ \max(0, -z_2) \leq x_2 \leq \min(m-1, m-1-z_2) \end{array} \right. .$$

Thus,

$$\begin{aligned} &\mathrm{Cov}\left(\mathcal{P}_m^{(1)}(t), \mathcal{P}_m^{(1)}(s)\right) \\ &= \sum_{z_1=(2-m)}^{m-2} \sum_{z_2=(1-m)}^{m-1} \left(m-1-|z_1|\right)\left(m-|z_2|\right) \mathrm{Cov}\left(f_t^{(1)}(0), f_s^{(1)}(z)\right). \end{aligned}$$

For $\mathrm{Cov}\left(\mathcal{P}_m^{(1)}(t), \mathcal{P}_m^{(2)}(s)\right)$, we still have by stationarity

$$\mathrm{Cov}\left(\mathcal{P}_m^{(1)}(t), \mathcal{P}_m^{(2)}(s)\right) = \sum_{x \in \mathbb{G}_m^{(1)}} \sum_{y \in \mathbb{G}_m^{(2)}} \mathrm{Cov}\left(f_t^{(1)}(0), f_s^{(2)}(y-x)\right),$$

and again, considering $z_1 = y_1 - x_1$ and $z_2 = y_2 - x_2$, we get

$$\begin{aligned} &\mathrm{Cov}\left(\mathcal{P}_m^{(1)}(t), \mathcal{P}_m^{(2)}(s)\right) \\ &= \sum_{z_1=2-m}^{m-1} \sum_{z_2=1-m}^{m-2} \left(m-|z_1|-\mathbb{1}_{z_1 \leq 0}\right)\left(m-|z_2|-\mathbb{1}_{z_2 \geq 0}\right) \mathrm{Cov}\left(f_t^{(1)}(0), f_s^{(2)}(z)\right). \end{aligned}$$

□

Proof of Lemma 3.3.5.
The covariance matrix Σ_n is invertible if the Gaussian vector $(X_{x_1}, \ldots, X_{x_n})$ is non degenerate. So, let $\lambda_1, \ldots, \lambda_n \in \mathbb{R}$ such that $\sum_{j=1}^n \lambda_j X_{x_j} = 0$, *a.s.* Then,

$$\begin{aligned} 0 = \mathrm{Var}\left(\sum_{j=1}^n \lambda_j X_{x_j}\right) &= \sum_{j=1}^n \sum_{k=1}^n \lambda_j \lambda_k \mathrm{Cov}\left(X_{x_j}, X_{x_k}\right) \\ &= \sum_{j=1}^n \sum_{k=1}^n \lambda_j \lambda_k \mathrm{Cov}\left(X_0, X_{x_k - x_j}\right) = \sum_{j=1}^n \sum_{k=1}^n \lambda_j \lambda_k \rho\left(x_k - x_j\right). \end{aligned}$$

We use the fact that ρ has a spectral density, say f, thus

$$
\begin{aligned}
0 &= \sum_{j=1}^{n}\sum_{k=1}^{n} \lambda_j \lambda_k \int_{\mathbb{T}^2} e^{i(x_k - x_j).\xi} f(\xi) d\xi \\
&= \int_{\mathbb{T}^2} \sum_{j=1}^{n}\sum_{k=1}^{n} \lambda_j \lambda_k e^{i(x_k - x_j).\xi} f(\xi) d\xi \\
&= \int_{\mathbb{T}^2} \left(\sum_{k=1}^{n} \lambda_k e^{i x_k .\xi} \right) \left(\sum_{j=1}^{n} \lambda_j e^{-i x_j .\xi} \right) f(\xi) d\xi \\
&= \int_{\mathbb{T}^2} \left| \sum_{k=1}^{n} \lambda_k e^{i x_k .\xi} \right|^2 f(\xi) d\xi .
\end{aligned}
$$

Here we note the torus $\mathbb{T} = \mathbf{R}/2\pi\mathbb{Z}$ identified with $(0, 2\pi]$. Since there exists an open set U in $(0, 2\pi]^2$ with positive measure such that $f > 0$ on U, then $\forall \xi \in U$, $\left|\sum_{k=1}^{n} \lambda_k e^{i x_k .\xi}\right|^2 = 0$. The family of functions $(\xi \mapsto e^{i x_k .\xi})_{1 \leq k \leq n}$ defined on U being linearly independent, it implies that $\lambda_1 = \ldots = \lambda_n = 0$, which gives the result. ☐

Proof of Lemma 3.3.7.

Let us begin by reconsidering the coefficients introduced in Lemma 3.A1.1, and note $\sigma_i^{(-)} = \sqrt{1 - \rho(e_i)}$ and $\sigma_i^{(+)} = \sqrt{1 + \rho(e_i)}$

- If $r(x) = 0$, then, $\pi_U^{(-,i)}(x) = \pi_U^{(+,i)}(x) = \pi_V^{(-,i)}(x) = \pi_V^{(+,i)}(x) = 0$, $\pi_W^{(-,i)}(x) = \sigma_i^{(-)}$ and $\pi_W^{(+,i)}(x) = \sigma_i^{(+)}$ and hence, $\mathrm{Cov}\left(f_t^{(1)}(0), f_s^{(i)}(x)\right) = 0$.
- Else, recalling the expressions introduced in Lemma 3.A1.1, we first get

$$
\left|\pi_U^{(\pm,i)}(x)\right| \leq \frac{4r(x)}{\sigma_1^{(-)}}, \qquad \left|\pi_V^{(-,i)}(x)\right| \leq \frac{4r(x)}{\sigma_1^{(+)}}. \tag{3.16}
$$

Then, subtracting $\sigma_i^{(-)}$ and applying inequality in (3.16) we get,

$$
\begin{aligned}
\left|\pi_W^{(-,i)}(x) - \sigma_i^{(-)}\right| &\leq \sigma_i^{(-)} \left| \left(1 - \frac{\pi_U^{(-,i)}(x)^2}{\left(\sigma_i^{(-)}\right)^2} - \frac{\pi_V^{(-,i)}(x)^2}{\left(\sigma_i^{(-)}\right)^2} \right)^{(1/2)} - 1 \right| \\
&\leq \frac{16 r^2(x)}{\sigma_i^{(-)}} \left(\frac{1}{(\sigma_i^{(-)})^2} + \frac{1}{(\sigma_i^{(+)})^2} \right).
\end{aligned} \tag{3.17}
$$

From (3.16) and (3.17), we also get

$$
\begin{aligned}
&\left|\pi_W^{(+,i)}(x)\right| = \frac{-1}{\pi_W^{(-,i)}(x)} \left(\pi_U^{(-,i)}(x) \pi_U^{(+,i)}(x) + \pi_V^{(-,i)}(x) \pi_V^{(+,i)}(x) \right) \\
&\leq 16 r(x)^2 \left(\frac{1}{(\sigma_i^{(-)})^2} + \frac{1}{(\sigma_i^{(+)})^2} \right) \left(\sigma_i^{(-)} - \frac{16 r^2(x)}{\sigma_i^{(-)}} \left(\frac{1}{(\sigma_i^{(-)})^2} + \frac{1}{(\sigma_i^{(+)})^2} \right) \right)^{-1} .
\end{aligned} \tag{3.18}
$$

Finally, from (3.16) and (3.18)

$$\left|\pi_Z^{(+,i)}(x)-\sigma_i^{(+)}\right| \leq \frac{16r^2(x)}{\sigma_i^{(+)}}\left(\frac{1}{(\sigma_i^{(-)})^2}+\frac{1}{(\sigma_i^{(+)})^2}+\frac{\pi_W^{(+,i)}(x)^2}{16r^2(x)}\right). \tag{3.19}$$

Let

$$R_1(x) = \frac{2s+\left(\pi_U^{(-,i)}(x)-\pi_U^{(+,i)}(x)\right)U+\left(\pi_V^{(-,i)}(x)-\pi_V^{(+,i)}(x)\right)V+\left(\pi_W^{(-,i)}(x)-\pi_W^{(+,i)}(x)\right)W}{\pi_Z^{(+,i)}(x)}-\frac{2s+\sigma_i^{(-)}W}{\sigma_i^{(+)}},$$

$$R_2(x) = \frac{2s-\left(\pi_U^{(-,i)}(x)+\pi_U^{(+,i)}(x)\right)U-\left(\pi_V^{(-,i)}(x)+\pi_V^{(+,i)}(x)\right)V-\left(\pi_W^{(-,i)}(x)+\pi_W^{(+,i)}(x)\right)W}{\pi_Z^{(+,i)}(x)}-\frac{2s-\sigma_i^{(-)}W}{\sigma_i^{(+)}}.$$

Considering $R_1(x)$

$$\begin{aligned}|R_1(x)| = \Bigg| & \frac{\sigma_i^{(+)}\left(2s+\pi_W^{(-,i)}(x)W\right)-\pi_Z^{(+,i)}(x)\left(2s+\sigma_i^{(-)}W\right)}{\sigma_i^{(+)}\pi_Z^{(+,i)}(x)} \\ & +\frac{\sigma_i^{(+)}\left(\left(\pi_U^{(-,i)}(x)-\pi_U^{(+,i)}(x)\right)U+\left(\pi_V^{(-,i)}(x)-\pi_V^{(+,i)}(x)\right)V-\pi_W^{(+,i)}(x)W\right)}{\sigma_i^{(+)}\pi_Z^{(+,i)}(x)}\Bigg|.\end{aligned}$$

Using the previous inequalities, there exists a constant $C_1 \in \mathbb{R}^+$ depending, on $s, \sigma_i^{(+)}, \sigma_i^{(-)}$ such that, $|R_1(x)| \leq C_1 r(x)\left(|U|+|V|+|W|\right)$.

Also, there exists C_2 such that $R_2(x) \leq C_2 r(x)\left(|U|+|V|+|W|\right)$. Reconsidering Equation (3.5) we get,

$$\begin{aligned}&\mathrm{Cov}\left(f_t^{(1)}(0), f_s^{(i)}(x)\right) = \mathbb{E}\Bigg(\mathbb{1}_{\left\{|2t-\sigma_1^{(+)}V|\leq|\sigma_1^{(-)}U|\right\}} \\ &\Big|\Phi_{\pi_Z^{(+,i)}(x)}\left(2s+\left(\pi_U^{(-,i)}(x)-\pi_U^{(+,i)}(x)\right)U+\left(\pi_V^{(-,i)}(x)-\pi_V^{(+,i)}(x)\right)V+\left(\pi_W^{(-,i)}(x)-\pi_W^{(+,i)}(x)\right)W\right) \\ &-\Phi_{\pi_Z^{(+,i)}(x)}\left(2s-\left(\pi_U^{(-,i)}(x)+\pi_U^{(+,i)}(x)\right)U-\left(\pi_V^{(-,i)}(x)+\pi_V^{(+,i)}(x)\right)V-\left(\pi_W^{(+,i)}(x)+\pi_W^{(-,i)}(x)\right)W\right)\Big|\Bigg) \\ &-\mathbb{E}\left(\mathbb{1}_{\left\{|2t-\sigma_1^{(+)}V|\leq|\sigma_1^{(-)}U|\right\}}\left|\Phi\left(\frac{2s+\sigma_i^{(-)}W}{\sigma_i^{(+)}}\right)-\Phi\left(\frac{2s-\sigma_i^{(-)}W}{\sigma_i^{(+)}}\right)\right|\right) \\ &=\mathbb{E}\Bigg(\mathbb{1}_{\left\{|2t-\sigma_1^{(+)}V|\leq|\sigma_1^{(-)}U|\right\}}\Bigg(\Bigg|\Phi\left(\frac{2s+\sigma_i^{(-)}W}{\sigma_i^{(+)}}+R_1(x)\right)-\Phi\left(\frac{2s-\sigma_i^{(-)}W}{\sigma_i^{(+)}}+R_2(x)\right)\Bigg| \\ &\qquad\qquad -\left|\Phi\left(\frac{2s+\sigma_i^{(-)}W}{\sigma_i^{(+)}}\right)-\Phi\left(\frac{2s-\sigma_i^{(-)}W}{\sigma_i^{(+)}}\right)\right|\Bigg)\Bigg) \\ &\leq\mathbb{E}\Bigg(\Bigg|\Phi\left(\frac{2s+\sigma_i^{(-)}W}{\sigma_i^{(+)}}+R_1(x)\right)-\Phi\left(\frac{2s+\sigma_i^{(-)}W}{\sigma_i^{(+)}}\right) \\ &\qquad\qquad +\Phi\left(\frac{2s-\sigma_i^{(-)}W}{\sigma_i^{(+)}}\right)-\Phi\left(\frac{2s-\sigma_i^{(-)}W}{\sigma_i^{(+)}}+R_2(x)\right)\Bigg|\Bigg) \\ &\leq\mathbb{E}\Bigg(\Bigg|\Phi\left(\frac{2s+\sigma_i^{(-)}W}{\sigma_i^{(+)}}+R_1(x)\right)-\Phi\left(\frac{2s+\sigma_i^{(-)}W}{\sigma_i^{(+)}}\right)\Bigg| \\ &\qquad\qquad +\Bigg|\Phi\left(\frac{2s-\sigma_i^{(-)}W}{\sigma_i^{(+)}}\right)-\Phi\left(\frac{2s-\sigma_i^{(-)}W}{\sigma_i^{(+)}}+R_2(x)\right)\Bigg|\Bigg).\end{aligned}$$

Applying the mean value theorem, there exists a constant $C \in \mathbb{R}^+$ such that

$$\left|\mathrm{Cov}\left(f_t^{(1)}(0), f_s^{(i)}(x)\right)\right| \leq C\mathbb{E}\left(|R_1(x)|+|R_2(x)|\right) \leq Cr(x),$$

and thus we get the result. $\square$

Proof of Theorem 3.3.8. For the sake of simplicity, we will prove the theorem for one threshold (*i.e.* $r = 1$), the generalized case can be established by following a similar procedure. Let $t \in \mathbb{R}$. Using the Cramèr-Wold method, we will prove that for each $(a_1, a_2) \in \mathbb{R}^2$, we have

$$\frac{a_1}{m}\left(\mathcal{P}^{(1)}_m(t) - \mathbb{E}\left(\mathcal{P}^{(1)}_m(t)\right)\right) + \frac{a_2}{m}\left(\mathcal{P}^{(2)}_m(t) - \mathbb{E}\left(\mathcal{P}^{(2)}_m(t)\right)\right) \xrightarrow[m\to\infty]{d} \mathcal{N}\left(0,\, \sigma^2(t)\right)$$

with $\sigma^2(t) < \infty$. For $x \in \mathbb{G}_m$, by using the notation introduced in (3.1), we consider the 3-dimensional Gaussian vector $\mathbb{X}_x = (\mathbb{X}^{(i)}_x)_{1\leq i\leq 3} = (X_x, X_{x+e_1}, X_{x+e_2})$ and the function g_t defined on $\mathbb{R}^3$,

$$g_t\left(u, v, w\right) := a_1 \mathbb{1}_{\{\min(u,v) < t \leq \max(u,v)\}} + a_2 \mathbb{1}_{\{\min(u,w) < t \leq \max(u,w)\}}.$$

Hence, re-writing the following sum, we get

$$\sum_{x\in\mathbb{G}_m} g_t\left(\mathbb{X}_x\right) = \sum_{x_1=0}^{m-1}\sum_{x_2=0}^{m-1} g_t\left(\mathbb{X}_{x_1,x_2}\right) = a_1\mathcal{P}^{(1)}_m(t) + a_2\mathcal{P}^{(2)}_m(t) + A^{(1)}_m + A^{(2)}_m,$$

where

$$A^{(1)}_m = a_1 \sum_{x_2=0}^{m-1} f^{(1)}_t(m-1, x_2) \text{ and } A^{(2)}_m = a_2 \sum_{x_1=0}^{m-1} f^{(2)}_t(x_1, m-1).$$

Note that $|g(t)| \leq |a_1| + |a_2|$, thus, $\mathbb{E}\left(g_t\left(\mathbb{X}_{0,0}\right)^2\right) < (|a_1| + |a_2|)^2$. On the one hand, under $(\mathcal{A}1)$, for all $1 \leq p, q \leq 3$,

$$\lim_{m\to\infty} m^{-2} \sum_{x\in\mathbb{G}_m}\sum_{y\in\mathbb{G}_m} \mathbb{E}\left(\mathbb{X}^{(p)}_x \mathbb{X}^{(q)}_y\right) \quad \text{exists,}$$

since ρ is the covariance function of X. On the other hand, $(\mathcal{A}3)$ implies that $\sum_{x\in\mathbf{Z}^2}\rho(x)^2 < +\infty$. Indeed, it comes from Fatou's Lemma using the fact that

$$\frac{1}{m^2}\sum_{x,y\in\mathbb{G}_m}\rho(x-y)^2 = \sum_{|x_1|<m}\sum_{|x_2|<m}\left(1 - \frac{|x_1|}{m}\right)\left(1 - \frac{|x_2|}{m}\right)\rho(x)^2.$$

Applying again Fatou's lemma yields the existence of

$$\lim_{m\to\infty} m^{-2} \sum_{x\in\mathbb{G}_m}\sum_{y\in\mathbb{G}_m} \mathbb{E}\left(\mathbb{X}^{(p)}_x \mathbb{X}^{(q)}_y\right)^2 \quad \forall p, q \in \{1, 2, 3\}.$$

Hence, we can apply Theorem 2 in Arcones (1994) and get that

$$m^{-1}\sum_{x\in\mathbb{G}_m} g_t\left(\mathbb{X}_x\right) - \mathbb{E}\left(g_t\left(\mathbb{X}_x\right)\right) \xrightarrow[m\to\infty]{d} \mathcal{N}\left(0,\, \sigma^2(t)\right).$$

Now, it only remains to check that $\frac{1}{m}A^{(i)}_m$ tends to 0 in probability for $1 \leq i \leq 2$. Let us verify it for $A_m^{(1)}$. By stationarity, the random variable $A_m^{(1)}$ has the same law as

$$\tilde{A}_m^{(1)} = \sum_{x_2=0}^{m-1} \tilde{g}_t(X_{0,x_2}, X_{1,x_2}), \quad \text{where } \tilde{g}_t(u,v) = a_1 \mathbb{1}_{\{\min(u,v)<t\leq\max(u,v)\}}.$$

Then, Assumptions ($\mathcal{A}2$) and ($\mathcal{A}3$) ensure that we can again apply Theorem 2 in Arcones (1994) so that the convergence in distribution of $\left(\frac{1}{m^{1/2}}\left(\tilde{A}_m^{(1)} - \mathbb{E}(\tilde{A}_m^{(1)})\right)\right)_m$ implies that $\left(\frac{1}{m}\left(\tilde{A}_m^{(1)} - \mathbb{E}(\tilde{A}_m^{(1)})\right)\right)_m$ tends to 0 in probability.

4 TOPOLOGICAL DATA ANALYSIS & LIPSCHITZ-KILLING CURVATURES

This chapter is an ongoing work in collaboration with Ian Morrilla, researcher at the Institute of Subtropical and Mediterranean Horticulture (IHSM), university of Málaga.

The recent progress that have been made in medical imaging has allowed the use of image processing tools, alongside the introduction of novel methods, for the processing of medical data, which provided healthcare professionals with diagnostic assistance in evaluating the severity of the disease alongside monitoring its progression Gatenby et al. (2013); Ranjbar and Ross Mitchell (2017); Singh et al. (2023). In this chapter, we aim to perform a classification task on skin cancer data, by capturing relevant geometrical and topological information from the dataset that would help to characterize the images in a finer way. To achieve that, we use tools from both the realm of integral geometry and the realm of Topological Data Analysis (TDA). Through this classification task, we aim to compare the performances of each features (geometrical and topological) and explore the potential benefits that combining both geometry and topology may offer in the context of supervised classification.

4.1 Quick introduction to Topological Data Analysis

Topological Data Analysis is a fast-growing field that provides mathematically well-founded methods that uncover the inherent topological patterns present in a data-set and represents them as quantitative and qualitative features that are well-suited for machine learning tasks. It aims to analyze and exploit the underlying topological structures data to perform tasks such as classification, segmentation, clustering, etc. the goal is to find relevant topological features of the object of interest, may it be a 1-D signal (Dindin et al. (2020)), a point cloud Chazal et al. (2013) or an image (Vandaele et al. (2020)). In this dissertation, we focus our attention on the latter, the goal being to perform a classification or segmentation task using the extracted topological features. The use of TDA in image processing is surprisingly relatively recent Garin and Tauzin (2019), despite the fact that the natural grid-like structure of the image makes it perfectly suited for the TDA method.

One of the pioneering applications of TDA in image processing can be attributed to Letscher and Fritts (2007). This study used the topologically based method to differentiate core regions from smaller ones within the image for the purpose of classification. In the medical field, Vandaele et al. (2020) use TDA to increase the performance of identifying and segmenting important objects on images, leading to an unsupervised method for the segmentation of skin lesion images. Somasundaram et al. (2021) apply the theory to tumor CT scans and show that these topological tools can predict survival rates in lung cancer patients. Vandaele et al. (2022) use it on thoracic radiographic images for lung tumor histology prediction and shows that it improves classification between malignant vs. benign tumors when combined with radiomic features (*i.e.* a large number of features from medical images using data-characterization algorithms). Chung et al. (2018) is using TDA to segment skin cancer images and classify different types of skin lesions. Consequently, this technique is widely used in machine learning for summarizing the global and local topological features of data, usually without considering the underlying geometric characteristics. Luo and Strait (2021) proposes a method that exploits both the geometrical and topological information within an image to estimate the boundaries of objects within images, which raises the question of the potential benefits of combining both approaches.

In this chapter, we start by introducing an important concept from Topological Data Analysis which is called *persistent homology* that extracts the topological features of the data that are then used to perform the classification task. Persistent homology is a procedure that allows to infer the so-called *homology groups* of a data set. We will provide a brief overview of the homology theory that is of interest to us, as stated by the authors in Adler et al. (2010), “This is done via examples rather than formal definitions, so it should be possible to understand the notion of persistent homology without actually knowing what a homology group is” and refer the reader to Hatcher (2000) for a thorough introduction. Then, we will briefly present the geometrical model using the geometrical features that are available in our bivariate framework, namely the area, perimeter, and Euler characteristic. All the features above are given to a supervised machine learning classifier to classify skin cancer 2-dimensional data. Then compare the performance of each model and the performance obtained when both are combined.

TDA is often used in conjunction with other machine learning models to enhance their performance and provide additional insights. In the context of the aforementioned study on skin cancer data, the goal is to explore the potential benefits of combining both geometric and topological models for classification tasks. It is important to note that both methods are not meant to replace other machine learning techniques but rather to complement them and reveal hidden topological and geometrical features that may be valuable for the classification task.

By combining TDA with geometric features like area, perimeter, and Euler characteristic, the aim is to compare the performance of each model individually and evaluate the improvements achieved when both geometry and topology are utilized.

4.2 From an image to a persistence diagram

Since our area of interest is image processing, we will focuse on describing the process of TDA when the input is an image. For a general and thorough presentation of the process we refer the reader to Chazal and Michel (2021).

THE WHOLE PROCESS IN A NUTSHELL The input grayscale image X of size $m \times m$ can be seen as a function from $\mathbb{G}_m := [0, m]^2 \cap \mathbb{Z}^2$ to $\mathbb{R}, x \mapsto X_x$ that associates to each pixel x its intensity which is a value in $\mathbb{R}$. We consider the set of binary images $\{x, X_x \geq t\}_t$ that are associated to X. This family, in the TDA realm is known as the upper-level set *filtration* (also known in our case as excursion sets). The filtration encodes the topological structure of the image X at different levels. From the study of that set of ordered binary images, we extract the topological features and encode them in something called the *persistence diagram*.

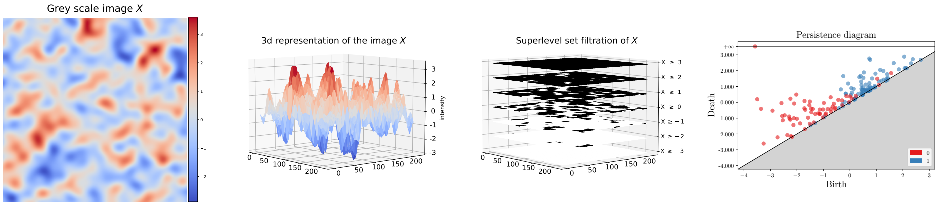

Figure 4.1 – Extraction of the topological feature from a grayscale image X.

The whole process of extracting the topological features is called persistent homology, which is the most widely used technique in TDA. It gives a theoretical framework to enable the inference of the *homology group* of a given dataset. Although persistent homology is primarily applied to point clouds, it can also be extended to images by using their cubical structure.

4.2.1 (Static) Homology groups

Homology is a fundamental concept in algebraic topology, which provides a valuable tool for formalizing and representing the topological characteristics of a given topological space in an algebraic manner. It is an operator that transforms topological spaces into vector spaces (in our case $\mathbb{Z}/2\mathbb{Z}$-vector spaces), by assigning to the topological space a sequence of vector spaces, each vector space encodes the characteristics of a topological feature. For any dimension k, it allows us to capture and quantify the presence of any k-dimensional "holes" in the space. These holes are described by vector spaces denoted as H_k and called *homology groups*. The dimension of H_k intuitively corresponds to the number of independent features ("holes") of k-dimension. For instance, the 0-dimensional homology group H_0 represents the connected components of the space, H_1 captures 1-dimensional loops, H_2 represents 2-dimensional cavities, and so on. We will not go into the details of how it is rigorously constructed. We refer the reader to Hatcher (2000) for a thorough presentation of homology theory and algebraic topology. In order to compute the homology of a space, it has to possess a topological structure and there is no canonical way to provide it for grayscale images, an alternative would be to consider for a fixed threshold $t \in \mathbb{R}$, the associated black-and-white image. The set of white pixels that is the excursion set, $\mathcal{X}_t(X) = \{x \in \mathbb{G}_m, X_x \geq t\}$, seen as a subset of $\mathbb{G}_m$, inherits its topological structure, it is then possible to compute the homology groups (H_k) of $\mathcal{X}_t(X)$. Besides, within the theory of homology, *cubical homology*, Strömbom (2007) is well-suited for image analysis. It transforms binary images (a union of cubes) into vector spaces. In Figure 4.2 the black and white image contains three independent features in dimension 0, that correspond each to a connected component, and two holes in dimension 1 that are the cycles inside of the empty circles.

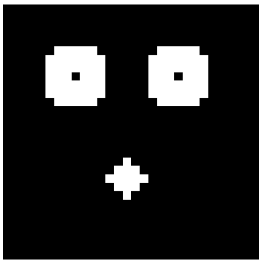

Figure 4.2 – Black and white image of size $m = 30$, $dim(H_0) = 3$, $dim(H_1) = 2$

Persistent homology and persistence diagram

Instead of only considering one threshold, one has the option to iterate through all the pixel values of the image X, generating a series of black and white images $(\mathcal{X}_t(X))_{t \in \mathbb{R}}$ and to follow the evolution of the homology groups all along. The knowledge of $(\mathcal{X}_t(X))_{t \in \mathbb{R}}$ enables the reconstruction of the image X, thus it encodes all the topological and geometrical informations. This type of homology is different from classical (static) homology in that it describes the evolution of a dynamic complex. More precisely, to follow the evolution of the homology, it is important to get an increasing family of binary images, in the sense that if a pixel gets activated (turns white) at a given threshold t, it has to stay that way for all $s \leq t$. In other words, if a topological feature appears it can not just vanish, it can either remain unchanged or continue to grow until it merges with another feature. To ensure that, we browse through the values of the image from the maximum value to the minimum one. Thus, we browse the range of threshold values from $+\infty$ to $-\infty$. For any, $s, t \in \mathbb{R}$ such that $s \leq t$ then $\mathcal{X}_t(X) \subseteq \mathcal{X}_s(X)$, thus, we get an increasing family of binary images indexed by the parameter t. It is called the *superlevel sets filtration* of X. Similarly, we can define the set of pixels with intensity lower or equal to t, then we obtain the *sublevel sets filtration* of X.

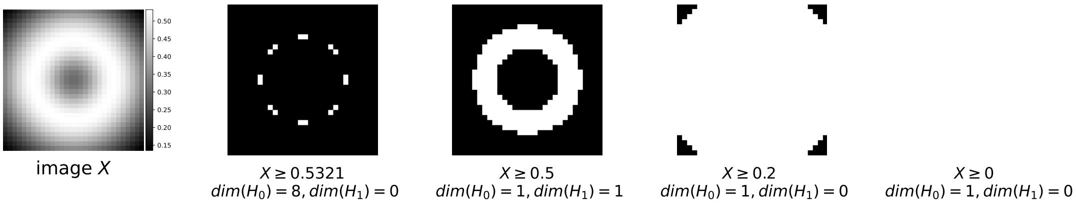

image X

$X \geq 0.5321$
$dim(H_0) = 8, dim(H_1) = 0$

$X \geq 0.5$
$dim(H_0) = 1, dim(H_1) = 1$

$X \geq 0.2$
$dim(H_0) = 1, dim(H_1) = 0$

$X \geq 0$
$dim(H_0) = 1, dim(H_1) = 0$

Figure 4.3 – Superlevel filtration of the image X.

In this procedure, the parameter t can be viewed as a temporal value, as illustrated in Figure 4.3, pixels with higher values are activated initially, meaning that the brightest regions of the image emerge first in the filtration sequence, while the darkest areas appear last. Ultimately, all the pixels in the image are included in the process. It is then possible to follow the evolution of topological features in the filtrations, a feature can appear (birth) at time t_b and evolve until it merges with another feature (death) at time t_d. The only way a component can die, is if it merges with another component, the component that survives the merge is decided to be the oldest. We can track the life of each connected component and encode it in something called the *persistence barcode*, and represent the birth and death coordinate in a *persistence diagram*.

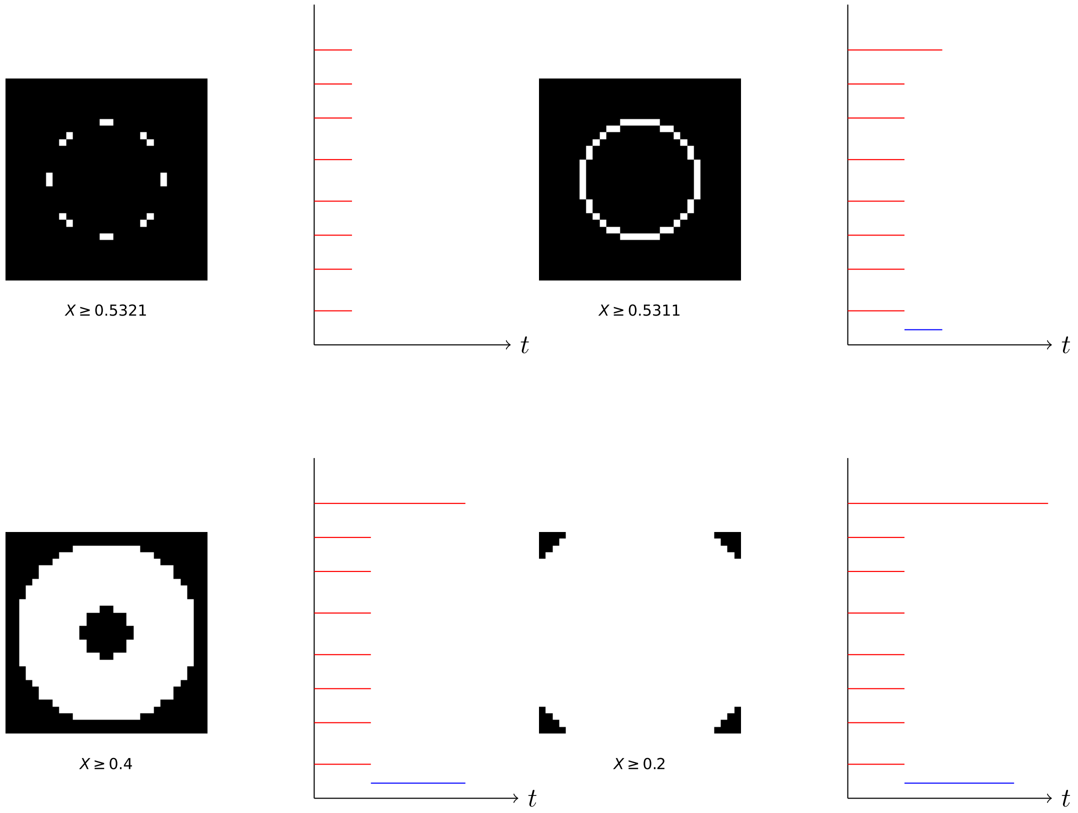

Figure 4.4 – Capturing the changes of the topological features in $\mathcal{X}_t(X)$ as the threshold t evolves.

In Figure 4.4, each horizontal bar represents a topological feature, and its color indicates the dimension of the feature (red for an H_0 component and blue for an H_1 component). The bar begins at the time of the feature's birth and ends at the time of its death, which occurs when two component merges together or when a cycle in H_1 is filled up. The length of the bar represents the lifespan of the feature, reflecting the duration from birth to death, the interval on which a feature exists is called its *persistence*. In practice, features with significant persistence are interpreted as relevant features within the data set, indicating meaningful patterns or structures. Conversely, features with low persistence are typically regarded as noise or insignificant fluctuations. Eventually, all features will cease to exist except for one, which prevails as the final surviving component.

Each of those features is summarized as a point in a persistence diagram as in Figure 4.5. The further a feature is from the diagonal, the more persistent it is in the image. Thus, points that are closer to the diagonal are perceived as noise. As we can see in Figure

4.5, there are only two topological features that are important in the image, one connected component and one hole, as the 7 other connected components merge and disappear very quickly during the process.

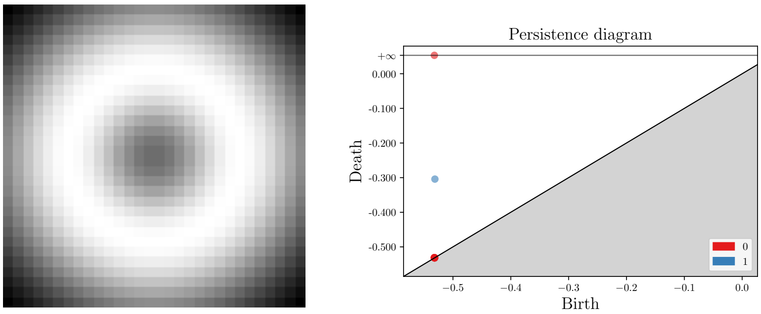

X

Figure 4.5 – The persistence diagram of the image X.

4.2.2 Lipschitz-Killing Curvatures

The Lipschitz-Killing curvatures (LKCs) constitute a widely used and intricate class of geometric summarizing tools. While the conventional approach has been to concentrate on the theoretical examination of each LK curvatures, recent theoretical papers (see Kratz and Vadlamani (2017); Müller (2017)) have aimed to explore the collective behavior of LK curvatures within excursion sets. The significance of investigating the geometry of random sets stems from Hadwiger's characterization theorem, which establishes the LKCs as a basis for all rigid motion invariant valuations of convex bodies. Consequently, LKCs offer concise and insightful overviews of the spatial characteristics of the random fields under scrutiny. In this study, our research concentrates on the two-dimensional domain, specifically random fields defined on $\mathbb{Z}^2$. Within this particular context, to describe the geometry of excursion sets of random fields, we have access to three distinct LKCs : the area of the set, the perimeter, and last but not least, the Euler-Poincaré characteristic, which is equal to the number of connected components minus the number of holes within the excursion set, it also constitutes a topological invariant. Each of these geometrical features captures aspects of the spatial properties:

- The surface area is linked to the occupation density.
- The perimeter reflects the regularity of the set.
- The Euler characteristic denotes the level of connectivity.

Hence, LKCs emerge as powerful tools for providing meaningful and succinct summaries regarding the spatial properties exhibited by the random fields under investigation.

Therefore, it is interesting to explore what both method have to offer. Moreover, what they eventually can bring to each other. Such a comparison can uncover each approach's unique insights and benefits, fostering a more comprehensive understanding of their combined capabilities.

4.3 Presentation of the data set

The dataset contains a balanced set of benign and malignant skin moles, images of dimension $(3, 224, 224)$ 1800 benign moles and 1497 malignant ones. The dataset was provided by the *The International Skin Imaging Collaboration*. It can be found on the *Kaggle* website, where it is registered under the name Skin Cancer: Malignant vs. Benign. We start by applying a little bit of pre-processing to the images of the dataset to ensure that the tumor has the highest values in the image and the lowest values are attributed to the back ground, we then center and reduce the image.
Figure 4.6 is a grayscale representation of two images from the dataset of a benign mole and a malignant tumor and some of their respective excursion sets. In this representation, black represents pixels of value 0, while white represents pixels of value 1. At the start of the iterative thresholding process, as we iterate from the highest value of the image to the lowest one to construct the filtration, only pixels that belong to the mole get activated, which distinguishes them from the background. At the end of the process, all pixels turn white as we reach the minimum value of the image.

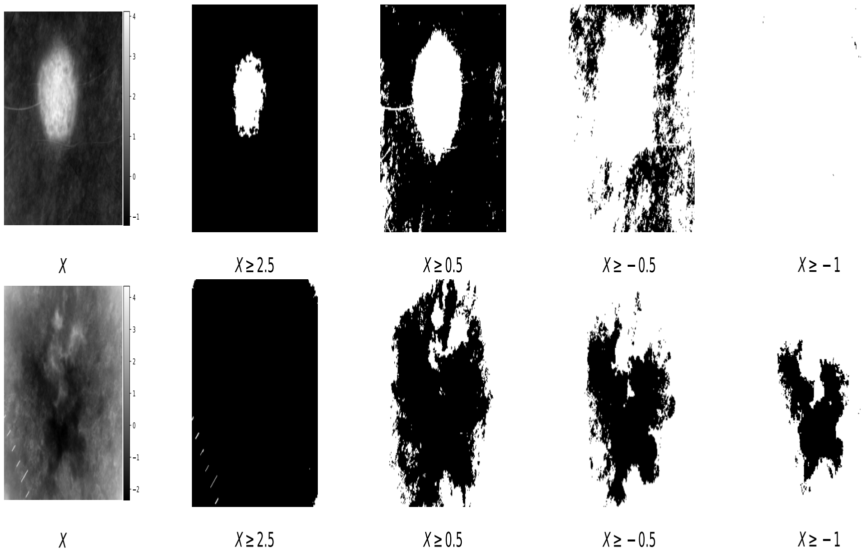

Figure 4.6 – Grayscale image of a benign (first row) and malignant tumor (second row) and their respective excursion sets.

4.3.1 Extraction of the topological and geometrical features

The feature extraction was done on all three (RGB) canals in addition to the grayscale image.

TOPOLOGICAL FEATURES Following the idea presented in Garin and Tauzin (2019), we extract the topological characteristics of the image and construct the vector of features that will be fed to the machine learning model. To do that, we use the Python module **gtda.images** that implements several tools to apply Topological Data Analysis to images.

We consider the image's natural filtration (presented above) and thus start by applying the function **gtda.homology.CubicalPersistence** to construct the persistence diagram of dimensions 0 and 1 and to follow the pipeline presented in Garin and Tauzin (2019), where they define the *amplitude* of a persistence diagram as being its distance to the empty diagram (a diagram which contains only the diagonal points). We consider all the metrics available in the Python module to compute the norm of the diagrams. To each persistence diagram, we associate 7 amplitudes and the entropy of the diagram for a total of 8 features per canal of image (grey-scale, red, green, blue) per dimension of the diagram, for a total of 64 feature per image to make the classification.

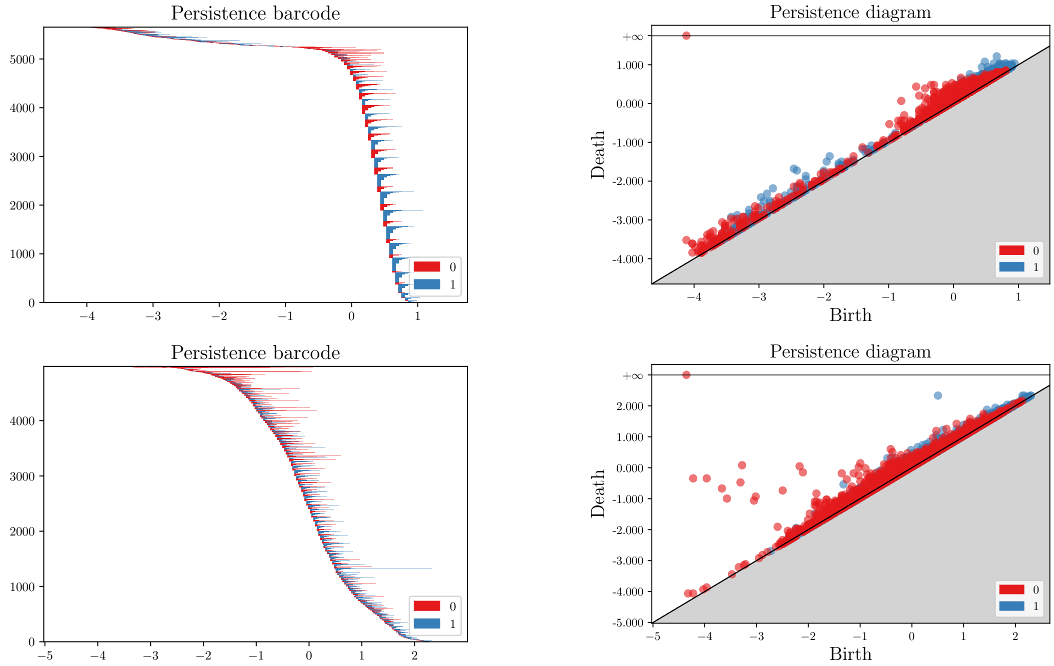

Figure 4.7 – Examples of a persistence diagram and barcode for grayscale image of benign (first row) and malignant (second row) tumor.

In Garin and Tauzin (2019), the database under study has a low range of values. Thus they first binarize the images before re-constructing the grey-scale associated images to apply the TDA pipeline.

GEOMETRICAL FEATURES Through test and error, we consider a set of thresholds that we denote T of size 200 that corresponds to 200 equidistant points from the minimum and maximum value of the images and their associated excursion sets for which we compute the three scaled geometrical features available: the area $\check{\mathcal{A}}$, perimeter $\check{\mathcal{P}}$, and Euler characteristic $\check{\mathcal{E}}$, with $\text{L}\check{K}\text{C} = \frac{\text{LKC}}{m^2}$. The area is implemented by summing all the white pixels of an image, the perimeter computed using the algorithm that is presented in the Introduction, which is based on Biermé and Desolneux (2021)'s paper, and the Euler characteristic by implementing the method presented in Ebner et al. (2018). To each geometrical function and its respective derivative, we apply a series of methods from the **Numpy** and **Scipy Python** library to summarize it; Through a process of trial and error, we identify the methods that produce the best classification score, f designates one the LKC functionals.

- The L2 norm of $\check{f}$ and ∂f computed using the **numpy.linalg.norm(., ord = 2)** function.
- The integral $\check{f}$ and ∂f computed using the **numpy.trapz(., T)** function.
- The sum over all the values of $\check{f}$, $\sum_{t \leq 200} \check{f}(t)$.
- The entropy value of $|\check{f}|$ and $|\partial \check{f}|$ computed using the **scipy.stats.entropy** function.
- The number of non-zeros value in $\check{f}$ and ∂f unsing the function **numpy.linalg.norm(., ord =0)**.
- The sum of $\check{f}$ and ∂f.

Although the sum and the integral seem to give the same numerical information, we observed that using both improves the performance of the classification results by 0.2% and reduces the set of false negatives for this method.

We obtain a total of 120 features per image and feed that to the random forest classifier.

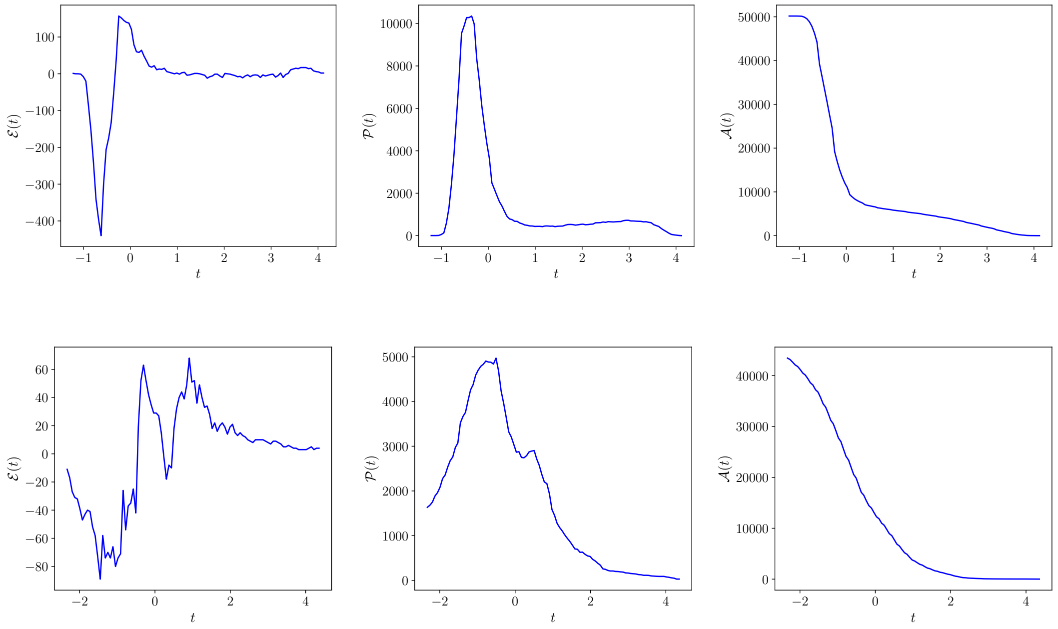

Figure 4.8 – Examples of the LKC functionals computed on 200 thresholds, from left to right Euler characteristic, perimeter and area, for grayscale image of benign (first row) and malignant (second row) tumor.

We observe in Figure 4.8 that the data is not centered and is positively shifted, thus it does not exhibit a Gaussian behavior.

We also include a method where we concatenate both the topological and geometrical vectors of features, in order to see if combining both methods could improve the classification, we will be referring to this third method as TDA+LKC.

4.3.2 Machine learning model and results

We opt for a simple random forest classifier to evaluate and compare the scores of the two methods; we bootstrap by dividing the dataset into 80% training data and 20% testing data, and train and test each model of the three models on the same training and testing dataset of patients. We perform bootstrap 500 times, thus collecting 500 scores computed using the function **score** method of the **RandomForestClassifier** class of **sklearn.ensemble**, we present in Table 4.1 the mean value of the scores and the standard deviation, Figure 4.9 is a histogram of the distribution of the scores for each method.

Model	mean value	std
TDA	0.84	0.01
LKC	0.84	0.01
TDA + LKC	0.86	0.01

Table 4.1 – Mean and std value of the bootstrap of the random forest's score.

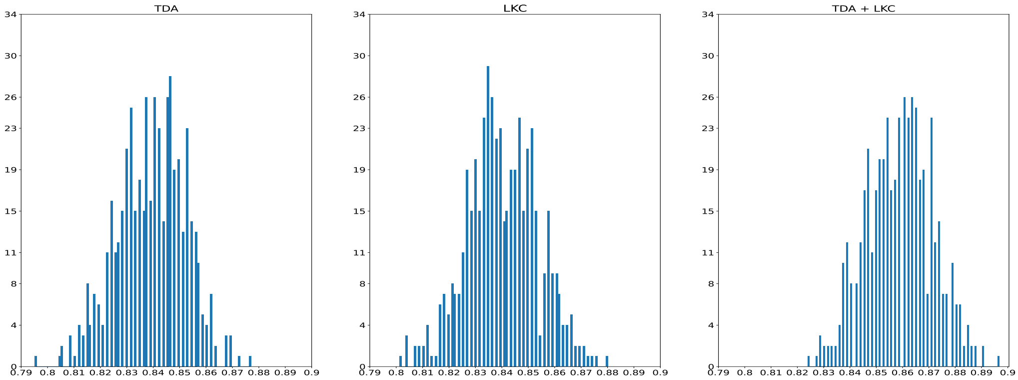

Figure 4.9 – Distribution of the score of the random forest bootstrapping for the three methods.

Table 4.1 shows that the TDA and LKC methods have similar classification performances, and combining the two increases the score by two percent on average. Figure 4.9, which represents the distribution of the scores, shows that the LKC method performs slightly better, presenting a higher minimal and maximal value. Though, combining the two is always best.

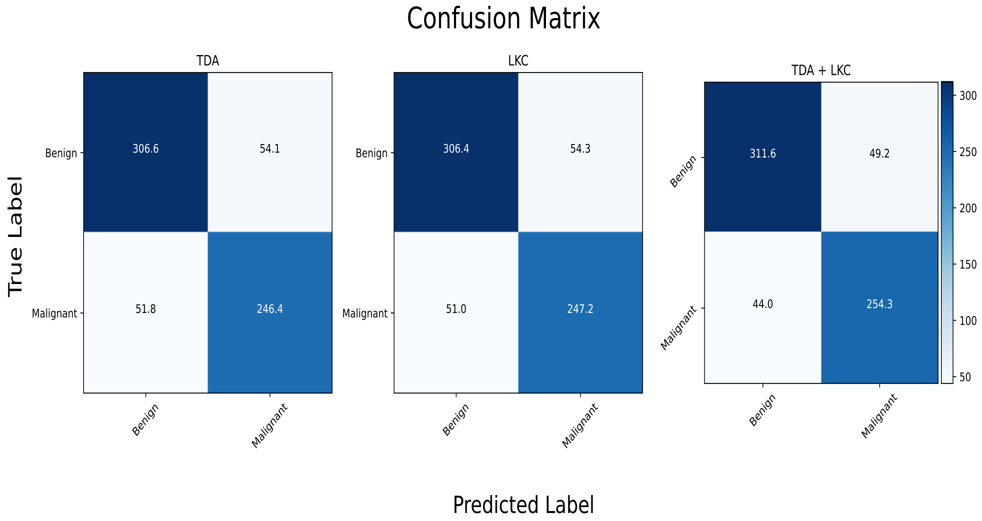

Figure 4.10 – Mean confusion matrix of the three methods.

Figure 4.10 is an in-depth comparison of the prediction results for the three methods. It represents the average confusion matrix obtained through bootstrapping. The LKC method exhibits a slightly lower rate of false negatives than the TDA method, while the latter slightly performs better regarding false positives, but the results are overall equivalent. However, the combined LKC+TDA approach improves the classification results for both false positives and negatives.

Within Table 4.2, we compute the mean value of the Adjusted Rank Index (ARI) for the 500 bootstraps for the three methods (TDA, LKC, and TDA+LKC). The ARI is a similarity measure between two sets of clustered data ranging from -1 to 1. An ARI equal to 1 indicates a perfect agreement between the two sets, 0 indicates random agreement, and -1 is a perfect disagreement. Therefore, the higher the ARI value is the closer the two sets of clusters are to each other. We compute the ARI using the **sklearn.metrics.adjusted_rand_score** function.

Model	(TDA, LKC)	(LKC, TDA+LKC)	(TDA, TDA+LKC)
Mean and std ARI	0.51 (0.04)	0.68 (0.04)	0.67 (0.04)

Table 4.2 – Mean value of the ARI between the predictions of the three methods.

At last, using functions from **sklearn.metrics** library, we compute the average f1-score and precision of the three methods, see Table 4.3.

Model	TDA	LKC	TDA+LKC
f1-score	0.82 (0.02)	0.82 (0.02)	0.85 (0.01)
precision	0.82 (0.02)	0.82 (0.02)	0.84 (0.02)

Table 4.3 – Mean of the f1-score and precision for the three methods.

Although TDA and LKC methods show similar results in this classification task, combining both always increases the performance of the classification.

EXAMPLES OF MISCLASSIFICATIONS FOR THE THREE METHODS. Below is a comparison of some of the results obtained from the three classification methods to present example of cases where one method misclassifies images while the others successfully classify them.

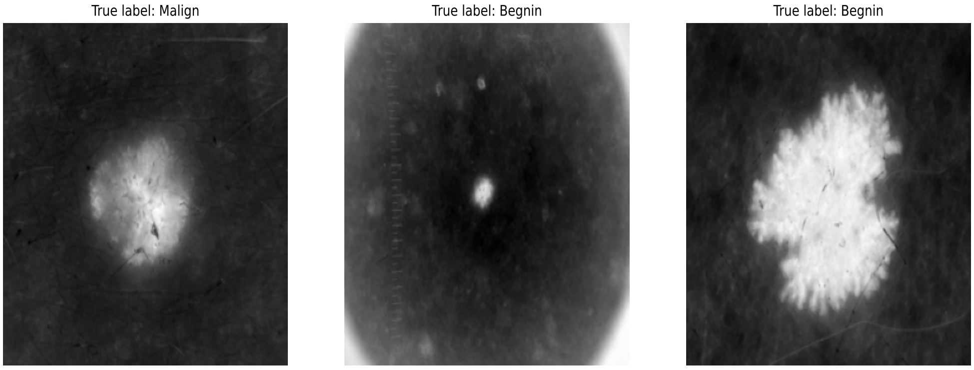

Figure 4.11 – Examples of images that are well labeled by TDA but wrongly classified by LKC.

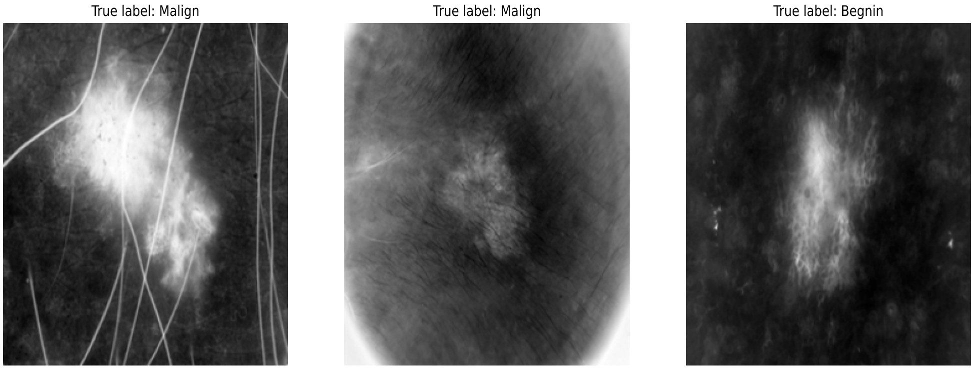

Figure 4.12 – Examples of images that are well labeled by LKC but wrongly classified by TDA.

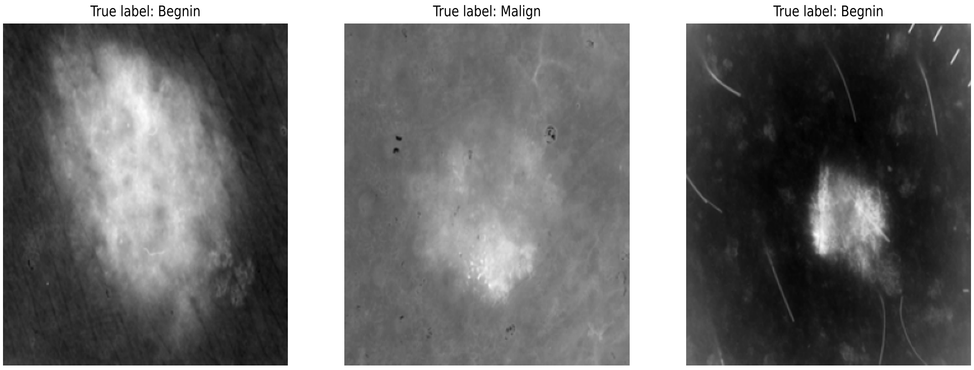

Figure 4.13 – Examples of images that are well labeled by LKC + TDA but wrongly classified by TDA and LKC.

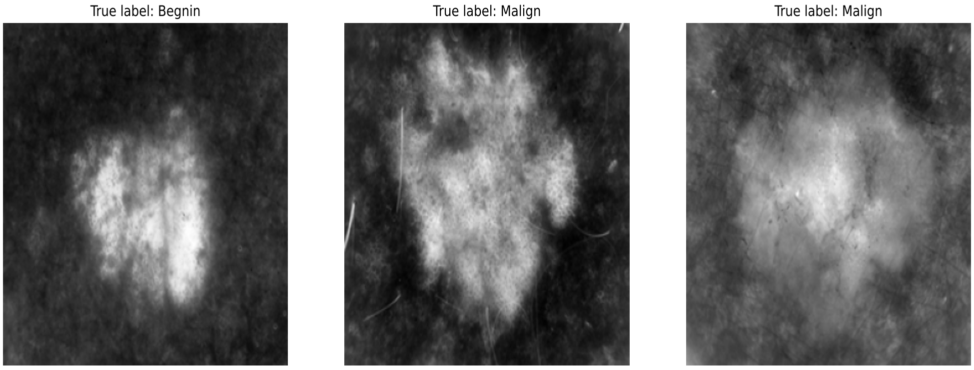

Figure 4.14 – Examples of images that are well labeled by LKC and TDA but wrongly classified by TDA + LKC.

Figure 4.15 – Examples of bad predictions for all three methods.

As we can see in the figures above, there is no discernable pattern for the naked eye that can explain why a method performs better than the other.

4.4 Exploring the potential of combining both topology and geometry

In our study investigating using the LKC for classification purposes, we leverage the complete geometrical information derived from the characteristics under study. To improve the analysis, we suggest exploiting the additive structure of the LKC and exploring them locally. For instance, the perimeter of the excursion set is equal to the sum of the perimeters of connected components within the excursion set, $\mathcal{P}(t) = \sum_{i \in C_i} \mathcal{P}_i(t)$, with $\mathcal{P}_i(t)$ being the perimeter of the ith connected component at threshold level t and adding that local information to the TDA means that we add geometrical information of the component to the information that is brought by it persistence. We can effectively combine geometric details with the relevant topological characteristics. In practice, we follow the existence of the component and its geometrical characteristics.

Toy example to illustrate

Let us consider an image (see left panel of Figure 4.16) of a multivariate Gaussian function of size 200×200. Within this image, we add a spot by intoducing a square of size 10×10 in the south east corner of the image, and attribute to all the pixels of the square an intensity equal to the maximum of the Gaussian. When we compute the persistence barcode of the upper-level filtration of the image, we observe that both the Gaussian and the added square result in two connected components of equal significance (right panel of Figure 4.16). Since they share the same intensity, they will both have the same birth value and approximately the same persistence. It is important to note that while a component may exhibit topological significance, it does not necessarily imply equal importance in terms of its structural and geometrical characteristics. It is worth to notice that the strength of TDA is that it fails to capture everything that is topologically invariant. Thus, solely relying on the persistence barcode or the persistence diagram, it becomes challenging to differentiate between the different structures that are present in the image.

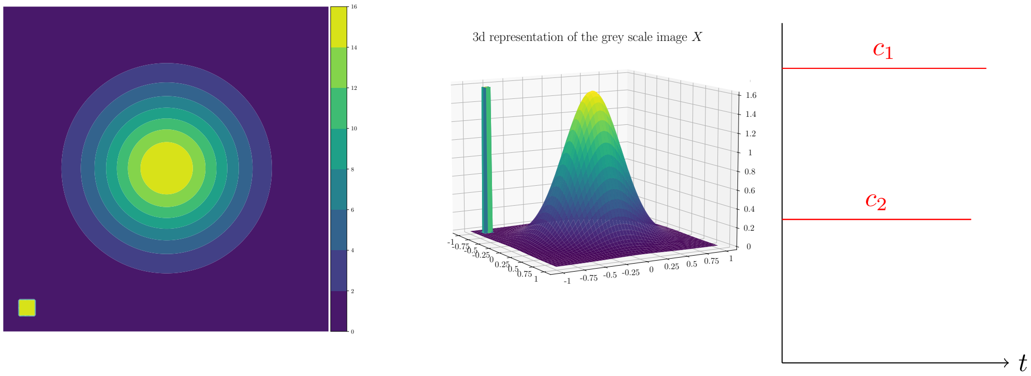

Figure 4.16 – Image of a multivariate Gaussian density and noise and its associated persistence diagram for the upper level filtration.

We can track the perimeter and area of each connected component of the excursion set as we keep track of its persistence. In doing so, it can prove useful and informative in assessing the significance of the underlying structures within the image and of their morphology.

The local analysis gives us a way to evaluate the significance of the underlying structures registered in the image, which enables us to differentiate between structural elements and noise.

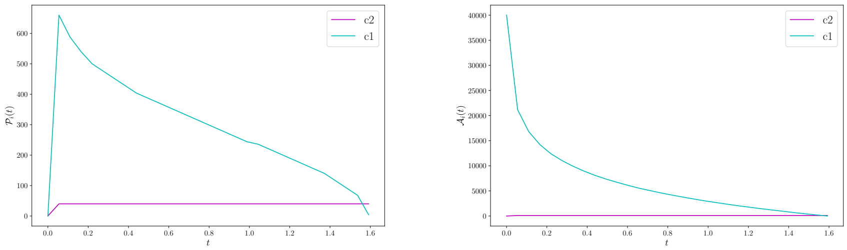

Figure 4.17 – Perimeter (left panel) and area (right panel) of the connected component in orange and blue, and the total perimeter and the area in red.

Figure 4.17 represents the two geometrical features of the two connected components, perimeter and area. As we can see, the square has little prominence compared to the Gaussian in the image, thus it is easily spotted as noise. Hence, tracking the LKC of the connected components allows for a detailed analysis of the structure of the image, which makes it a promising method to explore.

5 General Conclusion & Perspectives

Conclusion Using random fields to model images allowed us to access a consequent theoretical framework to analyze the structures of the image. In particular, we focused our study on elements from integral geometry, the LK curvatures. At first, we studied the statistical properties of the perimeter and how it is linked to the covariance structure of the field. We explored its behavior and the different features it inherits from the random field. After computing the relevant statistics and establishing the CLTs, we constructed statistical tests to uncover said features using only sparse information. In the context of a white noise framework, we demonstrated that the first moment of the perimeter copies the symmetry structure of the marginal distribution of the field, thus enabling us to construct a test that covers that property. Furthermore, in the Gaussian framework, the first moment of the perimeter is closely linked to the covariance over the two canonical directions, allowing it to reveal the property of local isotropy.

Our research is not confined to theoretical developments alone; we also conducted numerical studies to test the theoretical results. We have applied our findings to real-world data sets, such as bone X-rays, to test for the local isotropy property. The successful application of these statistical tests to analyze real-world data further solidifies the potential of this approach for extracting meaningful insights from complex and diverse image-based datasets.

In the final chapter of this thesis, we explored the synergies between geometrical methods and the emerging Topological Data Analysis (TDA) method. We used both methods to classify skin cancer data and compared their respective performances, and explored the potential benefit of combining both methods to analyze images.

Perspectives In the case of the Gaussian framework, there is still work to be done regarding the second moment of the perimeter and the analysis of its complex form; it would be intriguing to examine its behavior in the In-fill context (*e.g.* $m \to \infty$) and compare its asymptotic form to the one obtained in the continuous framework. It would also be interesting to explore the potential relationship between the first and second moment in an extreme regime context $m \to \infty, t \to \infty$. It would permit avoiding the use of the variance in the testing procedure and favoring the first moment instead.

It would also be interesting to conduct the same analysis on the statistics of the Euler characteristic and exhibit what kind of information it can reveal in the field, and also to establish a joint central limit theorems between the perimeter and the Euler characteristic.

Finally, drawing inspiration from the insights gained in the last chapter, a captivating direction of study would involve examining the local behavior of the perimeter. This exploration could lead to an insightful connection with the notion of topological persistence, thereby paving the way to explore the fusion of geometry and topology in the context of machine learning. Such a combination holds great promise for advancing our understanding of complex data and enhancing the capabilities of machine learning algorithms.

BIBLIOGRAPHY

M. Abaach, H. Biermé, and E. Di Bernardino. Testing marginal symmetry of digital noise images through the perimeter of excursion sets. *Electronic Journal of Statistics*, 15(2): 6429 – 6460, 2021.

M. Abaach, H. Biermé, E. D. Bernardino, and A. Estrade. Local isotropy test based on the oriented perimeter of digitalized images. working paper or preprint, Mar. 2023.

R. J. Adler. *The Geometry of Random Field.* John Wiley & Sons, 1981.

R. J. Adler and J. E. Taylor. *Random fields and geometry.* Springer Monographs in Mathematics. Springer, New York, 2007.

R. J. Adler, O. Bobrowski, M. S. Borman, E. Subag, and S. Weinberger. Persistent homology for random fields and complexes. In *Institute of Mathematical Statistics Collections*, pages 124–143. Institute of Mathematical Statistics, 2010.

M. A. Arcones. Limit theorems for nonlinear functionals of a stationary gaussian sequence of vectors. *The Annals of Probability*, 22(4):2242–2274, 1994.

J. M. Azaïs and M. Wschebor. *Level sets and extrema of random processes and fields.* John Wiley & Sons, 2009.

C. Berzin. Estimation of local anisotropy based on level sets. *Electronic Journal of Probability*, 26:1–72, 2021.

H. Biermé. Introduction to random fields and scale invariance. To appear in a volume of the CEMPI Lecture Notes in Mathematics subseries, Jan. 2017.

H. Biermé and A. Desolneux. On the perimeter of excursion sets of shot noise random fields. *Annals of Probability*, 44(1):521–543, 01 2016.

H. Biermé and A. Desolneux. The effect of discretization on the mean geometry of a 2D random field. *Annales Henri Lebesgue*, 4:1295–1345, 2021.

H. Biermé and A. Lerbet. Study of the perimeter of a shot noise random field by an elementary approach. working paper or preprint, Apr. 2022.

H. Biermé, F. Richard, and C. L. Benhamou. Parametric estimation for Gaussian operator scaling random fields and anisotropy analysis of bone radiograph textures. In K. Pohl, editor, *International Conference on Medical Image Computing and Computer Assisted Intervention MICCAI'09*, pages 13–24, London, France, 2009.

H. Biermé, E. Di Bernardino, C. Duval, and A. Estrade. Lipschitz-Killing curvatures of excursion sets for two-dimensional random fields. *Electronic Journal of Statistics*, 13(1), 2019.

P. Billingsley. *Probability and Measure (3 ed.).* John Wiley and Sons, 1995.

A. Blake, P. Kohli, and C. Rother. *Markov Random Fields for Vision and Image Processing.* The MIT Press, 2011. ISBN 0262015773.

A. Bulinski, E. Spodarev, and F. Timmermann. Central limit theorems for the excursion set volumes of weakly dependent random fields. *Bernoulli*, 18(1):100 − 118, 2012a.

A. Bulinski, E. Spodarev, and F. Timmermann. Central limit theorems for the excursion set volumes of weakly dependent random fields. *Bernoulli*, 18(1):100–118, 2012b. ISSN 1350-7265.

C. Butler. A test for symmetry using the sample distribution function. *The Annals of Mathematical Statistics*, 40(6):2209–2210, 1969.

E. M. Cabaña. Affine processes: a test of isotropy based on level sets. *SIAM Journal on Applied Mathematics*, 47(4):886–891, 1987.

B. Casaponsa, B. Crill, L. Colombo, L. Danese, J. Bock, A. Catalano, A. Bonaldi, S. Basak, L. Bonavera, A. Coulais, et al. Planck 2015 results: XVI. Isotropy and statistics of the CMB. 2016.

C. Chappard, B. Brunet-Imbault, G. Lemineur, B. Giraudeau, A. Basillais, R. Harba, and C. L. Benhamou. Anisotropy changes in post-menopausal osteoporosis: characterization by a new index applied to trabecular bone radiographic images. *Osteoporosis International*, 16:1193–202, 2005.

F. Chazal and B. Michel. An introduction to topological data analysis: fundamental and practical aspects for data scientists, 2021.

F. Chazal, L. J. Guibas, S. Y. Oudot, and P. Skraba. Persistence-based clustering in riemannian manifolds. *J. ACM*, 60(6), nov 2013. ISSN 0004-5411.

S. Chiu, D. Stoyan, W. Kendall, and J. Mecke. *Stochastic Geometry and Its Applications.* Wiley Series in Probability and Statistics. Wiley, 2013.

Y.-M. Chung, C.-S. Hu, A. Lawson, and C. Smyth. Topological approaches to skin disease image analysis. In *2018 IEEE International Conference on Big Data (Big Data)*, pages 100–105, 2018. doi: 10.1109/BigData.2018.8622175.

R. Cotsakis, E. D. Bernardino, and C. Duval. Surface area and volume of excursion sets observed on point cloud based polytopic tessellations. working paper or preprint, Sept. 2022a.

R. Cotsakis, E. Di Bernardino, and T. Opitz. On the perimeter estimation of pixelated excursion sets of 2D anisotropic random fields. working paper or preprint, Mar. 2022b.

S. Csörgő and C. R. Heathcote. Testing for Symmetry. *Biometrika*, 74(1):177–184, 1987. ISSN 00063444.

R. D'Agostino and E. S. Pearson. Tests for departure from normality. Empirical results for the distributions of b^2 and $\sqrt{b_1}$. *Biometrika*, 60(3):613–622, 12 1973. ISSN 0006-3444.

F. Dalmao, J. León, and E. Mordecki. Asymptotic normality of high level-large time crossings of a Gaussian process. *Stochastic Processes and their Applications*, 06 2017.

A. Desolneux. Stochastic methods for image analysis. In *Stochastic geometry*, volume 2237 of *Lecture Notes in Math.*, pages 87–127. Springer, Cham, 2019.

E. Di Bernardino and C. Duval. Statistics for Gaussian random fields with unknown location and scale using Lipschitz-Killing curvatures. *Scandinavian Journal of Statistics*, pages 1–42, 2020.

E. Di Bernardino, J. León, and T. Tchumatchenko. Cross-Correlations and Joint Gaussianity in Multivariate Level Crossing Models. *Journal of mathematical neuroscience*, 4:22, 04 2014. doi: 10.1186/2190-8567-4-22.

E. Di Bernardino, A. Estrade, and J. R. León. A test of Gaussianity based on the Euler Characteristic of excursion sets. *Electronic Journal of Statistics*, 11(1):843–890, 2017.

M. Dindin, Y. Umeda, and F. Chazal. Topological data analysis for arrhythmia detection through modular neural networks. In C. Goutte and X. Zhu, editors, *Advances in Artificial Intelligence*, pages 177–188, Cham, 2020. Springer International Publishing. ISBN 978-3-030-47358-7.

B. Ebner, N. Henze, M. A. Klatt, and K. Mecke. Goodness-of-fit tests for complete spatial randomness based on Minkowski functionals of binary images. *Electronic Journal of Statistics*, 12(2):2873–2904, 2018.

A. Estrade and J. R. León. A central limit theorem for the Euler characteristic of a Gaussian excursion set. *The Annals of Probability*, 44(6):3849–3878, 2016. ISSN 0091-1798.

G. Flandin and K. J. Friston. Topological inference. In A. W. Toga, editor, *Brain Mapping: an Encyclopedic Reference*, pages 495–500. Academic Press, 2015.

A. Garin and G. Tauzin. A topological "reading" lesson: Classification of mnist using tda. *2019 18th IEEE International Conference On Machine Learning And Applications (ICMLA)*, pages 1551–1556, 2019.

R. A. Gatenby, O. Grove, and R. J. Gillies. Quantitative imaging in cancer evolution and ecology. *Radiology*, 269(1):8–14, 2013. doi: 10.1148/radiol.13122697. PMID: 24062559.

J. R. Gott, D. C. Hambrick, M. S. Vogeley, J. Kim, C. Park, Y.-Y. Choi, R. Cen, J. P. Ostriker, and K. Nagamine. Genus Topology of Structure in the Sloan Digital Sky Survey: Model Testing. *The Astrophysical Journal*, 675(1):16, 2008.

Y. Guan, M. Sherman, and J. Calvin. A nonparametric test for spatial isotropy using subsampling. *Journal of the American Statistical Association*, 99(467):810–821, 2004.

M. K. Gupta. An asymptotically nonparametric test of symmetry. *Ann. Math. Statist.*, 38: 849–866, 1967. ISSN 0003-4851.

A. Hatcher. *Algebraic topology.* Cambridge Univ. Press, Cambridge, 2000.

L. Heinrich. Stable limit theorems for sums of multiply indexed m-dependent random variables. *Mathematische Nachrichten*, 127(1):193–210, 1986.

B. Ivanovic, B. Miloševic, and M. Obradovic. Comparison of symmetry tests against some skew-symmetric alternatives in i.i.d. and non-i.i.d. setting. *Computational Statistics & Data Analysis*, 151(C), 2020.

B. Jähne. *Digital Image Processing 6th Edition.* Springer, Berlin [u.a.], 2005. ISBN 3540240357 9783540240358.

M. Kratz and S. Vadlamani. Central limit theorem for Lipschitz–Killing curvatures of excursion sets of Gaussian random fields. *Journal of Theoretical Probability*, 2017.

R. Lachièze-Rey. Bicovariograms and Euler characteristic of random fields excursions. *Stochastic Processes and their Applications*, 129(11):4687–4703, 2019a. ISSN 0304-4149.

R. Lachièze-Rey. Normal convergence of nonlocalised geometric functionals and shot-noise excursions. *Ann. Appl. Probab.*, 29(5):2613–2653, 2019b. ISSN 1050-5164.

D. E. Lake and D. M. Keenan. *Identifying minefields in clutter via collinearity and regularity detection*, volume 2496. SPIE, 1995.

E. Lespessailles, C. Gadois, G. Lemineur, J. P. Do-Huu, and C. L. Benhamou. Bone texture analysis on direct digital radiographic images: precision study and relationship with bone mineral density at the os calcis. *Calcif. Tissue Int.*, 80:97–102, 2007.

E. Lespessailles, C. Gadois, I. Kousignian, J. P. Neveu, P. Fardellone, S. Kolta, C. Roux, J. P. Do-Huu, and C. L. Benhamou. Clinical interest of bone texture analysis in osteoporosis: a case control multicenter study. *Osteoporosis International*, 19:1019–28, 2008.

D. Letscher and J. Fritts. Image segmentation using topological persistence. In W. G. Kropatsch, M. Kampel, and A. Hanbury, editors, *Computer Analysis of Images and Patterns*, pages 587–595, Berlin, Heidelberg, 2007. Springer Berlin Heidelberg. ISBN 978-3-540-74272-2.

M. S. Longuet-Higgins. The statistical analysis of a random, moving surface. *Philos. Trans. Roy. Soc. London Ser. A*, 249:321—387, 1957.

H. Luo and J. Strait. Combining geometric and topological information for boundary estimation. In *2021 IEEE International Conference on Big Data (Big Data)*, pages 3841–3852, 2021.

D. Marinucci. Testing for non-Gaussianity on cosmic microwave background radiation: a review. *Statist. Sci.*, 19(2):294–307, 2004. ISSN 0883-4237.

MATLAB. *Update 4 (9.9.0.1570001) (R2020b).* The MathWorks Inc., Natick, Massachusetts, 2021.

A. Mira. Distribution-free test for symmetry based on Bonferroni's measure. *Journal of Applied Statistics*, 26, 03 1997.

A. Molina and F. R. Feito. A method for testing anisotropy and quantifying its direction in digital images. *Computers & Graphics*, 26(5):771–784, 2002.

S. Müller, L. Schüler, A. Zech, and F. Heße. `GSTools` v1.3: a toolbox for geostatistical modelling in python. *Geoscientific Model Development*, 15(7):3161–3182, 2022.

D. Müller. A central limit theorem for lipschitz-killing curvatures of gaussian excursions, 2017.

M. C. N.M. van Lieshout. 42713 Applications of Stochastic Geometry in Image Analysis. In *New Perspectives in Stochastic Geometry*. Oxford University Press, 11 2009. ISBN 9780199232574.

W. K. Pratt. *Digital Image Processing*. John Wiley & Sons, Inc., USA, 1978. ISBN 0471018880.

J. F. Quessy. On Consistent Nonparametric Statistical Tests of Symmetry Hypotheses. *Symmetry*, 8, 2016.

S. Ranjbar and J. Ross Mitchell. Chapter 8 - an introduction to radiomics: An evolving cornerstone of precision medicine. In A. Depeursinge, O. S. Al-Kadi, and J. Mitchell, editors, *Biomedical Texture Analysis*, The Elsevier and MICCAI Society Book Series, pages 223–245. Academic Press, 2017. ISBN 978-0-12-812133-7.

T. Reddy, S. Vadlamani, and D. Yogeshwaran. Central Limit Theorem for Exponentially Quasi-local Statistics of Spin Models on Cayley Graphs. *Journal of Statistiacal Physics*, 2018.

F. J. Richard. Some anisotropy indices for the characterization of Brownian textures and their application to breast images. *Spatial Statistics*, 18:147–162, 2016.

J. Schmalzing and K. M. Górski. Minkowski functionals used in the morphological analysis of cosmic microwave background anisotropy maps. *Monthly Notices of the Royal Astronomical Society*, 297(2):355–365, June 1998.

R. Schneider and W. Weil. *Stochastic and integral geometry*. Probability and its Applications. Springer-Verlag, Berlin, 2008. ISBN 978-3-540-78858-4.

Y. Singh, C. M. Farrelly, Q. A. Hathaway, T. Leiner, J. Jagtap, G. E. Carlsson, and B. J. Erickson. Topological data analysis in medical imaging: current state of the art. *Insights into Imaging*, 14(1):58, Apr 2023. ISSN 1869-4101.

E. Somasundaram, A. Litzler, R. Wadhwa, S. Owen, and J. Scott. Persistent homology of tumor CT scans is associated with survival in lung cancer. *Med. Phys.*, 48(11):7043–7051, Nov. 2021.

D. Strömbom. Persistent homology in the cubical setting : theory, implementations and applications, 2007. Validerat; 20101217 (root).

F. Telschow, A. Schwartzman, D. Cheng, and P. Pranav. Estimation of Expected Euler Characteristic Curves of Nonstationary Smooth Gaussian Fields. *The Annals of Statistics*, 51:2272–2297, 2020.

C. Thäle. 50 years sets with positive reach - a survey. *Surveys in Mathematics and its Applications*, 3:123–165, 2008. ISSN 1843-7265.

R. Vandaele, G. A. Nervo, and O. Gevaert. Topological image modification for object detection and topological image processing of skin lesions. *Scientific Reports*, 10(1):21061, Dec 2020. ISSN 2045-2322.

R. Vandaele, P. Mukherjee, M. S. Heather, R. Pravin Shah, and O. Gevaert. Topological data analysis of thoracic radiographic images shows improved radiomics-based lung tumor histology prediction. *medRxiv*, 2022.

I. Wani and S. Arora. Computer-aided diagnosis systems for osteoporosis detection: a comprehensive survey. *Medical and Biological Engineering and Computing*, 58:1873–1917, 2020.

Z. Weller and J. Hoeting. A Review of Nonparametric Hypothesis Tests of Isotropy Properties in Spatial Data. *Statistical Science*, 31(3):305 – 324, 2016.

Z. D. Weller. spTest: An R package implementing nonparametric tests of isotropy. *Journal of Statistical Software*, 83(4):1–24, 2018.

K. J. Worsley. Local maxima and the expected Euler characteristic of excursion sets of χ^2, F and t fields. *Advances in Applied Probability*, 26(1):13–42, 1994. ISSN 0001-8678.

K. J. Worsley. The geometry of random images. *Chance*, 9(1):27–40, 1996.

M. Wschebor. *Surfaces aléatoires: mesure géométrique des ensembles de niveau*, volume 1147. Springer, 2006.

Abstract

This thesis explores the possibility of using geometrical functionals to analyze and summarize the geometrical attributes of an image. Using discretized random fields to model the image, we study the statistical behavior of the perimeter of the excursion sets associated with the image. We proceed by varying the conditions on the covariance structure of the field and observing how it affects the statistics of the perimeter. The first natural framework that emerges is the white noise framework, and the second is the stationary Gaussian random fields. This approach allowed us to construct a statistical test for the symmetry of the marginal distribution of the field in the first case and for local isotropy in the latter. Numerical studies support all our findings and results. We also applied the local isotropy test for local isotropy in calcaneus X-rays. Finally, we conclude our dissertation by comparing the performances of geometrical functionals to topological features retrieved using methods from Topological Data Analysis in a classification task.

Keywords: Geometrical characteristics, Discretized Random Fields, Image analysis, symmetry tests, local isotropy test.

Résumé

Cette thèse explore la possibilité d’utiliser des fonctionnelles géométriques pour analyser et résumer les attributs géométriques d’une image. En utilisant des champs aléatoires discrétisés pour modéliser l’image, nous étudions le comportement statistique du périmètre des ensembles d’excursion associés à l’image. Nous procédons en faisant varier les conditions sur la structure de covariance du champ et en observant comment cela affecte les statistiques du périmètre. Le premier cadre naturel qui émerge est le cadre du bruit blanc, et le second est celui des champs aléatoires Gaussiens stationnaires. Cette démarche nous a permis de construire un test statistique pour évaluer la symétrie de la distribution marginale du champ dans le premier cas et l’isotropie locale dans le second. Les résultats théoriques sont illustrés et complétés par des simulations numériques. Nous avons également appliqué le test d’isotropie locale à des radiographies du calcanéus. Enfin, nous concluons notre thèse en comparant les performances des fonctionnelles géométriques aux caractéristiques topologiques obtenues à l’aide de méthodes d’analyse de données topologiques dans une tâche de classification.

Mots-Clefs : Caractéristiques géometrique, champs aléatoires discrets, test de symmétrie, test d’istropie locale.